Dipl.-Ing. Philipp Rosenauer BSc

Modelling of Polyimides for Innovative Process & Product Integration in the Semiconductor Industry

DOCTORAL THESIS

to achieve the university degree of
Doktor der technischen Wissenschaften

submitted to

Graz University of Technology

Supervisor

Assoc.Prof. Dr.techn. Stefan Radl

Institute of Process and Particle Engineering

Graz, Jänner 2025

Dipl.-Ing Philipp Rosenauer BSc

Modelling of Polyimides for Innovative Process & Product Integration in the Semiconductor Industry

Dissertation

Mentor

Dr. Silvia Larisegger

Research & Technology House

Graz University of Technology

First Reviewer

Assoc.Prof. Dipl.-Ing. Dr.techn. Michaela Flock

Institute of Inorganic Chemistry

Graz University of Technology

Second Reviewer

Ao.Univ.Prof. Dipl.-Ing. Dr.techn. Günter Fafilek

Institute of Chemical Technologies and Analytics

Vienna University of Technology

AFFIDAVIT

I declare that I have authored this thesis independently, that I have not used other than the declared sources/resources, and that I have explicitly indicated all material which has been quoted either literally or by content from the sources used. The text document uploaded to TUGRAZonline is identical to the present doctoral thesis.

Date, Signature

Acknowledgment

First and foremost, I want to thank my supervisor at Graz University of Technology Prof. Stefan Radl for his continuous support and the fruitful discussions to overcome obstacles on the way over the past years.

Many thanks to my supervisor from the industrial partner, Dr. Silvia Larisegger, who proposed this project and helped me to manage the connection between academia and industry. Furthermore, she is responsible for the funding of the project via the Austrian Research Promotion Agency (FFG). The funding received from FFG and the industrial partner is greatly appreciated.

I also want to thank my colleagues at the Institute of Process & Particle Engineering (IPPE), the colleagues from Vienna University of Technology and my fellow students I had the pleasure to meet during my academic education.

Lastly, I want to thank my family and friends for supporting me during all the ups and downs over the years.

My biggest thanks go to my wife Isabella, who always supported me, cheered me up in times where no easy answer to problems could be found, and helped me to stay on track during all those years.

Abstract

This thesis focuses on the feasibility of applying molecular dynamics (MD) simulations to investigate the transport behavior of different species in a polyimide, namely Kapton®. This polyimide is used as a protective layer of semiconductor devices against corrosive gases, corrosive ions and humidity. The simulations should provide an understanding of the underlying mechanisms that affect the protective properties of the polyimide. The main transport mechanism that is investigated is the diffusion within the polyimide.

Simulations can be conducted (i) with more flexibility in terms of diffusing species and (ii) faster in comparison to saturation experiments that can take hundreds of hours (from personal communication with Stefan Wagner). Also, simulations provide rapid insight into the behavior in harsh and humid environments that are difficult to realize in experiments. Therefore, the applicability of the OPLS-AA force field, that allows simulations with liquid phases, was verified in a first step. Physical properties such as the density, the glass-transition temperature, the Young's modulus and the Poisson's ratio were determined from simulations and compared to experimental data from literature.

All-atom MD simulations of ions in the polyimide matrix were conducted with the OPLS-AA force field. Trends like the temperature dependency and the effect of ionization, meaning comparing cupric and cuprous ions, on the diffusion coefficient, were replicated with the all-atom simulations. However, for quantitatively determining the diffusion coefficient in the polyimide the simulation times were too short.

Therefore, coarse-grained force field parameters for systems involving Kapton® were obtained. This enabled longer coarse-grained simulations to quantitatively determine the diffusion coefficient of organic solvents in the polyimide. Organic solvents were chosen since (i) they impact the durability of the polymer film, and (ii) experimental data was available that allowed a verification of the results. Although MD simulations up to 500 ns were conducted, the required simulation time (i.e., approximately 2.4 ms) was out of reach by a factor of 5000. However, a blueprint of how to (i) obtain coarse-grained force field parameters, as well as (ii) conduct coarse-grained simulations, is presented. These blueprints allow researchers to conduct meaningful simulations once the computational power is accessible to reach sufficiently long simulations times.

Contents

Table of Contents

Table of Figures

Table of Tables

1 Introduction

1.1 Motivation

A large number of applications involving polymers is related to selectively transport ions and molecules [1]. Especially in corrosion processes it is important to understand limiting and accelerating factors that influence this transport of, e.g., corrosive gases, in order to protect industrial devices [2]. The high thermal stability of the polyimides, as well as their mechanical toughness and dielectric strength make them an important material in the electronic industry [3]. For this work the anticorrosive behavior of polyimide films in form of coatings [4] is of special interest to the industrial partner. The focus in the present thesis was on the polyimide PMDA-ODA, better-known under its brand name Kapton®.

There is no direct way of measuring the diffusion coefficient from ions that migrate through a membrane or a film. In experiments, the permeability is the parameter that can be measured: Varain et al. [5] showed, in a parallel work to the present work, a way to determine the diffusion coefficient with permeability measurements based on a set of numerically solved ordinary differential equations and estimated partitioning coefficients. However, determining the diffusion coefficient *in silico*, e.g., with the aid of molecular dynamics (MD) simulations would allow for more flexibility in material investigation.

A very detailed atomistic understanding of these transport processes can be achieved through such molecular dynamics simulations: for example, effects such as the swelling behavior of polymers due to moisture absorption can be predicted without lengthy experiments [6]. With the results from MD simulations - first and foremost the diffusion coefficient of an ion or molecule - polymers can be rationally developed, and designed to provide better corrosion protection. Additionally, the determination of physical properties from MD simulations will allow an estimation of possible applications that require higher mechanical strengths.

Research has shown that results of MD simulations can describe mechanical properties of polyimides [7], [8], [9], [10]. However, the combination of the software tools used, the force fields to describe the polyimide system, and the methods to determine physical properties has not been used for research so far. In our opinion the presented MD-based framework allows for the highest degree of flexibility.

1.2 State-of-the-art in molecular dynamics simulations

Neyertz et al. [6], [11], [12], [13], [14], [15] investigated the transport of various gases and water through polyimide membranes with MD simulations. They also described the simulation procedure to prepare free-standing membranes based on the real-world synthesis process. This preparation procedure was followed in this work as well, as these free-standing membranes allow the simulation of the experiments that were conducted by Lars Varain [16]. However, Neyertz et al. investigated mainly gases, which have faster diffusion coefficients than ions and organic solvents that were the species of interest in the present study. Therefore, it was possible for them to determine the diffusion coefficient with AA simulations.

Especially in the field of batteries the investigation of the diffusion of ions through polymers [17] with MD simulations is a topic of huge interest [18], [19]. In the field of battery simulations, the species of interest is Lithium. As the elements that were investigated in the experiments of Varain, i.e., sodium (Na) and potassium (K), are alkali metals like lithium, it was promising to investigate these with MD simulations as well.

Diddens et al. [19] investigated different possible effects on the ion mobility of the polymers with MD simulations. This topic is also of interest for the present work, as understanding the underlying mechanisms of the transport behavior would allow the design of materials towards improved properties.

In terms of mechanical properties different groups investigated polyimides with MD simulations. Lei et al. [7] investigated the thermo-mechanical properties of PMDA-ODA (i.e., Poly[4,4'-oxydiphenylenepyromellitimide]), which is the scientific name for Kapton®. In their work, they used the COMPASS force field and the so-called "stress–Strain" scripting approach in the 'Material Studio' simulation package.

Odegard et al. [10] predicted the mechanical properties of polymers with different force fields, including the OPLS-AA force field. However, Kapton® was not investigated in their research.

Riccardi et al. [8], [9] described a method to determine a locally resolved Young's modulus and Poisson's ratio. In their work, they investigated an atactic polystyrene (PS) thin film and a polystyrene nanocomposite, described by the OPLS-AA force field. However, PS has a comparably simple structure to simulate in comparison to the structure of Kapton®.

1.3 Goals and content

The goal of this thesis is to simulate the transport processes of different species, e.g. ions, corroding gases and organic solvents, in a polyimide protective film. Furthermore, the investigation of the mechanical properties of the polyimide films was a topic of interest.

It was important to the industrial partner to investigate the feasibility of determining transport processes in polyimides, based on molecular dynamics simulations. The polyimide Kapton® was chosen, as it is a widely used and well described material in literature. Having literature data for a material, that can be used to verify the results from simulations, is vital before transferring the findings from discovered methods to novel materials.

A blueprint to conduct both AA and coarse-grained (CG) simulations with already available software tools, i.e., LAMMPS [20] and VOTCA [21], as well as some in-house code for the post-processing is provided. This blueprint allows to (i) create a CG representation of an AA system, (ii) conduct the CG MD simulations, (iii) determine the self-diffusion coefficient and (iv) verify if the Einstein equation is applicable to the system.

The main part of this work contains the two publications "*Extraction of Mechanical Parameters via Molecular Dynamics Simulation: Application to Polyimides"* and *"Towards coarse-grained MD of polyimides: combining PC-SAFT theory, experiments and MD simulations"*. Both publications have a separate methods section, where all steps that were necessary to obtain the presented results are described. The conclusion and outlook into the future conclude the main part of the thesis. Further results, for example the investigation of ion transport properties, can be found in the appendix.

1.4 Contributions to publications

Chapter 2 is based on a scientific publication and chapter 3 will be submitted in the near future. In this section the author's contributions are summarized.

1.4.1 Publication on mechanical properties of polyimides

P. Rosenauer, C. Kratzer, S. Larisegger, and S. Radl, "Extraction of Mechanical Parameters via Molecular Dynamics Simulation: Application to Polyimides," *Polymers (Basel)*, vol. 16, no. 6, p. 813, Mar. 2024, doi: 10.3390/polym16060813.

P. Rosenauer: Conceptualization, Methodology, Simulations, Postprocessing Code, Visualization, Writing

1.4.2 Publication on coarse-grained simulations of polyimides and organic solvents

P. Rosenauer, S. Larisegger, and S. Radl, "Towards coarse-grained molecular dynamics simulations of polyimides: combining PC-SAFT theory, experiments and MD simulations".

P. Rosenauer: Conceptualization, Methodology, Simulations, Postprocessing Code, Visualization, Writing

2 Extraction of Mechanical Parameters via Molecular Dynamics Simulation: Application to Polyimides

2.1 Introduction

Polyimides have a vast number of applications in the field of semiconductor protection. They are used as a passivation stress buffer to protect the semiconductor chip surfaces from thermal and mechanical stresses in packaging processes. Furthermore, they are used as a protective layer from α-rays released by inorganic fillers in epoxy-molding compounds (EMC) and as a final insulation layer before interconnect bumping operations. Adapting and improving their behavior in regard to mechanical and thermal protection behavior is an important topic in materials science. Combining both the molecular dynamics simulations with experimental characterizations is often beneficial (or even necessary) to obtain a deeper understanding of influencing factors [1], [22], [23].

The first step in an attempt to improve the properties of a polymer with simulation is to verify the accurate representation of the reality with the used simulation parameters. Therefore, physical properties are predicted by means of computer simulations that can easily be compared to experimental or literature data. Our group has already investigated the density and glass-transition temperature properties.

Lei et al. [7] investigated the thermo–mechanical properties of six different polyimide films, including PMDA-ODA (Poly [4,4'-oxydiphenylenepyromellitimide]). Kapton® is the brand name of PMDA-ODA. In their work, they used the COMPASS force field and the so-called "Stress–Strain" scripting in the Material Studio simulation package. The Material Sstudio simulation package is a commercially available software tool that brings along licensing costs. Lei et al. also investigated the polymer PMDA-BIA, which was investigated as a second polyimide in our current work, as the literature data for it is extremely sparse.

Odegard et al. [10] predicted the mechanical properties of polymers with different force fields. In their study, they investigated a single polyimide (i.e., BPDA-APB) with the force fields AMBER, OPLS-AA, and MM3. The prediction of the mechanical properties, namely the Young's modulus and the shear modulus, was most accurate in comparison to experimental values with the OPLS-AA force field. However, Kapton® was not investigated by them, and we placed the focus of this work on determining the quality of predicted mechanical properties of Kapton® with the OPLS-AA force field.

Riccardi et al. [8], [9] described a method to determine a locally resolved Young's modulus and Poisson's ratio. In their work, they investigated an atactic polystyrene (PS) thin film and a polystyrene nanocomposite. For describing the atactic polystyrene, the OPLS-AA ("optimized potentials for liquid simulations all-atom") [24] force field was used. PS has a comparably simple structure to simulate in comparison to the objective polymers of the present study, i.e., polyimides.

The objective of our present study is to determine the applicability of the OPLS-AA force field to the polyimides (i) Kapton® (or PMDA-ODA) and (ii) pyromellitic dianhydride/2-(4-aminophenyl)-1H-benzimidazole-5-amine(PMDA-BIA). In order to determine if the mentioned force field can be applied to PMDA-ODA and PMDA-BIA, (i) a thorough investigation of how to determine the Young's modulus and the Poisson's ratio was conducted, and (ii) the computed results were compared to the literature data. Kapton® was used as it is a commercially available standard polymer. PMDA-BIA was used as it is a similar polymer with different properties. In future research, we plan to use Kapton® in combination with an aqueous liquid phase. Therefore, the OPLS-AA force field was used.

The Young's modulus and Poisson's ratio were determined via molecular dynamics with either (i) a simulation of the well-established tensile test [25], [26], [27], [28] or (ii) the methodology proposed by Riccardi et al. [8], [9]. To allow for more flexibility, contrary to previous works ([7]), in this work, the large-scale atomic/molecular massively parallel simulator (LAMMPS) [29] was used with the OPLS-AA force field.

The first section of this work describes the simulation and modeling details to allow the interested reader to replicate our results. Specifically, the preparation procedure for the virtual polymer molecules and the numerical parameters used by the software are described. Additionally, the different procedures used to calculate Young's modulus will be described.

The results section is organized in a way that the effect of each influencing parameter, like the system size, temperature, and pressure, are described individually for each deformation mode. This allows the reader to understand the different application fields of the deformation modes and what parameters to look for. The last part of the result section compares the behavior of the material in the simulations with literature and experimental data.

2.2 Materials and Methods

2.2.1 Molecular Dynamics Simulation Method

The molecular dynamics simulations in the present study were conducted with LAMMPS [29] (LAMMPS branch: stable; commit: 584943fc928351bc29f41a132aee3586e0a2286a (28 October 2020)). To allow for the greatest flexibility in polymers that are investigated, the base geometry of a monomer is determined by vector coordinates in an xyz-file. The atomic structure of the monomers that were investigated in our present work were extracted in the form of bond lengths and angles from Ramos et al. [30]. With the atomistic bond lengths and angles, it was possible to calculate the coordinates of each atom of the monomer to prepare the xyz-file. Moltemplate [31] (git branch: master; commit: 9f1512e6b25f8325b5c6c1a4f2fecdc94eda40f1 (21 March 2021)) was used to transform this xyz-file into the required LAMMPS input file collection. Moltemplate allows the user to determine the size of the simulation box, the chain length, and the number of chains, which is beneficial for the investigation of polymeric materials.

As the initial state for a molecular dynamics simulation is created artificially, the system needs to be equilibrated before the actual simulation runs. The equilibration removes structural artifacts that occurred during the initialization of the system [32] and imposes the correct pressure and temperature on the system for the simulation. There are various ways and definitions to ensure that an equilibrated state has been reached [32]. In this study, the system was equilibrated based on the 21-step equilibration that uses a certain procedure of NVT (constant temperature, constant volume) and NPT (constant temperature, constant pressure) ensembles to reach that equilibrated state [33]. In the present study, the maximum pressure was set to be 50,000 (atm), and the final pressure and final temperature represent ambient conditions at 1 (atm) and 300 (K).

2.2.2 Simulation Parameters

Here, we describe the simulation parameters used in the present study to allow the reader the replication of the simulations. The parameters described were used for all systems of both investigated polymers.

Both for the relaxation mode and the continuous deformation mode, periodic boundaries were imposed. Atom style "full" was chosen with real units. Bond, angle, and improper style were harmonic, and the OPLS style was used for dihedrals. The styles determine how the bonded forces between all atoms of the polymer of interest are calculated. The formulas for these potentials can be found in the LAMMPS manual [29]. For non-bonded interactions, the pair

style lj/cut/coul/long was used, which computes a standard 12/6 Lennard–Jones potential with an additional coulombic pairwise interaction. In LAMMPS, a long-range solver is used to compute long-range coulombic interactions. Most of these long-range solvers perform their computation in K-space, which we also prefer by using the "kspace style" command. As k-space style "pppm" with an accuracy of 0.0001 is used, and "kspace modified gewald" with a rinv value of 0.0002 [$Å^{-1}$] is used to ensure that every simulation is conducted with the same solver conditions. Here, rinv represents the G-ewald parameter for Coulombics and is given in reciprocal distance units.

2.2.3 Force Field and Numerical Parameters

The "optimized potentials for liquid simulations" (OPLS) force field was used in its all-atom form to describe the interatomic interactions. This force field was developed by Jorgensen et al. [34], [35] and is widely used in molecular dynamics simulations [36]. Additionally, moltemplate has the OPLS force field already included, which allows for a less time-intensive preparation of the polymer system.

2.2.4 Chain Length Selection

The chain length selection impacts the behavior and results of the molecular dynamics simulation [37], [38]. The system behaves stiffer if the chain length is longer, i.e., the systems tend to have a stiffer elastic regime and higher yield stresses [38]. In particular, the entanglement is influenced by the chain length and is shown in the yield peak. Shorter chains can more easily align with the direction of loading and show a less pronounced yield peak. However, computational power is the limiting factor in molecular dynamics simulation; therefore, a chain length of 20 monomers was chosen as a compromise. This was motivated by the fact that model chains with 10–20 repeating units were previously found to be sufficient for reasonable results [39], [40], [41], [42] without inducing size effects.

For reasons of comparability, the chain length that was chosen for Kapton© was also used for the simulations involving the PMDA-BIA polyimide.

2.2.5 System Size

The system size in molecular dynamics simulations is an important metric both for the results of the simulation and the required computational power. An important task is to find the sweet spot between those criteria and get the most representative results with the least possible computational power. Before the final system sizes were defined, some preliminary simulations were conducted to compare three system sizes. Table 1 shows the size of the different systems, the number of chains in each system, and the chain length. The preliminary results showed that

system A was not behaving isotropically already in our preliminary analysis. Furthermore, although Ries et al. [43] showed that the system size has no impact on their results, their systems were all larger than 104 atoms. Due to these reasons, we decided to remove system A from the investigation but kept the naming, as displayed in Table 1.

Investigations of system size were skipped from the beginning for the additionally investigated polymer PMDA-BIA, as it was assumed that the smallest system would not produce usable results. As the number of atoms per monomer group is different for the two systems, Table 2 shows the respective number of atoms for each system.

Table 1: Different system sizes and chain lengths for PMDA-ODA (Kapton®).

System	Chains	Monomers per Chain	Atoms
A	27	5	5265
B	16	20	12,480
C	80	20	62,400

Table 2: Different system sizes and chain lengths for PMDA-BIA.

System	Chains	Monomers per Chain	Atoms
B	16	20	14,496
C	80	20	72,480

2.2.6 Relaxation Mode

This method was first introduced by D. N. Theodorou and U. W. Suter [25] to predict the elastic constant of a glassy polymer. Further development of the procedure was conducted by Riccardi et al. [8], [9] to locally resolve Poisson's ratio and Young's modulus of composite materials. The main idea behind this method is to apply a small deformation at time t0 and let the system relax afterwards. The relation of stress, strain, and elastic stiffness coefficient matrix are related according to Equation (2-1). Under the assumption of an isotropic material, this relation can be reduced to Equation (2-2):

$$\bar{\sigma} = \bar{\bar{C}} \cdot \bar{\varepsilon} \tag{2-1}$$

$$\begin{bmatrix} \varepsilon_{xx} \\ \varepsilon_{yy} \\ \varepsilon_{zz} \end{bmatrix} = \frac{1}{E} \begin{bmatrix} 1 & -\nu & -\nu \\ -\nu & 1 & -\nu \\ -\nu & -\nu & 1 \end{bmatrix} \cdot \begin{bmatrix} \sigma_{xx} \\ \sigma_{yy} \\ \sigma_{zz} \end{bmatrix}. \tag{2-2}$$

The main benefit of the method is the ability to locally resolve Poisson's ratio in a compound material. Therefore, the strain is imposed in two directions uniformly; otherwise, the local displacements would be a function of the overall material properties if periodic boundary conditions were used [8]. During the deformation, the length of the edges in the third axis is held constant. After inducing the strain, an equilibration phase follows, whereby the length in the deformed directions is held constant in contrast to the unperturbed axis, which can change

its length to balance the emerging stress. Figure 1 shows the basic principle of this "relaxation mode"-type of simulation.

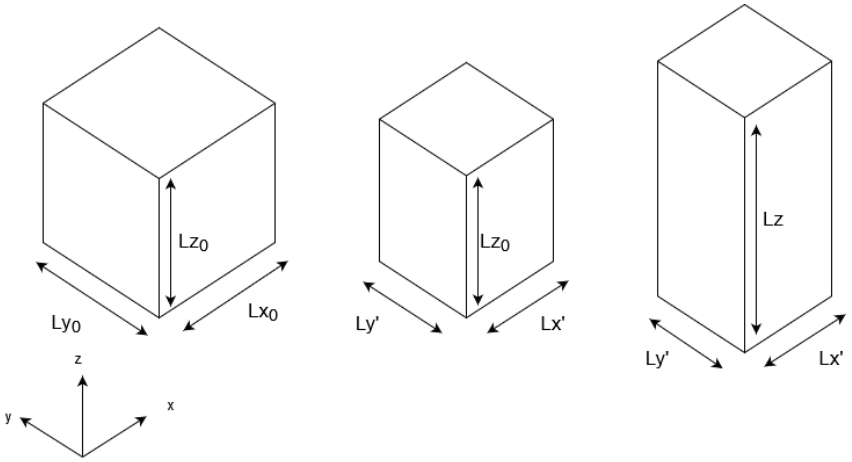

Figure 1: Depiction of the method to determine Young's modulus and Poisson's ratio via "relaxation mode" simulations.

Due to the biaxial strain scheme imposed on the system in the x and y direction, $\sigma xx = \sigma yy = \sigma\parallel$, and $\varepsilon xx = \varepsilon yy = \varepsilon\parallel$. With the further assumption of mechanical equilibrium, the stress $\sigma zz = 0$; thus, Equation (2-2) results in two linear equations, i.e., Equations (2-3) and (2-4). By rearranging these equations, a direct measurement of Young's modulus (Equation (2-5)) and Poisson's ratio (Equation (2-6)) is possible. The same rearrangements could be made by inducing the strain as a combination of the other directions:

$$\sigma_{\parallel} - \nu\sigma_{\parallel} = E\varepsilon_{\parallel} \tag{2-3}$$

$$-2\nu\sigma_{\parallel} = E\varepsilon_{zz} \tag{2-4}$$

$$E = \frac{2\sigma_{\parallel}}{2\varepsilon_{\parallel} - \varepsilon_{zz}} \tag{2-5}$$

$$\nu = -\frac{\varepsilon_{zz}}{2\varepsilon_{\parallel} - \varepsilon_{zz}} \tag{2-6}$$

Due to fluctuations in the MD simulations, 100 computed values were combined to one averaged value to smoothen the results. Furthermore, the final value of Young's modulus was determined by averaging the results of the last 50% of the simulation time. The simulation time in the relaxation mode experiments was 5 ns.

2.2.7 Continuous Deformation Mode

The continuous deformation mode represents the tension test that is well-known and widely used to determine Young's modulus and Poisson's ratio of elastic materials. In the conventional tension test, Young's modulus is determined from the stress–strain curve with Equation (2-7), as shown in Figure 2. Here, ε is the deformation in percent of the initial length as shown in

Equation (2-8), and σ is the stress in the normal stress in the material. Another important factor that is affecting the result of the simulation is the deformation rate $\dot{\varepsilon}$, defined in Equation (2-9) [44]:

$$E_i = \frac{\sigma_i}{\varepsilon_i} \tag{2-7}$$

$$\varepsilon = \frac{L - L_0}{L_0} \tag{2-8}$$

$$\dot{\varepsilon} = \frac{\Delta\varepsilon}{\Delta t} \tag{2-9}$$

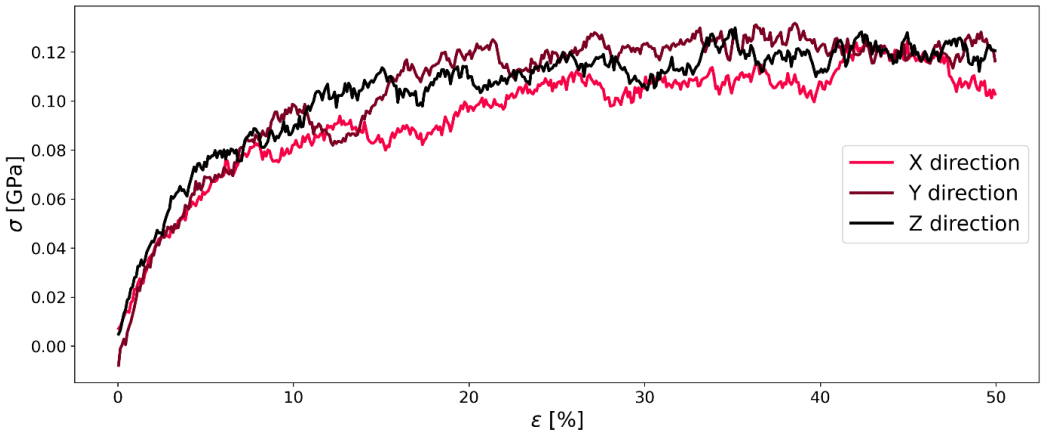

Figure 2: Stress–strain diagram of stretching system C of Kapton® as shown in Table 1with a strain rate of $1x10^{-7}\ fs^{-1}$.

As mentioned previously, to ensure that each simulation starts at the same initial state, the system is equilibrated before the actual simulation run. In the next step, the system is deformed in one direction with a certain deformation rate up to a maximum deformation, depending on the simulation time. It is important to mention that the deformation rate is extremely high in comparison to the real tension experiments where the deformation rate is between 10^{-4} [s^{-1}] and 10^{5}[s^{-1}]. In all our continuous deformation mode simulations of the present work, the rate is between 10^{-8}[fs^{-1}] and 10^{-5}[fs^{-1}], thus, 10^{2} to 10^{5} higher than the highest deformation rate of the real experiments.

The Young's modulus can then be calculated as the slope of a straight line fit between the origin (at ambient pressure) and the respective stress, for which the Young's modulus is calculated. There is not one Young's modulus, but each strain has a different Young's modulus as the slope of the straight-line fit varies with different strains. The anisotropy Γ and the linearity in the form of R^2 were introduced to allow for an objective determination of Young's modulus.

2.2.8 Anisotropy Γ

It is important that a small system (as modeled in an MD simulation) can represent the bulk of the polymer of interest as adequately as possible. One important property that needs to be represented is the isotropy. Therefore, every system was deformed in the three spatial directions x, y, and z. In the next step, normalized perpendicular stress was determined for each direction following Equations (2-10) and (2-11).

$$\bar{\sigma} = \frac{\sigma_x + \sigma_y + \sigma_z}{3} \tag{2-10}$$

$$\sigma_i^*{}_{,n} = \frac{\sigma_i}{\bar{\sigma}} \tag{2-11}$$

$$\Gamma_{(\varepsilon)} = \frac{1}{N} \sum_{N=\varepsilon-0.01}^{N=\varepsilon} \sigma_{\sigma_i^*{}_{,n(\varepsilon)}} \tag{2-12}$$

The anisotropy is calculated by averaging the standard deviation of the normalized perpendicular stress $\sigma_{\sigma_i^*{}_{,n(\varepsilon)}}$ of the last percent of strain before the strain (corresponding to the value of Γ) is calculated (Equation (2-12)).

2.2.9 Linearity

The second determining factor is the R^2 value of a straight line that is fitted to the simulation results to obtain Young's modulus. Determining Young's modulus in this way is only valid when the system follows Hooke's law up to the first plastic deformation. Hooke's law is valid when there is a linear relationship between the deformation and the stress at this deformation [45]. In order to verify the linearity quantitatively and, therefore, to probe the validity of Hooke's law, the R^2 value of the fit was logged. A high R^2 represents a good representation of the results by the straight line fit.

2.2.10 Software

The software used for the simulation runs (i.e., LAMMPS), the pre-processing steps, and the exact version (i.e., commits) of the software was already mentioned at the beginning of the Methods Section (see "Molecular Dynamics Simulation Method"). The post-processing tools that were used for visualization were (i) Microsoft® Excel® for Microsoft 365 MSO (Version 2401 Build 16.0.17231.20236) 64-bit, and (ii) self-written python scripts (Python 3.10.9 64-bit.) developed in the Spyder IDE (version 5.4.1).

2.3 Results and Discussion

2.3.1 Effect of System Size and Isotropy

The first thing that was investigated was the effect of the system size on the isotropy of the polymer system. As mentioned in the section about the relaxation mode, it is necessary for the system to be isotropic, i.e., to be able to use Equations (2-5) and (2-6) to calculate Young's modulus and Poisson's ratio. Both systems B and C were investigated regarding their isotropy. The isotropy was investigated based on the already described anisotropy Γ. Figure 3 shows the anisotropy in the first 10% of strain of system B and system C. From about 1.7% on, the black line that represents the anisotropy of system C is below the red line of system B. In this case, a lower anisotropy represents a more isotropic system.

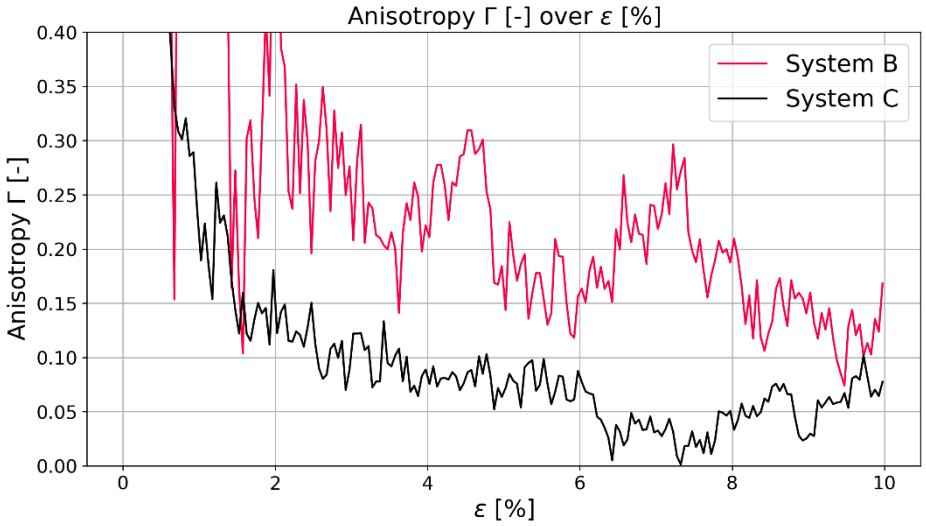

Figure 3: Comparison of anisotropy Γ of system B (red) and system C (black) for Kapton©.

From this investigation, it can be seen that additional to the chain length mentioned by [37], [38], the system size is also relevant for MD predictions of the polymeric system. Both systems have the same chain length, but system C has five times more chains in comparison to system B. Further differences that surfaced due to the size difference was the behavior during stretching and compressing: regarding the calculated Young's moduli of system B and system C, the general trend was that the difference between the moduli in system B is about 20% between compression and stretching while the difference in system C was about 10%. Although simulations were conducted for both system sizes, the results presented in the next sections were taken from the simulations of system C, as there was a clear indication that the larger system leads to more representative results. Figure 4 shows the same behavior for the second investigated polymer PMDA-BIA. With the confirmation of this system size-dependent

behavior, it can be said that bigger systems are beneficial for simulations that require a certain isotropy for representative results.

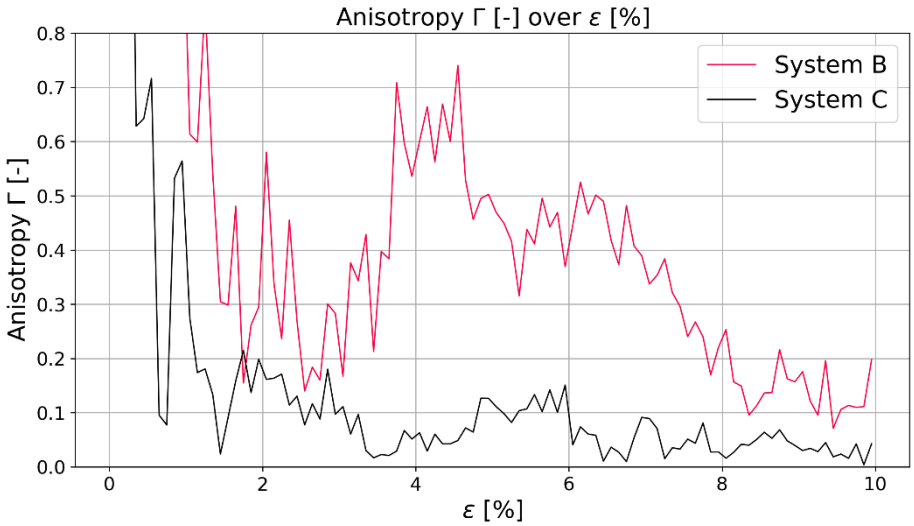

Figure 4: Comparison of anisotropy Γ of system B (red) and system C (black) for PMDA-BIA.

2.3.2 Effect of the Temperature

2.3.2.1 Relaxation Mode

The results from the relaxation mode simulations represent the assumed behavior from the literature: Lyulin et al. [27] showed a linear decrease of the Young's modulus with increasing temperatures up to the glass-transition temperature. Here, we also demonstrate that above the glass-transition temperature, Young's modulus leveled off and stayed constant, although temperatures were increasing for both polymers. With rising temperatures, the Young's modulus and the Poisson's ratio were decreased. The investigation of Young's modulus for Kapton® over the temperature showed a change in slope between 600 (K) and 700 (K), which coincides with the glass-transition temperature described in the literature[7], [46]. Contrary, for PMDA-BIA, there was a steep decline in Young's modulus between 500 K and 600 K. This coincided with the found glass-transition temperature of density monitoring from our simulations but did not coincide with the glass-transition temperature reported by Lei et al. [7].

2.3.2.2 Continuous Deformation Mode

In the continuous deformation mode, the Young's modulus also leveled off with rising temperature, but it was also seen that the behavior of the system changed with rising temperatures. For the equilibration process at 300 (K) the system started to expand when the simulation was conducted at higher temperatures. This led to a negative stress, although the system was stretched in one direction, and the stress should have been positive. Additionally, it was found that there was no linear behavior between higher deformation and stress, but the stress response stayed the same upon a continued deformation of the material. This leads to our

speculation that around the glass-transition temperature, where this behavior change was the highest, the system lost parts of its tensile strength.

This behavior in the continuous deformation mode indicates that the equilibration method should be adapted before the measuring simulation. We assume that this can be done either (i) if the last NPT step of the 21-step equilibration is already conducted at elevated temperatures or (ii) an additional equilibration step is included before the measuring run to give the system the chance to equilibrate at the temperature of the simulation before measuring the stress–strain behavior. However, this would be a task for further investigation.

2.3.3 Effect of the Pressure

As the stress in molecular dynamics simulations is determined with the compute pressure command, it was assumed that the pressure will have a certain effect on the simulation results. In the MD simulations, the pressure was logged for each simulation run (i.e., stress and pressure were computed using LAMMPS' "compute pressure" command). This was done in order to systematically investigate the effect of pressure on the system properties. Simulations regarding the Poisson's ratio, Young's modulus, and density were conducted in relaxation mode and normalized with the respective literature data. The results of these simulations are summarized in Figure 5. As can be seen in Figure 6 and Figure 7, the results of the continuous deformation mode also show a dependence on the pressure, but this effect is smaller than what is observed in the relaxation mode simulations.

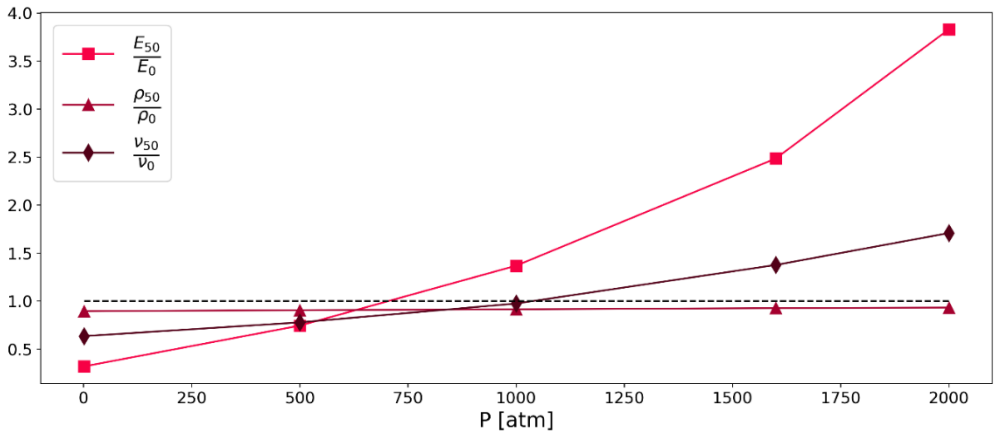

Figure 5: Pressure dependence of Young's modulus, Poisson's ratio, and density from relaxation mode simulations (system C) of Kapton®. The black dotted line represents the target value at 1 as this graph visualizes simulation values normalized to literature values.

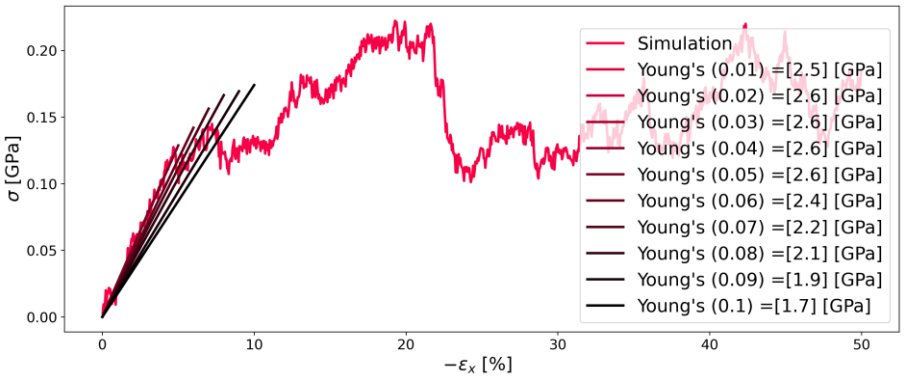

Figure 6: Stress–strain diagram of system C of Kapton® during compression in the x-direction at 1 (atm). The simulation results are depicted as the red line. Straight lines with changing colors represent the linear fit for each corresponding strain (indicated in parenthesis in the legend).

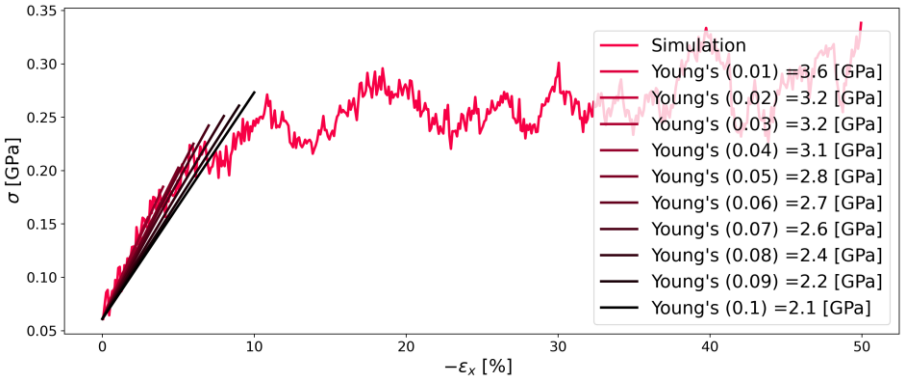

Figure 7: Stress–strain diagram of system C of Kapton® during compression in the x-direction at 750 [atm]. For interpretation of the legend, see the description in Figure 6.

2.3.3.1 Relaxation Mode

For the determination of the best representation of the real behavior by the simulation, a normalized Young's modulus, a normalized density, and a normalized Poisson's ratio were used. The values were normalized with data from the literature [46]; therefore, the best result for each of the investigated values is 1. For the simulation results the latter half of the 5 ns simulation run was averaged for each pressure and normalized as mentioned above. The best fit was determined to be at 750 (atm). Based on these findings, it was decided that simulations of the continuous deformation mode should be conducted at 750 atm as well. Simulations at this pressure resulted in the best agreement with literature, in respect to Young's modulus, density, and Poisson's ratio, as shown in Figure 5.

2.3.3.2 Continuous Deformation Mode

Figure 6 and Figure 7 show that also the continuous deformation mode simulations are affected by different pressures, but to a smaller extent, as a result of the relaxation mode simulations. In order to determine the Young's modulus for each percent of deformation, a linear fit was applied to the simulation data. Specifically, as a least squares method was used, the linear fit had different ordinate distances that represented the stress at zero strain. For ambient pressure, this

needs to be zero in an equilibrated system. Therefore, the linear fit was forced to pass through the origin. On the contrary, at a pressure of 750 (atm), the stress at zero strain was higher as the elevated pressure also induced a certain stress on the system, although there was no strain applied at the beginning of the simulation. For this case, the linear fit was forced to pass through the stress determined at zero strain for each percentage of deformation. Both simulations at 1 (atm) and 750 (atm) showed reasonable agreement for Young's modulus when compared to the literature value of 2.5 (GPa) [46].

Based on the findings from the investigation of Kapton®, the second polymer PMDA-BIA was investigated at the same pressures and temperatures for reasons of comparability. Figure 8 and Figure 9 show that the behavior of both polymers is similar. Contrary to Kapton®, it is interesting that there was less influence of the pressure on the Young's modulus for PMDA-BIA. Furthermore, there is very little literature data that allows a comparison of the Young's modulus of PMDA-BIA: in contrast to the agreeing results of Kapton®, the simulated results of this study were far off the results by Lei H. et al. [7], which is the only literature data that we found on this polymer. As the data were in good agreement with the experimental data, and the same procedure as for Kapton® was used, the reliability of the literature data was questioned. In [7], a Young's modulus higher than 8.5 GPa was reported for PMDA-BIA, while the results of our study were in the order of 2 GPa.

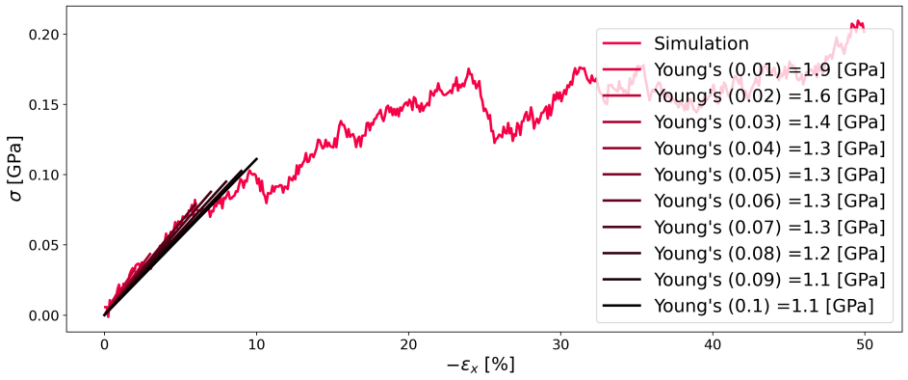

Figure 8: Stress–strain diagram of system C of PMDA-BIA during compression in the x-direction at 1 (atm). The simulation results are depicted as the red line. Straight lines with changing colors represent the linear fit for each corresponding strain (indicated i in parenthesis in the legend).

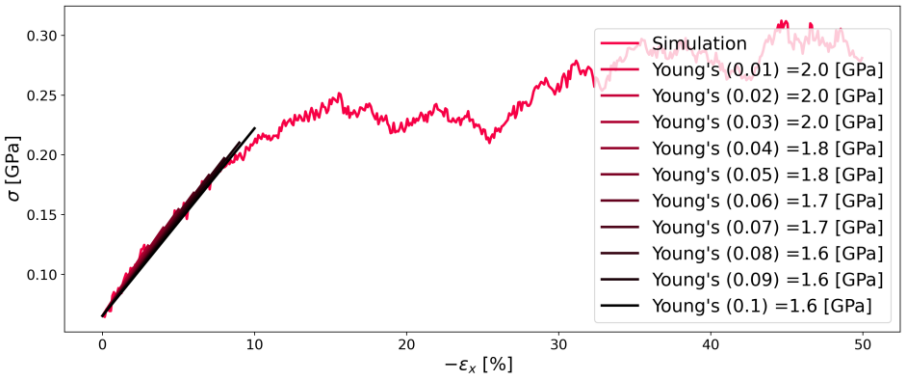

Figure 9: Stress–strain diagram of system C of PMDA-BIA during compression in the x-direction at 750 (atm). For interpretation of the legend, see description in Figure 8.

2.3.4 Youngs Modulus and Poisson Ratio

The stress–strain curve during the continuous deformation mode for both compression and expansion is shown in Figure 10. Our results showed the same known behavior of higher stresses at higher strain rates as observed for other polymers in MD simulations [27], [38], [47]. There was no detectable strain softening after the yield point in compression and a plateauing of the stress in stretching. There was no strain softening regime after the yield point, which also represents the typical behavior of a polyimide.

The general behavior for all stress–strain curves during the continuous deformation mode stayed the same: First, there is a linear increase of the stress, followed by a region in which the slope decreases. Finally, the stress is almost constant (only for the slowest deformation rate 10^{-8} (fs^{-1}); there is a significant temporal fluctuation of the stress) till the end of the simulation. Also, there is a clear difference in the performance of the compression and stretching of the system: By stretching the system, the maximum stress was below the results of the compression simulations, especially at high strain rates. We speculate the following: The entangled chains need some time to relax after deformation is initiated. During stretching, entangled chains become loose-packed, which leads to lower intermolecular forces and hence, stresses. In contrast, during our compressive deformation simulations, the chains increasingly entangle with ongoing deformation, building up extremely high stress (approximately twice as high as during stretching). As we will show later, this also leads to extremely high values of the Poisson's ratio.

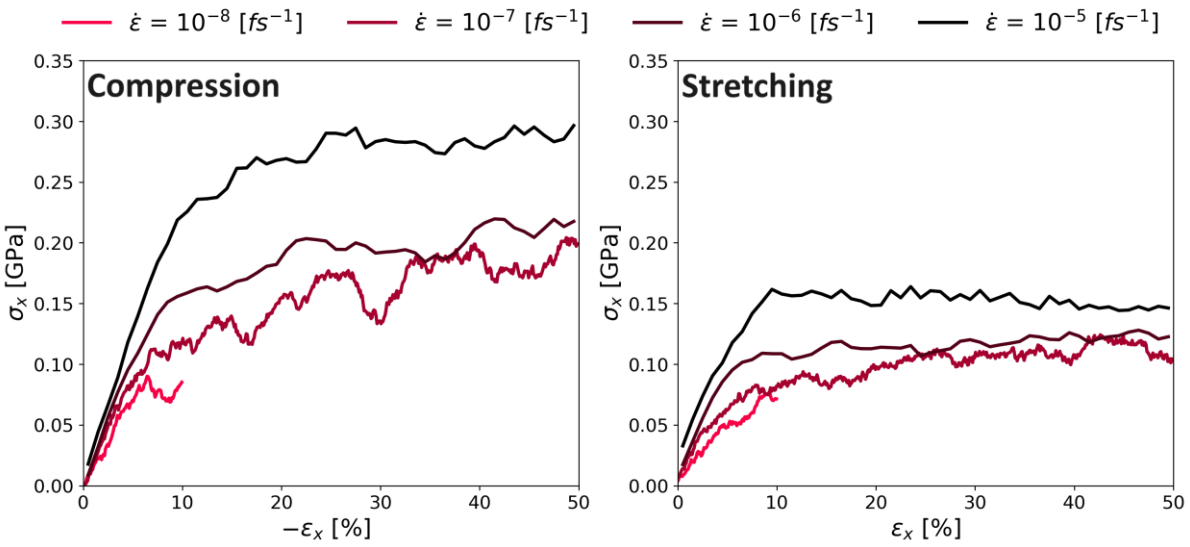

*Figure 10: Stress–strain relation for different strain rates on system C of Kapton®. **Left** panel with induced compression; **right** panel with induced stretch.*

Figure 11 shows a similar behavior for PMDA-BIA. The stresses during compression (shown in the left panel) were higher than during stretching, as in the case of Kapton®. While the behavior during stretching was very similar to the stretching of Kapton®, the compression of PMDA-BIA at the lowest deformation rate kept a linear upward trend after the initial steep linear behavior.

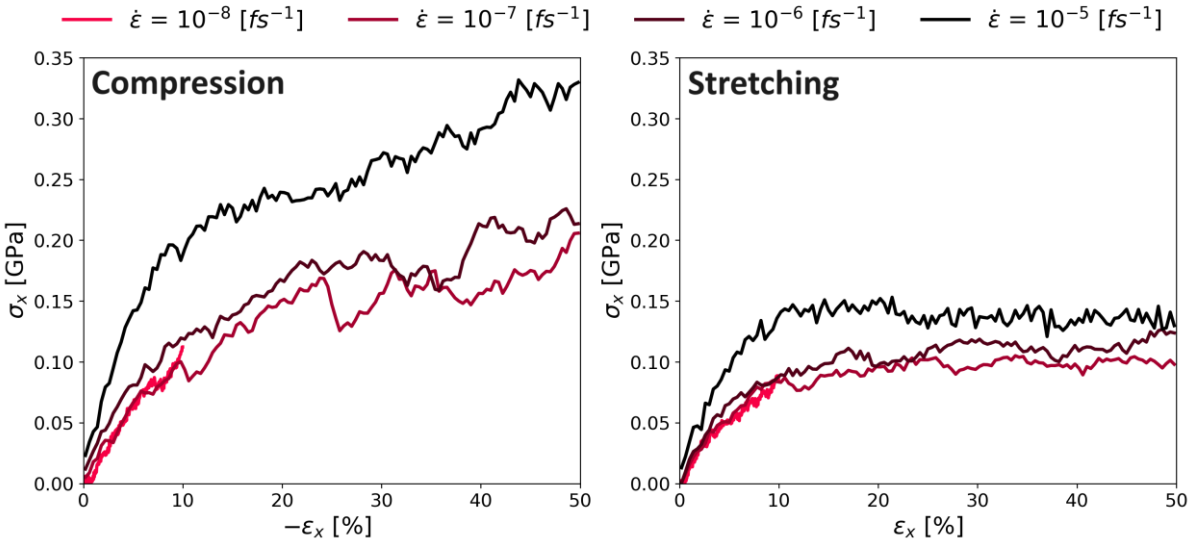

*Figure 11: Stress–strain relation for different strain rates on system C of PMDA-BIA. **Left** panel with induced compression; **right** panel with induced stretch.*

A noticeable semi-logarithmic relationship between the Young's modulus and the strain rate was observed in the literature [48], [49]. Specifically, this behavior was observed in laboratory experiments that indicated that a faster deformation leads to a higher Young's modulus. Exactly

such a trend was also observed in our compression and stretching simulation data, as shown in Figure 12.

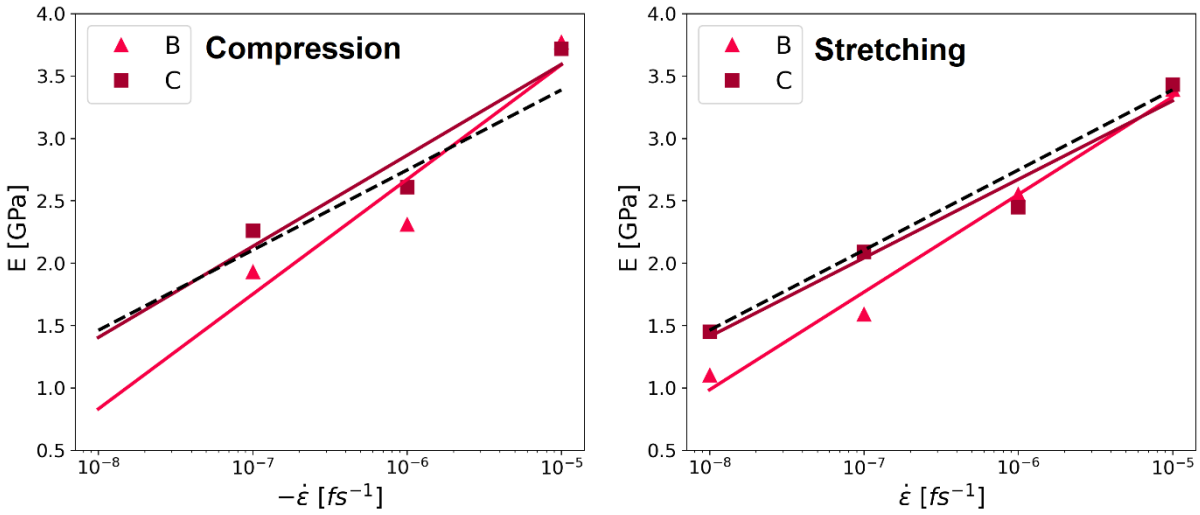

*Figure 12: Young's modulus of Kapton® analyzed at 2% strain, versus strain rate, simulated values as squares for system C, and triangles for system B. The plotted lines are fits using the least square method. The colors of the lines replicate the colors of the symbols for the respective system sizes described in the legend. **Left** panel: compression. **Right** panel: stretching. Results are in good agreement with values found in experiments using Kapton® HPP ST [49], indicated as a black dashed line.*

Analyzing the slope of regression lines from Young's modulus versus strain rates results in a slope of 0.27 for the Kapton® (system C). This result was similar to the results observed during experiments using HPP ST polyimide films with a slope of 0.28 [49]. Also, the other simulated values agree well with values between 0.34 and 0.23. However, the laboratory trials were performed at significantly slower strain rates between 10^{-4} and 10^{-1} $[s^{-1}]$. The coefficient of determination R^2 in the compression simulations is 0.91 for system C and 0.90 for system B. In the case of the stretching deformation mode, the coefficients of determination are even higher (i.e., 0.97 for system C and 0.98 for system B).

Besides the similar slope to the existing literature, the increased Young's modulus caused by longer chains matches the expected behavior, as well as results for different polymers during MD simulations (Refs. [27], [38], [47]; all these simulations used the continuous deformation mode).

Although there were no values from experiments regarding the impact of the deformation rate on the Young's modulus for PMDA-BIA, the same simulations as for Kapton® were conducted to see if the same semi-logarithmic behavior could be found. Similarly to Kapton®, the Young's modulus of system C of PMDA-BIA showed a semi-logarithmic behavior, as can be seen in Figure 13. In contrast, the behavior of system B could not be described by the semi-logarithmic fit for PMDA-BIA. The coefficient of determination for compression for system C was 0.91,

and for system B it was 0.44. In the stretching simulations, the coefficient of determination for system C was 0.98 and for system B was 0.75. This is another indication that the system size is relevant, and that a larger system is beneficial for the simulation results of molecular dynamics simulations conducted in this study.

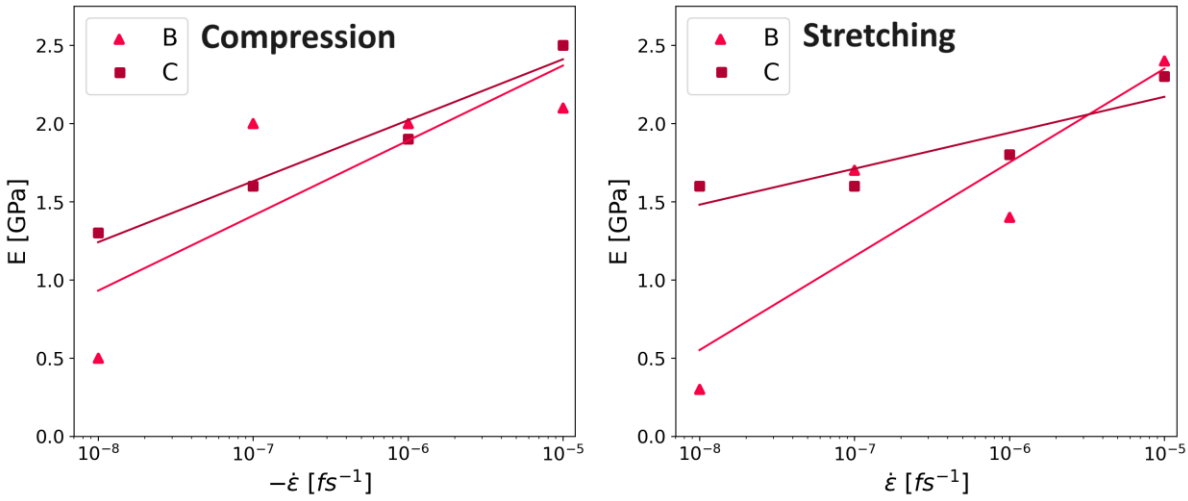

*Figure 13: Young's modulus of PMDA-BIA analyzed at 2% strain, versus strain rate, simulated values as squares for system C, and triangles for system B. The plotted lines are fits using the least square method. The colors of the lines replicate the colors of the symbols for the respective system sizes described in the legend. **Left** panel: compression. **Right** panel: stretching.*

During the stretching of the simulation box, the Poisson's ratio decreased from values around 0.4 down to $\nu = 0.3$ (see right panel Figure 14). Other researchers found the same influence, namely a decrease of the Poisson's ratio for polystyrene for increasing strain ([47], [50]; these observations were made below the glass-transition temperature, the same as in our study). Finally, there was no clear trend on how the Poisson's ratio changed when changing the strain rate.

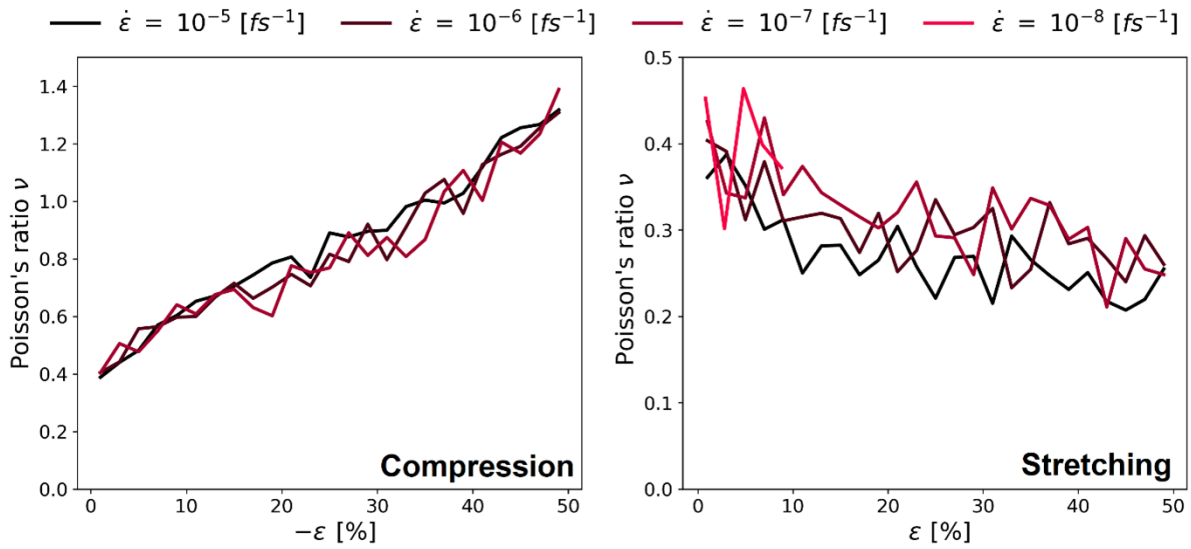

*Figure 14: Continuous deformation mode, Poisson's ratio vs. strain for different $\dot{\varepsilon}$, system C of Kapton®. **Left** panel with stretching the system; **right** panel with compression.*

The left panel of Figure 14 shows the results during compression simulations. The behavior of increasing Poisson's ratio did not match the expectations, and values over 0.5 [-] were physically not plausible (i.e., volume expansion upon compression). However, in the elastic regime (i.e., small deformation), the values around $\nu = 0.4$ were in good agreement with the results with a positive strain.

Figure 15 shows the Poisson's ratio of PMDA-BIA. As the behavior is very similar to the case of Kapton® shown in Figure 14, we assume the same reasons for that behavior as before. Contrary to the investigation of Kapton® the slowest deformation rate ($10^{-8}\ fs^{-1}$) leads to extremely high Poisson's ratios and large fluctuations.

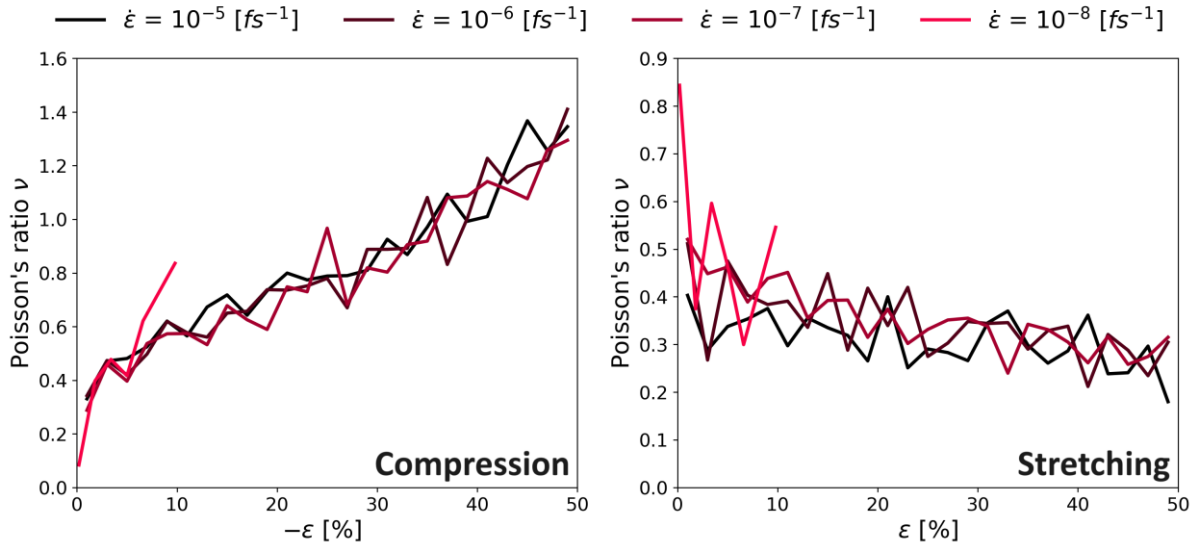

*Figure 15: Continuous deformation mode, Poisson's ratio vs. strain for different $\dot{\varepsilon}$, system C of PMDA-BIA. **Left** panel with stretching the system; **right** panel with compression.*

Figure 16 shows the result tables for the continuous deformation mode simulations of system C with different deformation rates. The results for R^2 and the anisotropy Γ were color-coded to indicate the following: green means a high level of matching the criteria, red means a low level of matching the criteria. These criteria were defined as follows: Quality of a linear fit $R^2 > 0.88$ in each direction and isotropy parameter $\Gamma < 0.11$, rows matching both criteria were highlighted in grey. Finally, we note in passing that our prediction for the spatially averaged Young's modulus at 4% deformation in the results table (Figure 16A) replicates the value from the literature (2.5 (GPa)) almost perfectly [46].

(A)

ε	X	Y	Z	anisotropy	X	Y	Z	
	R^2			Γ	E [Gpa]			average
1%	0.795	0.110	0.852	0.200	2.15	4.14	2.25	2.85
2%	0.913	0.848	0.966	0.193	2.16	3.4	2.28	2.61
3%	0.939	0.928	0.979	0.160	2.23	3.11	2.37	2.57
4%	**0.964**	**0.935**	**0.983**	**0.086**	**2.22**	**2.89**	**2.27**	**2.46**
5%	0.976	0.946	0.979	0.127	2.17	2.75	2.18	2.37
6%	**0.974**	**0.952**	**0.984**	**0.071**	**2.09**	**2.64**	**2.14**	**2.29**
7%	**0.975**	**0.939**	**0.975**	**0.071**	**2.03**	**2.51**	**2.06**	**2.20**
8%	**0.975**	**0.914**	**0.959**	**0.069**	**1.98**	**2.38**	**1.97**	**2.11**
9%	**0.969**	**0.886**	**0.938**	**0.053**	**1.92**	**2.25**	**1.88**	**2.02**
10%	0.952	0.830	0.886	0.086	1.84	2.12	1.76	1.91

(B)

ε	X	Y	Z	anisotropy	X	Y	Z	
	R^2			Γ	E [Gpa]			average
1%	0.812	0.565	0.908	0.235	1.46	3.41	1.93	2.27
2%	0.953	0.885	0.974	0.181	1.82	2.81	2.16	2.26
3%	**0.980**	**0.921**	**0.974**	**0.089**	**1.89**	**2.54**	**2.05**	**2.16**
4%	**0.986**	**0.906**	**0.945**	**0.089**	**1.88**	**2.3**	**1.85**	**2.01**
5%	**0.986**	**0.907**	**0.946**	**0.064**	**1.83**	**2.14**	**1.74**	**1.90**
6%	**0.977**	**0.908**	**0.947**	**0.087**	**1.75**	**2.02**	**1.66**	**1.81**
7%	0.971	0.854	0.950	0.031	1.68	1.87	1.6	1.72
8%	0.953	0.822	0.958	0.051	1.61	1.75	1.56	1.64
9%	0.911	0.810	0.957	0.025	1.51	1.66	1.51	1.56
10%	0.881	0.804	0.909	0.078	1.43	1.58	1.43	1.48

(C)

ε	X	Y	Z	anisotropy	X	Y	Z	
	R^2			Γ	E [Gpa]			average
1%	0.795	0.142	0.844	0.196	1.43	2.58	1.58	1.86
2%	0.936	0.568	0.946	0.124	1.49	1.80	1.42	1.57
3%	0.970	0.832	0.910	0.113	1.54	1.62	1.23	1.46
4%	**0.985**	**0.926**	**0.954**	**0.020**	**1.53**	**1.56**	**1.31**	**1.47**
5%	**0.988**	**0.951**	**0.969**	**0.033**	**1.50**	**1.53**	**1.35**	**1.46**
6%	**0.988**	**0.945**	**0.979**	**0.046**	**1.46**	**1.45**	**1.34**	**1.42**
7%	**0.977**	**0.953**	**0.965**	**0.055**	**1.41**	**1.40**	**1.28**	**1.36**
8%	**0.911**	**0.923**	**0.970**	**0.071**	**1.30**	**1.33**	**1.25**	**1.29**
9%	0.833	0.893	0.961	0.096	1.20	1.25	1.21	1.22
10%	0.760	0.843	0.946	0.060	1.12	1.18	1.16	1.15

Figure 16: Results tables of Young's modulus for system C of Kapton in the continuous deformation mode for different strain rates at ambient pressure. The results for R2 and the anisotropy Γ were color-coded to indicate the following: green means a high level of matching the criteria, red means a low level of matching the criteria. Rows matching both criteria were highlighted in grey and their values are displayed bold. (A) Strain rate of 1 × 10−6 (fs−1). (B) Strain rate of 1 × 10−7 (fs−1). (C) Strain rate of 1 × 10−8 (fs−1).

Figure 17 shows the results table for system C of PMDA-BIA under the same criteria as for Kapton®. The rows that match both criteria were highlighted in grey as before. Except for the case of a deformation rate of $1 \times 10^{-6}\, fs^{-1}$ the values that fulfill the criteria are found at higher strains compared to Kapton®.

(A)

	X	Y	Z	anisotropy	X	Y	Z	
ε		R^2		Γ		E [Gpa]		average
1%	0.029	0.760	0.677	0.333	2.93	2.84	1.38	2.38
2%	0.836	0.899	0.910	0.081	2.49	2.33	1.99	2.27
3%	0.814	0.950	0.956	0.072	2.09	2.16	2.03	2.09
4%	**0.891**	**0.947**	**0.976**	**0.034**	**1.96**	**2**	**2.06**	**2.01**
5%	**0.915**	**0.966**	**0.985**	**0.064**	**1.85**	**1.96**	**2.03**	**1.95**
6%	0.877	0.959	0.975	0.042	1.71	1.87	1.95	1.84
7%	0.860	0.965	0.929	0.107	1.61	1.82	1.81	1.75
8%	0.827	0.965	0.863	0.093	1.51	1.77	1.66	1.65
9%	0.849	0.948	0.816	0.070	1.46	1.7	1.55	1.57
10%	0.842	0.886	0.788	0.034	1.39	1.59	1.46	1.48

(B)

	X	Y	Z	anisotropy	X	Y	Z	
ε		R^2		Γ		E [Gpa]		average
1%	0.640	0.350	0.574	0.275	1.87	0.85	1.08	1.27
2%	0.867	0.787	0.868	0.161	1.65	1.1	1.39	1.38
3%	0.836	0.920	0.919	0.111	1.45	1.16	1.37	1.33
4%	0.871	0.951	0.948	0.063	1.33	1.23	1.32	1.29
5%	0.931	0.960	0.965	0.111	1.33	1.2	1.32	1.28
6%	**0.958**	**0.939**	**0.972**	**0.040**	**1.32**	**1.12**	**1.29**	**1.24**
7%	**0.941**	**0.956**	**0.964**	**0.089**	**1.25**	**1.13**	**1.24**	**1.21**
8%	**0.921**	**0.970**	**0.964**	**0.016**	**1.19**	**1.13**	**1.21**	**1.18**
9%	**0.915**	**0.978**	**0.952**	**0.030**	**1.14**	**1.13**	**1.16**	**1.14**
10%	**0.924**	**0.977**	**0.945**	**0.089**	**1.11**	**1.11**	**1.13**	**1.12**

(C)

	X	Y	Z	anisotropy	X	Y	Z	
ε		R^2		Γ		E [Gpa]		average
1%	0.033	0.372	0.642	0.588	0.37	0.81	1.46	0.88
2%	0.707	0.724	0.803	0.035	0.99	0.98	1.25	1.07
3%	0.863	0.881	0.896	0.034	1.13	1.17	1.2	1.17
4%	**0.925**	**0.926**	**0.939**	**0.039**	**1.21**	**1.18**	**1.23**	**1.21**
5%	**0.953**	**0.954**	**0.940**	**0.056**	**1.25**	**1.19**	**1.17**	**1.20**
6%	**0.967**	**0.967**	**0.951**	**0.069**	**1.25**	**1.18**	**1.14**	**1.19**
7%	**0.975**	**0.972**	**0.965**	**0.053**	**1.24**	**1.16**	**1.13**	**1.18**
8%	**0.961**	**0.975**	**0.975**	**0.053**	**1.19**	**1.14**	**1.14**	**1.16**
9%	**0.951**	**0.980**	**0.980**	**0.026**	**1.14**	**1.13**	**1.15**	**1.14**
10%	0.957	0.981	0.952	0.122	1.12	1.12	1.1	1.11

Figure 17: Results tables of Young's modulus for system C of PMDA-BIA in the continuous deformation mode for different strain rates at ambient pressure. The results for R2 and the anisotropy Γ were color-coded to indicate the following: green means a high level of matching the criteria, red means a low level of matching the criteria. Rows matching both criteria were highlighted in grey and their values are displayed bold. (A) Strain rate of 1 × 10−6 (fs−1). (B) Strain rate of 1 × 10−7 (fs−1). (C) Strain rate of 1 × 10−8 (fs−1).

2.4 Conclusions

In our present contribution, a method was described to predict the Young's modulus of the frequently used polyimide, namely Kapton®. Specifically, we used MD simulations with the

OPLS-AA force field to represent this popular polyimide. Additionally, the polymer PMDA-BIA was investigated as a second polyimide to get a better understanding of whether our procedure applies to polyimides in general or not.

A preparation procedure that allows for maximum flexibility in terms of using different materials is described. With this preparation method, a polymer can be used and adapted only by changing the geometry of the monomer. This was demonstrated by investigating the polymer PMDA-BIA additional to Kapton®, with the same workflow as described in our present work. The Young's modulus and the Poisson's ratio of the polymers were determined with two modes for different system sizes, different pressures, and temperatures.

For the investigated system in the relaxation mode, it was found that if the pressure is at 1 (atm) the system is breaking apart and will not have any calculable Young's modulus in the case of Kapton®. A similar behavior was found for PMDA-BIA, although the system did not break apart completely (Young's modulus at 1 atm was only 30% of the Young's modulus found at 750 atm). While the relaxation mode was strongly affected by a change in pressure, the continuous deformation mode simulations were strongly affected by the strain rate. The anisotropy Γ and the correlation coefficient R^2 (determined from a linear approximation of the stress and strain) were introduced to determine the configuration at which the system is most isotropic and behaves linear elastic. Due to this procedure, it is now possible to investigate the influence of different simulation boundary conditions, e.g., pressure and temperature, as objectively as possible. Compared to the literature data, our continuous deformation mode simulation at 10^{-6} (fs^{-1}) deformation rate replicated these results best. The Young's modulus of Kapton® of 2.5 GPa is in perfect agreement with literature values that range from 2.5 GPa [51] to 3.2 GPa [52]. Lei et al. [7] reported a Young's modulus of PMDA-BIA from a simulation of 5.37 GPa and referenced 8.5 GPa as the experimentally found Young's modulus of Song et al. [47], [53].

The investigation of the system size showed that—contrary to Ries et al. [47] —the system size has an impact on the results for the polyimides Kapton® and PMDA-BIA. The larger system behaved more isotropic and was less affected by the direction of deformation (both for compression and stretching). For future research in that area, it is important to determine a sufficient system size to ensure an isotropic behavior of the material. This also suggests future investigations regarding the optimal system size, i.e., the sweet spot between a low anisotropy parameter Γ and the computational effort spent.

Regarding the Poisson's ratio, the continuous deformation mode appears to be the more reliable one. The results of the continuous deformation mode simulations replicated the results from literature within their reported range for Kapton®. Both the results for system B with 0.33 and system C with around 0.38 [51]. However, the results from the relaxation mode simulations underestimate the Poisson's ratio in comparison to the literature data by 50% for system B. The Poisson's ratio for system C is about 25% underestimated. Unfortunately, there was no literature data on the Poisson's ratio for PMDA-BIA. However, the differences between relaxation mode and continuous deformation mode simulations were identical to that for Kapton®. Both systems B and C showed a higher Poisson's ratio in comparison to the simulations of Kapton®.

Our contribution showed that there is a pressure dependence when performing relaxation mode simulations, as suggested initially by Riccardi et al. [9]. Specifically, we find that for Kapton®, a pressure of 750 (atm) showed the best results for the Young's modulus in comparison with experimental data from the literature. Furthermore, at a pressure of 1 (atm), system B lost its structure and the simulation needed to be conducted at elevated pressures. Therefore, when investigating a homogeneous system, a simulation of the well-established tensile test is the more reliable way to obtain results that should replicate experimental values. In contrast, the relaxation mode is recommended to obtain a locally resolved determination of Young's modulus and Poisson's ratio, as described by Riccardi et al. [8], [9].

In summary, while Odegard et al. [10] already showed that the OPLS-AA force field can describe a single polyimide in MD simulations, we showed that this force field is also adequate for two other polyimides. This is of critical importance since future research may also be interested in other properties of polyimides (e.g., the diffusion behavior of ions) at different temperatures and molecular structures of the polymer. Since the OPLS-AA force field was built "… to give highly accurate descriptions of fluids" [34], we are optimistic that this force field can give a robust and accurate prediction for such applications. In future, this may allow researchers to simulate polyimides with a novel structure under extreme conditions that are difficult to replicate in a physical experiment.

3 Towards coarse-grained molecular dynamics simulations of polyimides: combining PC-SAFT theory, experiments and MD simulations

3.1 Introduction

A large number of applications involving polymers are related to the transport of ions and molecules in these materials [54]. Especially in corrosion processes it is important to understand limiting and accelerating factors that influence this transport of, e.g., corrosive gases, in order to protect industrial devices [2]. A detailed atomistic understanding of these transport processes can be achieved through molecular dynamics (MD) simulations: for example, effects such as the swelling behavior of polymers due to moisture absorption can be predicted without lengthy experiments [6]. With the results from MD simulations - first and foremost the diffusion coefficient of an ion or molecule - polymers can be rationally developed, and designed to provide better corrosion protection. Another topic is the usage of polymeric membranes both for separation of gases, as well as for fuel cells. Therefore, also the interest in understanding the underlying mechanisms of the diffusion process of different species through these membranes increased. MD simulations are also a useful tool to understand the influencing effects of these transport mechanisms [6], [15]. The ideas that came from membrane simulations can be transferred to investigations of protecting polymer films [55], [56].

In our present study the focus is on the transport properties of organic penetrator molecules in a polymer film that is used as a protective layer against corrosion. Specifically, our contribution shows how a mechanistic understanding of the diffusion behavior of molecules in a polymer film, namely the polyimide Kapton®, can be created by using MD simulations. On the one hand, this is important fundamental research, since often the diffusion coefficient cannot be determined quantitively in experiments, i.e., as is the case for permeability experiments [5] (in situations in which the solubility cannot be determined, or is unknown). Furthermore, this knowledge could be transferred to corrosive ions and molecules and allow the design of corrosion protective polymer films on the molecular level and improve the lifetime of the protected devices. Therefore, the goal of the present study was to determine the diffusion coefficient of an organic solvent, namely isopropanol, in Kapton® to investigate influences on the transport properties of the polyimide.

In membrane science, using MD simulations to investigate the transport properties of materials is a widely used tool already. For example, Neyertz et al. [15] investigated the diffusion based

on the concentration of the penetrator molecules (i.e., carbon dioxide) in three different polyimides. While they used the general force field TRIPOS 5.2, in the present work the more specific force field OPLS-AA [34] was used to allow for presumably more accurate results in simulations that include a liquid phase. They showed a concentration dependent diffusion coefficient and used a high penetrator concentration to allow for adequate statistics in terms of the number of atoms that were inserted in the polyimide matrix.

In general, the diffusion coefficient can be determined with MD simulations by monitoring the mean-squared-displacement (MSD) of an atom, a molecule, or a group of all species of the same type. If Fickian diffusion is present, the self-diffusion coefficient can be determined from the Einstein equation, as described in the methods section [15].

Müller-Plathe [57] and van der Vegt [58] state that for a small diffusion coefficient it is not possible to calculate the diffusion coefficient with the Einstein equation since feasible simulation times will be too short. In order to estimate the minimum simulation times, we used diffusion coefficients that were determined with experiments and the PC-SAFT continuum method and will be published in the future [59]. Based on the equation of Müller-Plathe [57] the minimum simulation time for isopropanol in Kapton® would be 2.4 ms, which would mean that the longest coarse-grained MD simulations conducted for the present work are too short by a factor of 5000.

System sizes are small in MD simulations, that often leads to statistical problems for the MSD. For example, the MSD might fluctuate in time if some of the investigated atoms are trapped in the polymer matrix. One way to overcome both challenges (i.e., long enough simulation times and large enough system sizes) is to reduce the number of interactions within the system by coarse-graining (CG) the all-atom (AA) simulation. Specifically, CG is the grouping of several atoms to beads with the goal to represent the AA behavior of the system as close as possible. Coarse-grained simulations are already used widely to investigate larger systems for longer times [60], [61], [62], [63].

Even coarse-grained simulations will not allow for the expected simulation times of 2.4ms (of isopropanol in a PI), that were mentioned above. However, it is important to prepare a blueprint that describes the necessary steps to obtain meaningful results once longer simulation times become computationally affordable. In our present work we present a way to conduct CG simulations with the combination of the software tools LAMMPS [20] and VOTCA [21], which are both already widely used. The advantage of using existing software and understanding how to use it is that not every researcher has to start from scratch with coding programs that allow

(i) the grouping of atoms to beads (ii) doing the statistical calculations for the radial distribution functions and (iii) conducting a complex CG procedure (e.g., an iterative Boltzmann inversion).

In order to provide a holistic view on the complete procedure, first AA simulations of (i) the pure substances, i.e., Kapton® and isopropanol, as well as (ii) a mixture of isopropanol and Kapton® were conducted. As a first step, these simulations were conducted to prepare physically correct systems that can be used as starting configuration for the CG procedure. Second, these simulations allowed a first understanding of trends, as it became apparent that with such short simulations times a sub-diffusive regime was present. Therefore, the AA simulations cannot be used to determine a diffusion coefficient. In the next step the results from the pure substance AA simulations were used to conduct the CG procedure with the pure substances, and investigate the results with the determined CG force fields. Although the CG systems behaved differently than the AA systems, the found force field parameters lead to stable simulations and allowed simulations of the target system, i.e. isopropanol in Kapton®.

The current chapter of the thesis is split into a thorough methods section that highlights the main parameters we identified that influence the quality of the coarse-graining procedure and the determination of the diffusion behavior primarily. In the results section first the findings from the AA simulations are presented, followed by the results of the CG simulations. The conclusion and outlook summarize our findings and open interesting research questions for the future.

3.2 Methods

3.2.1 MD

Molecular dynamics (MD) simulations allow us to determine atomistic states of molecular systems by solving Newton's equations of motion. The system has a certain initial state, that includes the initial coordinates of all atoms in the system. Based on so-called force fields (see below) the interactions between all atoms can be calculated respectively. With the known initial state, the forces between all atoms can be calculated, and numerically integrated. That way it is possible to simulate the motion of polymer chains, as well as penetrator molecules. Such MD simulations have been state of the art since many years, see [64].

The interactions are divided into bonded and non-bonded interactions. The bonded interactions summarize all intramolecular interactions that represent a bond between 2 atoms, the angle between 3 atoms as well as the out of plane and the torsional interaction between 4 atoms. In our case, the bonded interactions, except the torsional (dihedral) interactions, are calculated

based on a harmonic potential. A harmonic potential can be thought of as a spring between the atoms and is calculated with an equation of the form $E = K \cdot (x - x_0)^2$, where x_0 is the equilibrium bond distance or equilibrium angle in case of the harmonic angle potential, and K is a constant in the units of $\left[\frac{energy}{distance^2}\right]$ [20]. The dihedral interactions are calculated with the OPLS dihedral style in LAMMPS [20] which is based on a Ryckaert-Bellemans function and represents Fourier dihedrals [65].

Non-bonded interactions represent the coulombic and Van der Waals interactions between two intermolecular atoms within a certain distance. The non-bonded interactions in our study are calculated with an adapted 12-6 Lennard-Jones potential that is extended by a coulombic term [20].

In this work the Large-scale Atomic/Molecular Massively Parallel Simulator (LAMMPS) was used as the MD simulation software. The 2020 version of LAMMPS was used for all simulations described in this work. Furthermore, the 2023 version (30.11.2023) of the Versatile Object-oriented Toolkit for Coarse-graining (VOTCA) was used to conduct automated coarse-graining from LAMMPS simulations. Detailed information of the software used is provided in Appendix D – Software and Data Repositories.

3.2.2 Determination of Diffusion Coefficients

3.2.2.1 Self-diffusion

The self-diffusion coefficient can be determined either from a Green-Kubo integral, with the argument of the velocity auto correlation function (VACF) or from the mean-squared displacement (MSD) of a certain group of atoms. Haile [66] showed the derivation of the MSD form from the VACF form, which shows that both approaches are formally equivalent. Due to the simple calculation of the self-diffusion coefficients from the MSD this version was chosen.

Equation (3-1) shows the definition of the MSD [67], it can be tracked for every time step of the simulation.

$$MSD \equiv \frac{1}{N}\sum_{i=1}^{N}\left|r^{(i)}(t) - r^{(i)}(0)\right|^2 \tag{3-1}$$

If Brownian motion, i.e. the atoms follow a random walk, is present, the Einstein equation (see: equation (3-2)) can be used to calculate the self-diffusion coefficient from the long-time limit of the MSD [15]. The random walk condition is obtained when the MSDs are proportional to *t*, i.e. within the framework of a long-time Fickian diffusive limit [57].

$$D = \lim_{t\to\infty}\left(\frac{1}{6t}\left[\frac{1}{N}\sum_{i=1}^{N}\left|r^{(i)}(t) - r^{(i)}(0)\right|^2\right]\right) \tag{3-2}$$

Müller-Plathe [57] and van der Vegt [58] state that the second criterion to allow for equation (3-2) to be used for calculating the diffusion coefficient from the MSD is that the slope of the log-log plot of MSD over time is going to 1. Thus, equation (3-2) converges to a time-independent diffusion coefficient D if the MSD grows linearly with t.

3.2.2.2 Sub-Diffusion

If the MSD is not linearly changing with time, the Fickian diffusive limit is not reached, and anomalous diffusion is prevailing. In polymer systems the Fickian diffusion limit is often not achieved, simply because the atoms in these systems re-arrange relatively slowly. Tomasino et al. [68] state that in this case, it would be more correct to employ the generalized form of Einstein's equation. Rezayani et al. [69] present the generic version of the Einstein's equation (see: equation (3-3)) with an anomalous diffusion exponent *n*.

$$\langle\left(r_j(t) - r_j(0)\right)^2\rangle = MSD \sim 2dD_a t^n \tag{3-3}$$

Reformulating equation (3-3), one can calculate the anomalous diffusion coefficient as follows:

$$D_a \sim \frac{MSD}{6t^n} \tag{3-4}$$

Where *n* is defined via equation (3-5) and represents the slope of the MSD over time in a log-log plot.

$$n_{(t)} = \frac{d\ln\left(\langle\Delta r^2_{(t)}\rangle\right)}{d\ln(t)} \tag{3-5}$$

However, it is not possible to convert anomalous diffusion coefficients into meaningful diffusion coefficients (e.g., the Maxwell-Stefan diffusion coefficient introduced next).

In the present work the knowledge of sub-diffusion from the double logarithmic plots of the MSD allowed the discussion whether the simulation time is sufficiently long or if the Fickian diffusion limit was not reached yet.

3.2.2.3 Maxwell-Stefan diffusion coefficient

For reasons of comparison the self-diffusion coefficients need to be converted to Maxwell-Stefan diffusion coefficients. We note in passing that within the continuum theory (in form of

the PC-SAFT equation of state) that will be described later, Maxwell-Stefan diffusion coefficients are determined directly.

The conversion of the Maxwell-Stefan diffusion coefficients is based on the paper of Kubaczka [70]. His formulations are based on the theory of friction coefficients described by Bearman [71] and thoroughly investigated in the field of molecular dynamics by Vrentas and Vrentas [72], [73], [74]. This theory uses the self-diffusion coefficients of both materials, i.e. the pure polymer and the penetrator molecule (here: isopropanol), to calculate the friction coefficients for the specific system configuration. These friction coefficients can be used to determine the Maxwell-Stefan diffusion coefficient of the system. The interested reader is referred to the literature references above for further details or to Appendix C – Maxwell-Stefan diffusion from MD simulations.

3.2.3 System Preparation

As computational resources still are the most restricting component in MD simulations, researchers often build an equilibrated state, that (i) does not contain structural artifacts of the initialization, and that (ii) can be used as the initial state for the simulation of interest (e.g. apply an external electric field to investigate the diffusion of ions) to avoid unnecessary initial equilibration simulations.

One way to estimate if the system is sufficiently equilibrated is to track the radius of gyration and the mean-squared displacement. The system is treated as sufficiently equilibrated if on average the chains of the polymer have diffused some multiple of their radius of gyration [32]. There are different procedures to allow for a fast equilibration of the system. In this work we used the 21-step equilibration procedure described by Abbott et al. [33]. This procedure was used for each investigated system as the initial system preparation step. Regarding the system size, the systems in this work were prepared in the same manner as described in our previous work [75], in which we demonstrated that the polymer was modelled in a representative way.

For the combined system of isopropanol in Kapton®, absorption experiments were conducted to measure the equilibration concentration that is required to give estimates of realistic loadings of the MD simulations systems and to calculate the PC-SAFT parameters that allow an estimation of the Stefan-Maxwell diffusion coefficients. During these experiments the equilibration concentration was found to be above 3 wt%. Therefore, the two mass concentrations that were prepared for the MD simulations were for 1 wt% and 3 wt% isopropanol in the Kapton® matrix.

The mass concentrations were realized by inserting the correct number of isopropanol molecules to the system before the 21-step equilibration run to allow a random distribution of the molecules within the polymer chains. For System B, as defined in Table 3, this means that 102 isopropanol molecules were inserted for 1wt% concentration and 305 molecules for 3wt% concentration.

3.2.4 Production Runs

Two different system configurations of the polymer were investigated. It was decided to take the same system size as in our former work [75]: it was found that the system size, i.e. the number of atoms in the simulation has a significant impact on the results of the simulation. Therefore, a system size of 62'400 atoms was chosen, that already reproduced mechanical properties as the Young's modulus and the density accurately. Table 3 shows the systems were prepared with different chain lengths to determine the impact of the chain length on the diffusion. The maximal chain lengths used are based on preliminary calculations with the continuum model PC-SAFT, where results differed minimally at chain lengths above 200 monomers. To avoid excessive MD simulation times, longer chain lengths were avoided. Although the number of atoms is equal in both system A (SYS A) and B (SYS B) from Table 3, it was decided to conduct all simulations after this point with the configuration SYS B.

Table 3: System sizes, chain lengths and number of chains.

SYSTEM	CHAIN LENGTH	CHAINS
SYS A	40 monomers	40
SYS B	200 monomers	8

3.2.5 Statistical Considerations

As mentioned in the previous section, it is important to determine if there is a linear behavior between the MSD and time. In our simulations we identified that – next to the simulated time - the number of molecules that are sampled for the MSD had a significant impact on this behavior.

An estimation for the minimum simulation time was first mentioned by Müller-Plathe [57] and later formulated in an estimation equation by van der Vegt [58]. Using the jump distance of 5 to 10 Å suggested in their publications allowed us to estimate the minimum simulation time as already described in the introduction.

The second influencing metric, namely the number of atoms, was addressed by averaging over multiple simulations. Simulations with different starting configurations were conducted for each production run. Figure 18 shows the average MSD of three single simulation runs and shows

that the averaging smooths the MSD curve to allow for more accurate results. Furthermore, effects like trapped molecules that might appear in individual simulations are not impacting the result that much, as the sample size of diffusing molecules is getting larger due to the averaging of different simulations.

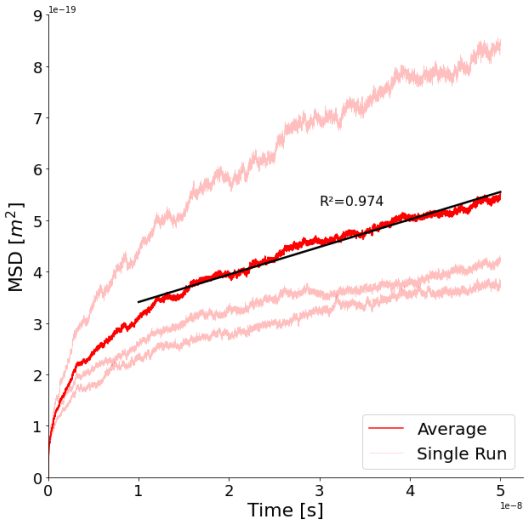

Figure 18: Comparison of average and single runs MSD data at 323 K and 1 atm for 50 ns (AA-MD simulation).

Additionally, coarse-grained simulations were conducted to allow the investigation of larger systems with a similar requirement regarding computational power. In our results section we report on the effect of both considerations.

3.2.6 Coarse-Graining

All-atom simulations can reflect the behavior of the polymer accurately. However, due to the comparably slow movements in terms of relaxation and diffusion of the polymer, the attainable timescales (of a few hundred nanoseconds) might be too short. Furthermore, to even reach these simulation durations, the system sizes are in the range of up to a maximum of 100 nm, in our case. Therefore, a method called coarse-graining is used to reduce the complexity of the all-atom simulation and to reduce the number of interactions that need to be calculated [63].

The basic idea of coarse-graining (CG) with respect to MD simulations is to reduce the number of atom-atom interactions in the simulation by grouping atoms to larger beads; e.g. grouping a benzene ring to a benzene bead (i.e., 12 atoms to 1 bead). The CG representation of the system needs to behave similarly to the AA simulation, to benefit from this approach. A well-established procedure to do that is using Boltzmann inversion: this method calculates a potential between two beads based on data for the radial distribution of the centers-of-mass (COMs) obtained from AA simulation. These potentials can either be used as (i) tabulated potentials, or (ii) can be transferred to parameters of a (harmonic) potential. The latter is subsequently used

in MD simulations to describe the bonded interactions, i.e., bonds, angles, proper and improper dihedrals [60], [76].

Figure 19 shows the grouping used in the present work. The definition of the beads was chosen (i) as informed by the chemistry, (ii) to prevent atoms being in two beads simultaneously, and (iii) was motivated by the grouping of Hu et al. [77].

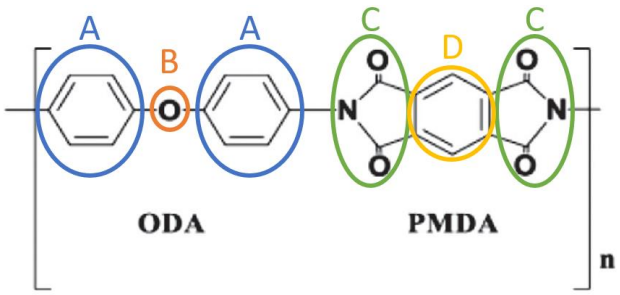

Figure 19: Schematic depiction of a possible grouping of the Kapton® monomer that was used in this work.

3.2.6.1 *Iterative Boltzmann Inversion (IBI) [63]*

In this work the IBI approach for obtaining the CG potential of Kapton® was followed. The iterative Boltzmann is the widest used method to obtain coarse-grained potentials due to its algorithmically simple scheme and good, i.e., fast convergence. As mentioned already in the introduction, the idea is to (i) define a reference bead-based representation from AA simulations, (ii) perform the coarse-grained simulations with an initial guess for the force field parameters, (iii) compare the radial distributions between the reference data and the coarse-grained simulation, and (iv) update the coarse-grained potential according to the update scheme shown in Equation (C-1). The initial guess is made by the software tool VOTCA automatically with a single Boltzmann inversion step.

$$u_i^{(k+1)}(r) = u_i^{(k)}(r) - \alpha \cdot k_B \cdot T \cdot \ln\left(\frac{g_{CG}^{(k)}(r)}{g_{AA}(r)}\right) \tag{3-6}$$

$u_i^{(k)}$ in equation (3-6) indicates the kth CG potential for a certain interaction distance r, e.g. bond between bead A and B from Figure 19, $g_{CG}^{(k)}(r)$ is the radial distribution function (RDF) for the interaction with the index *i* from the kth CG potential, $g_{AA}(r)$ is the AA target distribution, and α is a parameter that defines the magnitude of the potential update.

The disadvantage of this approach is that the interactions (indexed with *i*) are determined independently. Therefore, the convergence is slower and less stable than for the Inverse Monte Carlo method. However, as the preservation of structural quantities is given for both methods, we decided to use IBI as it does not require the acquisition of cross-correlated averages, which would add more complexity to the methodology [63].

Another CG approach would be to use the Martini force field that uses generic types of CG beads to represent the AA structure of the molecule [78], [79]. However, the idea in the present work is to further improve material properties on the atomistic level, which would be more difficult by using generic beads in contrast to beads that can be directly mapped back to an atomistic configuration.

3.2.6.2 Development of Coarse-Grained Potentials

Obtaining a stable force field for CG simulations is - aside from accurately reproducing results from AA simulations - the most important part of the CG procedure.

Although in literature [60], [77] dihedral interactions are not included to reduce the complexity of the system, we included these interactions at first. However, after investigating the determined potential (i) the potential was noisy which is no good behavior for a force field potential (since the first derivative of the potential represents the force between the beads) and (ii) the smoothed potential had a slope of nearly zero, which would represent very little forces between the beads regarding the torsion. Therefore, we did not include the dihedral interactions in simulations that are presented in the results section.

Through different iterations of the IBI procedure we ended up only determining the non-bonded interactions from the IBI runs and taking the already found interaction parameters for similar beads from Wen et al. [60] for the bonded interactions.

The results from the IBI are tabulated force field parameters, that determine the potential and hence the force between 2 types of beads at certain distances between these beads. To directly use these tabulated potentials in LAMMPS it is necessary to declare the "pair_style table" for nonbonded interactions. LAMMPS creates an interpolation table based on these tabulated potentials. In the LAMMPS documentation it is stated that the parameter N, that defines the number of entries in this interpolation table, should be equal to the number of entries in the tabulated potential file. The tabulated potential file is determined from the IBI to obtain a perfectly matched interpolation table to the calculated potential from the IBI [20]. However, in our simulations this was not the case as the interpolated potential that is used in the LAMMPS simulations was different from the obtained tabulated potential from the IBI. Therefore, we decided to use N for the interpolated table to be double the entries in the tabulated potential file. With this approach, we obtained a correctly interpolated potential for the LAMMPS CG simulations.

3.3 Results

The results section is split into 2 main parts: our results from AA simulations, and the results from CG simulations respectively.

3.3.1 AA Kapton®

In our prior work [75] we showed that the OPLS-AA force field can be used for the representation of Kapton® in an AA MD simulation. The detailed results can be found there, but it is important to mention that the starting system for the CG procedure is behaving physically accurate regarding density, Young's modulus and glass-transition temperature.

3.3.2 AA Isopropanol

As the matrix material was described well with the used force field, it was natural to also check if the diffusion properties of the material can be described accurately. Zangi et al. [80] already showed that the basic OPLS-AA force field [34] was not perfectly representing the behaviors of isopropanol and adapted the OPLS-AA parameters accordingly. In the present work we used the parameters Zangi et al. provided and conducted the production runs with 512 isopropanol molecules for 10 ns. Figure 62 and Figure 63 show the average MSD of three unique simulations over time and the double logarithmic plot. Both from the R-squared and the power law coefficient n that are shown in the figures it can be seen that these simulation results can be used to calculate the diffusion coefficients based on the MSD. Therefore, it can be assumed that the system size was chosen large enough to account for good statistics.

The self-diffusion coefficients were compared to the experimental data from Partington et al. [81] and were found to be in good agreement. The simulations were conducted at 294 K and the resulting diffusion coefficient of $D = 6.4 \cdot 10^{-10}\ \frac{m^2}{s}$ is within the range presented in literature from 15 °C to 25 °C. Furthermore, the density of $764\ \frac{kg}{m^3}$ is within 2.6% of the literature value of $785\ \frac{kg}{m^3}$.

Based on these findings, the applicability of the adapted OPLS-AA force field was verified, and the resulting systems can be used as the base for the coarse-graining procedure.

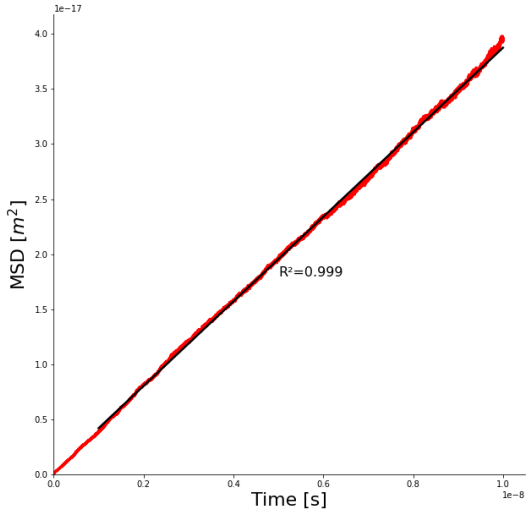

Figure 20: Isopropanol AA MSD (self-diffusion). Simulation at 294 K and 1 atm for 10 ns.

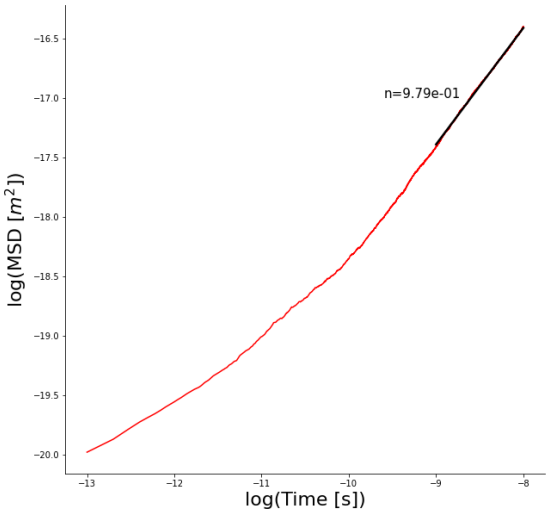

Figure 21: Isopropanol AA MSD (self-diffusion; double logarithmic plot). Simulation at 294 K and 1 atm for 10 ns.

3.3.3 AA Kapton® – Isopropanol

After the pure systems, i.e. pure isopropanol and pure Kapton®, were investigated, the combined system was prepared. As mentioned in the methods section, "SYS B" in Table 3 was used to conduct the simulations. The system was prepared as described in the methods section. The simulations were conducted at various temperatures and with various simulation durations. The main simulation results were taken from the 100 ns simulations at 323 K and 353 K. These temperatures were chosen as the experiments were conducted within this temperature range.

The most important parameter from these simulations is the slope of the double-logarithmic plot to see if it is possible to determine the self-diffusion coefficient from the Einstein equation (see Eqn. (3-2)). Figure 22 and Figure 23 show the double-logarithmic plots of the MSD, determined from 3 simulations respectively at 323 K and 353 K, for "SYS B" with 1 wt% of isopropanol molecules. The parameter *n* described in the graphs represents the slope of the graphs in the range from 10 ns to 100 ns. As can be seen, for 323 K $n = 0.2$, and at 353 K $n = 0.33$. Both of these factors are far from 1, which supports the assumption from the beginning that even these comparably long simulation times [6], [57], [82] are too short to determine the diffusion of isopropanol in Kapton®.

However, we calculated the self-diffusion coefficient with Eqn. (3-2) and used the calculated diffusion coefficient to determine the Stefan-Maxwell diffusion coefficient and compare it to the results from the experiments and the PC-SAFT approach. At 323 K $D_{MS} = 9.32 \cdot 10^{-15} \frac{m^2}{s}$ and at 353 K $D_{MS} = 2.38 \cdot 10^{-14} \frac{m^2}{s}$. Based on the results of the experiments and the PC-SAFT approach (to be published in a separate publication) the diffusion coefficients determined from

these simulations are more than two magnitudes of order higher than from experiments. This further implies that sub-diffusion is present [68], [69], [83] in this simulation, and that significantly longer simulation times are required.

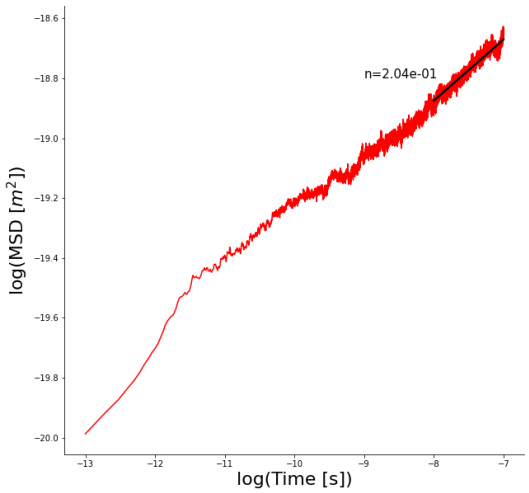

Figure 22: Double-logarithmic plot of MSD of isopropanol in Kapton® at 323 K and 1atm.

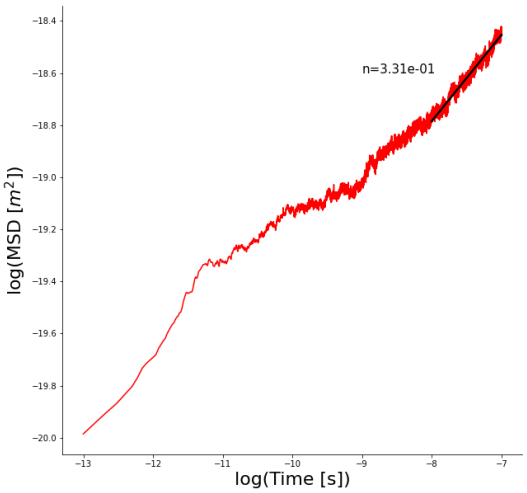

Figure 23: Double-logarithmic plot of MSD of isopropanol in Kapton® at 353 K and 1atm.

The most important finding here is that it is necessary to monitor the slope in the double-logarithmic graph. Although the linearity based on R-squared was high in the MSD plot (see: Figure 24), what would fulfill one criterion for the Einstein equation, the double-logarithmic plot (see: Figure 23) shows that the MSD is not linear over time.

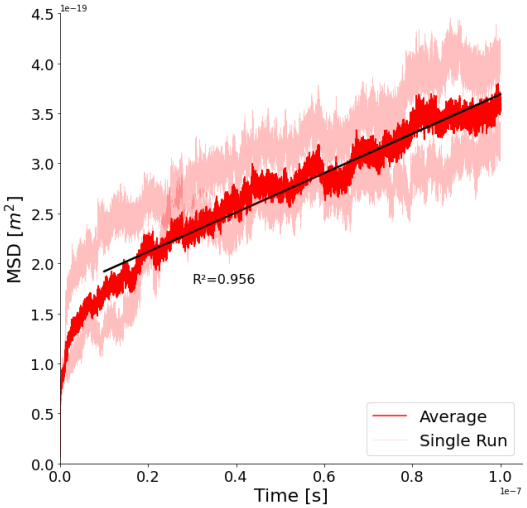

Figure 24: MSD for the AA simulation of 62'400 polymer atoms in 8 chains with 102 isopropanol molecules at 353 K and 1atm.

3.3.4 CG Isopropanol

The first step in the CG procedure was to investigate the behavior of the CG isopropanol. Therefore, initially a very coarse grouping was chosen that grouped the whole isopropanol

molecule to 1 bead as shown in Figure 26. The reason for this is the reduced complexity of the required force field as only 1 non-bonded interaction is necessary to describe the coarse-grained isopropanol system. As mentioned above, the AA simulations of 512 isopropanol molecules were used to create the radial distribution functions during the IBI.

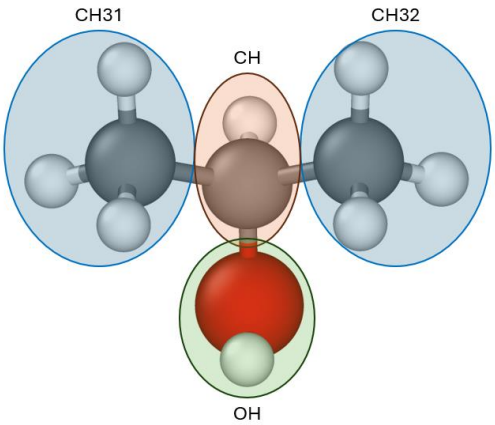

Figure 25: Grouping of isopropanol into 4 beads.

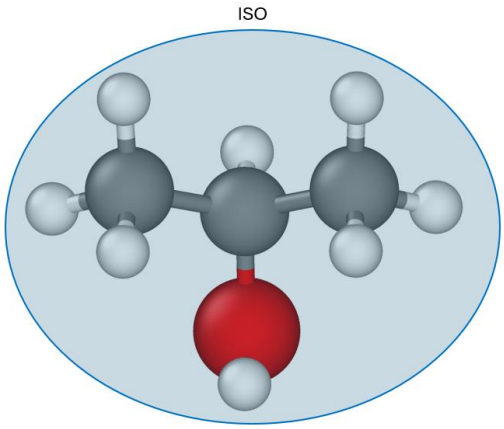

Figure 26: Grouping of isopropanol into 1 bead.

As the AA simulations already showed a linear behavior after 10 ns (see Figure 62 and Figure 63), the CG simulations were conducted for the same duration.

3.3.4.1 Results for 1-bead isopropanol

Simulations with the 1-bead configuration were conducted for 512 isopropanol molecules at 308 K as this was a temperature where literature data for the self-diffusion coefficient was available. The system reached an equilibrium density of 1297 $\frac{kg}{m^3}$, while still in a gaseous state, based on the measured temperature and pressure of the system.

By investigating the trajectories of the molecules, it became clear that the coarse grouping led to a crystallized system, that looked more like a metallic material than a gaseous system. Naturally, the diffusion coefficient was about zero as the molecules only vibrated in place after a short initial phase that showed randomness. Therefore, the next step was to prepare a less coarse system with 4 beads representing an isopropanol molecule, as shown in Figure 25.

3.3.4.2 Results for 4-bead isopropanol

The assumption for the 4-bead configuration of isopropanol (see Figure 25) was that the grid formation monitored in the 1-bead configuration will be broken up and the molecules will move freely in the system. The idea was that the different bead types will help in this approach. However, the system showed the same behavior and reconfigured in an oriented system where only a vibrational motion was present during the investigation of the trajectories.

Contrary to the 1-bead system the equilibration density in this configuration was $756\ \frac{kg}{m^3}$ which is within 4% of the density of isopropanol of $786\ \frac{kg}{m^3}$. Similar to the system with the 1-bead configuration, the diffusion coefficient was close to zero as well, as the system did not show diffusion except from short-distance vibrational motion.

One possibility for this could be the usage of tabulated potentials. These potentials are based on an equilibration state that is represented by the radial distribution functions for each interaction in AA simulations. The assumption is that the CG simulation is forced into a metastable state that only allows for small vibrations in place of the single bead. However, no relevant movements in terms of diffusive motion of the solvent were observed.

3.3.5 CG Kapton® – Isopropanol

Based on the findings of the CG simulations of both Kapton® and isopropanol it was decided to group the Kapton® as shown in Figure 19. As both configurations of isopropanol provided the same quality for the diffusion coefficient it was combined with the 1-bead configuration of isopropanol. The advantage of using the 1-bead configuration is the reduced complexity and hence the reduced required computational power.

The final force field used to conduct stable simulations up to 500 ns was a mixture of the conducted IBI for the nonbonded interactions, the skipping of dihedral interactions and the usage of already prepared CG parameters for similar interactions from Wen et al. [60].

While the density of the CG simulation of pure Kapton® was within 20% of the real density, in case of the system with Kapton® and isopropanol the density was too high. This fits with the findings from Demydiuk et al. [84]: they showed that with reduced torsional interactions the density increases. However, they showed a difference of the density between a full dihedral potential and a zero dihedral potential of only approximately 10%. In our case the density with switched off dihedral potential was $\rho = 2200\ \frac{kg}{m^3}$ and therefore about 50% higher than the literature value. This leads to the suggestion that the density correction method used by Hu et al. [77] would allow for better results regarding the density.

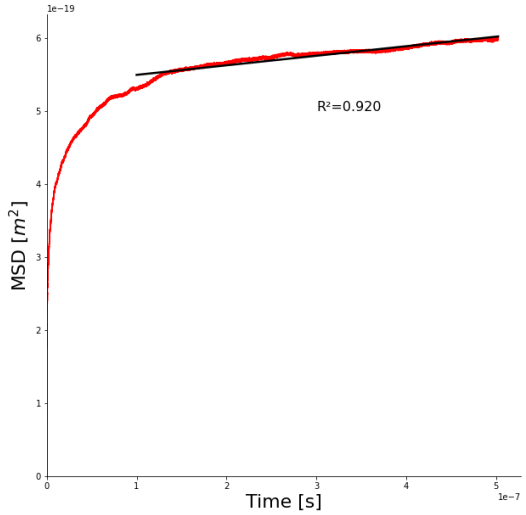

Figure 27: MSD for the CG simulation of 62'400 polymer atoms in 8 chains with 102 isopropanol molecules at 353 K and 1 atm for 500 ns.

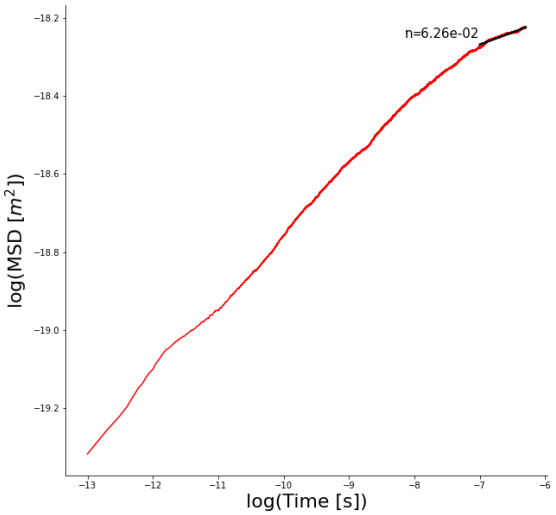

Figure 28: Double logarithmic plot of MSD for the CG simulation of 62'400 polymer atoms in 8 chains with 102 isopropanol molecules at 353 K and 1 atm for 500 ns.

Figure 27 shows the average MSD of three independent CG simulations of isopropanol in Kapton® over 500 ns. The CG systems consist of 62'400 atoms from the AA simulation that are coarse-grained to 9600 beads of Kapton® in 8 chains and the 102 isopropanol molecules. Figure 28 shows the double logarithmic plot of the MSD over the simulation time. Similarly to the results from the AA simulations, the slope of the double logarithmic graph is far from 1, which indicates that sub-diffusion is present.

The longer simulation times up to 500 ns did not bring the slope of the double logarithmic MSD towards 1, but even further away in comparison to the AA simulations with a duration of 100 ns.

3.4 Conclusion

In this work we presented a concept for conducting AA and CG simulations of an organic solvent in a polyimide material to determine the transport properties of the solvent. It was apparent that simulations at the moment will not lead to usable results, as required simulation times combined with large system sizes are not feasible with currently accessible computational power. However, the blueprint of how these simulations should be conducted - once it is possible to conduct AA MD or calibrated CG MD simulations - was presented.

In the first step the pure systems, i.e., Kapton® and isopropanol, were investigated with AA simulations to (i) determine if the used force field OPLS-AA can describe the individual systems and (ii) to prepare a reference AA system that can be used as the base for the CG procedure. Our previous work [75] and the presented results in this work for pure isopropanol showed that these systems can be described accurately with AA MD simulations. Furthermore, the

simulations of these species can be used as the starting configuration for the CG procedure with the IBI method.

The CG procedure was conducted with the software tool VOTCA [21] that allows an automated workflow of the iterative procedure (IBI). It also provides functions to determine the radial distribution functions (RDF) of the bonded and non-bonded interactions from AA simulations. It is further possible to automatically map the AA configuration to a CG configuration to allow the usage of an already equilibrated system that saves computational power. However, if compared to correct physical properties from literature, the simulations of pure Kapton® and pure isopropanol lead to better results than the simulations of the mixed system. It seems that the increased complexity of the CG system, namely the increased number of interactions due to different bead types, leads to difficulties in finding the correct CG force field. Skipping dihedral interactions lead to stable simulations, since IBI-based dihedral CG potentials were physically not meaningful. However, skipping the dihedral interactions leads to excessively high densities. Due to this high density, the reason for the sub-diffusive behavior of isopropanol in Kapton® as shown in Figure 28 remains unclear. On the one hand, the tabulated force field could be the reason that prevents an investigation of dynamic properties based on molecular movement. On the other hand, the high density could force the system into a state with little movement. Therefore, a density correction method that showed improved results in the work of Hu et al. [77] would be especially beneficial to the more complex system of isopropanol in Kapton®.

The combination with experimental values and determination of the diffusion coefficient with PC-SAFT method allowed an estimation of the required simulation time to achieve meaningful results with MD simulations. Even the longest simulations in this work with extreme coarse-graining, i.e., for Kapton® 39 atoms grouped to 6 beads and for isopropanol 12 atoms grouped to 1 bead, are by a factor of 5000 too short. Although the sufficient simulation times are not yet reachable, this work highlighted a few parameters that need to be considered once these long simulation times are affordable.

Dihedral interactions add a layer of complexity to the system, but are important to represent the density of the simulated system. The effect of adding a density correction method to the coarse-graining procedure on the diffusive behavior of the solvent would be an interesting starting point for future research.

Another important point of interest is the reason that even for longer simulations as shown in Figure 28, the slope of the double logarithmic MSD graph is not converging towards 1. Instead,

this slope even diverges from it in comparison to the 100 ns AA simulations that are shown in Figure 23. This behavior can stem from the high density as mentioned before. However, by comparing the behavior to the CG isopropanol simulations, diffusion could not be detected although the density was correct. As mentioned above, a possible explanation would be the crystallization that was seen in the analysis of the trajectories. Therefore, transferring the tabulated potentials to parameters for a Lennard-Jones potential, i.e. σ and ε, would be an interesting starting point to investigate this influence. The analytical solution of the Lennard-Jones potential might allow for more stability in the simulation in contrast to a discrete function. Another possibility from parcel-based approaches in discrete element methods, is either a slight variation in the size of the CG representation or a weak dilution of the system with a different species [85]. The first approach is similar to the simulation of isopropanol with the 1- and the 4-bead grouping. The latter approach was not tested in this work and would be an interesting point to investigate in the future.

Independent of the CG procedure and the software, it is necessary to check an obtained force field for its physical meaningfulness. For example, a potential that fluctuates strongly w.r.t to the distance is not acceptable as forces might change sign within a short distance. Automatic plotting and analysis of the derived CG potentials would help to address this challenge and accelerate research.

4 Conclusion

In this work, the possibility of investigating the transport properties of different species in polyimides with MD simulations was surveyed. A flexible framework was developed that allows researchers to

(i) prepare polymeric systems with different polymer types, chain lengths and number of chains, as well as penetrator molecules,
(ii) conduct AA simulations with the OPLS-AA force field, as well as CG simulations with calibrated CG force fields with the MD simulation software LAMMPS,
(iii) determine CG force fields based on AA simulations with the software tool VOTCA, and
(iv) determine properties like the glass-transition temperature, the Young's modulus the Poisson's ratio, the self- and Maxwell-Stefan diffusion coefficients with in-house postprocessing code written in python.

Before conducting MD simulations, a method had to be developed that allows to prepare a system of the polymer of interest (here: Kapton) flexibly, in terms of polymer chain length and number of polymer chains. As described in the first part of the thesis, moltemplate [31] was used to enable this flexibility. Based on bond lengths and angles, the structure, including the coordinates of each atom, of monomers can be described and prepared with moltemplate. Then this artificially created system was equilibrated with the method described in the first part of this thesis to prepare systems that are as close to the real system as possible.

In the first step, the applicability of the OPLS-AA force field to the polyimide and various diffusing species was investigated and verified. Although force fields like COMPASS were already proven to allow for correct simulations of polyimides [7], the OPLS-AA force field was chosen. The reason was that simulations with liquid phases were planned for future research. Simulations to determine the Young's modulus and the Poisson's ratio, similarly to the well-established tensile test, were conducted. The simulation results showed that the OPLS-AA force field can be used to describe the interactions in the Kapton polymer during uniaxial stretch and compression. However, the system size is of high importance as our investigation of an anisotropy metric showed. The system needs to have low anisotropy if the simulation should represent bulk properties of the polyimide. These findings were the first indication that the possibility of simulating larger system for longer times would be an important milestone when conducting MD simulations.

After verifying the applicability of the OPLS-AA force field to MD simulations of Kapton, simulations regarding the ion diffusion through the polyimide were conducted. The results of these simulations are presented in Appendix A – Atom and Ion diffusion. The idea was to simulate experiments of ion transport through a membrane that were previously conducted at Vienna University of Technology by Lars Varain [5]. However, the small system sizes of an MD simulation did not allow for the simulation of the complete process, including the ion absorption from the liquid phase into the membrane, the transport through the membrane and the desorption on the other side of the membrane. Therefore, the focus was set on the transport properties in the bulk of the polyimide. The diffusion coefficients of different ions were determined, based on their MSDs and the Einstein equation. However, due to the limited computational power the system sizes were too small and the simulation times too short to obtain good statistics. The presented results show sub-diffusive behavior as described in chapter 2. Experimental values from literature [86] are 8 orders of magnitude slower than indentified in the present simulations. Clearly, longer simulations, as described in part two of the thesis, would be interesting points for future research.

Müller-Plathe [57] also states that 10 ns long simulations bring diffusion coefficients of $4 \cdot 10^{-11} \frac{m^2}{s}$ within reach. The longest simulations in this thesis were 500 ns long. Therefore, it is necessary to investigate ways to allow longer simulations with the available computation power. The reoccurring topic of computational power to be the bottleneck of this research lead to the results described in the second part of the thesis, where the coarse graining of polymeric systems was investigated.

This second part of the thesis dealt with the determination of a coarse-grained force fields for an organic solvent, namely isopropanol, in the polyimide Kapton. This system was chosen, as the experimentally determined absorption of isopropanol in Kapton showed promising results for good statistics in comparison to other organic solvents. These experiments in combination with the continuum method PC-SAFT, conducted by Stefan Wagner from Graz University of Technology, allowed an estimation of the diffusion coefficient of this system. The determined Maxwell-Stefan diffusion coefficients can be used as verification for the MD simulations conducted in the present work. A blueprint was presented that allows researchers to determine a CG force field based on AA simulations and determine self-diffusion as well as Maxwell-Stefan diffusion coefficients for diffusing species in a polymer matrix. The estimation of the diffusion time from the continuum method made it clear that conducting long enough simulations to describe the diffusion process properly is out of reach with the computational

power available for the present research. However, it was important to present the correct way to conduct simulations for investigating the transport properties of these species. The combination of the MD simulation tools LAMMPS and VOTCA, a toolbox to conduct coarse graining methods automatically, is presented in Appendix B – The VOTCA / LAMMPS Interface. The VOTCA tool presents tutorials for both simple and complex systems in combination with GROMACS [65]. When starting the present work, there was no thoroughly described tutorial for conducting the coarse-graining with VOTCA based on AA simulations from LAMMPS for complex systems. We hope this guide will support researchers in the future to allow a faster setup of CG simulations with the presented tools. Another possibility is the widely used coarse grained force field MARTINI [78]. However, for more flexibility in the application of the force field, as it is only determined by AA simulations verified beforehand, the combination of LAMMPS and VOTCA was chosen in the present work.

The way to determine if a Fickian or sub-diffusive regime is present from MD simulation data was presented. Furthermore, the calculation of the Maxwell-Stefan diffusion coefficient based on self-diffusion coefficients was summarized in Appendix C – Maxwell-Stefan diffusion from MD simulations.

5 Outlook

The most important point for future research would be the determination of a stable CG force field that allows simulations up to the required times calculated in chapter 2 of the present thesis. Consequently, there are various ways to improve the presented method:

I. Sample bonded interaction RDFs only from single polymer chains [60]
II. Add the density correction to the coarse-graining method [77]
III. Investigate the improvement by using pair coefficients instead of tabulated potentials

An interesting point for future research will also be the investigation of the sub-diffusive behavior, and if a correct diffusion coefficient can be determined with shorter simulations. Tomasino et al. [68] and Berrod et al. [83] have presented generic versions of the Einstein equation that could be used to calculate a diffusion coefficient from MSDs that do not have a slope of 1 in a double logarithmic plot over time.

Once stable CG force fields are found, the method described in the first chapter (i.e., to determine the Young's modulus of the polymer) would allow the validation of the force field by comparison with experimental mechanical properties. In other words, combining the findings from chapter 1 and 2 would improve the validation of the found CG force fields.

Subsequently, the original goal of chapter 2 (i.e., combining atomistic simulations with a continuum method, e.g. PC-SAFT, to describe the transport properties in polyimides) could be followed.

6 Bibliography

[1] S. Neyertz and D. Brown, "An optimized fully-atomistic procedure to generate glassy polymer films for molecular dynamics simulations," *Comput Mater Sci*, vol. 174, no. November 2019, p. 109499, Mar. 2020, doi: 10.1016/j.commatsci.2019.109499.

[2] L. Varain, "Electrochemical Investigation of Ion Diffusion through Polymer Membranes in Combination with FEM Modelling," 2019.

[3] J. Seo and H. Han, "Water diffusion studies in polyimide thin films," *J Appl Polym Sci*, vol. 82, no. 3, pp. 731–737, 2001, doi: 10.1002/app.1899.

[4] A. Sezer Hicyilmaz and A. Celik Bedeloglu, "Applications of polyimide coatings: a review," Mar. 01, 2021, *Springer Nature*. doi: 10.1007/s42452-021-04362-5.

[5] L. Varain, S. Larisegger, M. Nelhiebel, and G. Fafilek, "Simultaneous measurement and ODE-modeling of ion- and water permeability through ion exchange membranes," *J Memb Sci*, vol. 684, Oct. 2023, doi: 10.1016/j.memsci.2023.121847.

[6] S. Neyertz and D. Brown, "Molecular dynamics simulations of oxygen transport through a fully atomistic polyimide membrane," *Macromolecules*, vol. 41, no. 7, pp. 2711–2721, 2008, doi: 10.1021/ma7026676.

[7] H. Lei, S. Qi, and D. Wu, "Hierarchical multiscale analysis of polyimide films by molecular dynamics simulation: Investigation of thermo-mechanical properties," *Polymer (Guildf)*, vol. 179, no. April, p. 121645, Sep. 2019, doi: 10.1016/j.polymer.2019.121645.

[8] E. Riccardi, C. B. Michael, and M. Florian, "Molecular dynamics method to locally resolve Poisson ' s ratio : Mechanical description of the solid – soft-matter interphase," *Phys Rev E*, vol. 86, no. 3, pp. 1–11, 2012, doi: 10.1103/PhysRevE.86.036704.

[9] E. Riccardi, M. C. Böhm, and F. Müller-Plathe, "Molecular dynamics approach to locally resolve elastic constants in nanocomposites and thin films: Mechanical description of solid-soft matter interphases via Young's modulus, Poisson's ratio and shear modulus," *The European Physical Journal E*, vol. 37, no. 103, Oct. 2014, doi: 10.1140/epje/i2014-14103-5.

[10] G. M. Odegard, T. C. Clancy, and T. S. Gates, "Prediction of mechanical properties of polymers with various force fields," in *Collection of Technical Papers* -

AIAA/ASME/ASCE/AHS/ASC Structures, Structural Dynamics and Materials Conference, 2005, pp. 586–597. doi: 10.2514/6.2005-1850.

[11] S. Neyertz, "Molecular dynamics simulations of helium permeation in polyimides with a bulky dianhydride and a fluorinated diamine," *Macromol Theory Simul*, vol. 16, no. 5, pp. 513–524, 2007, doi: 10.1002/mats.200700017.

[12] S. Neyertz and D. Brown, "Single- and mixed-gas sorption in large-scale molecular models of glassy bulk polymers. Competitive sorption of a binary CH4/N2 and a ternary CH4/N2/CO2 mixture in a polyimide membrane," *J Memb Sci*, vol. 614, no. June, p. 118478, 2020, doi: 10.1016/j.memsci.2020.118478.

[13] G. Marque, S. Neyertz, J. Verdu, V. Prunier, and D. Brown, "Molecular dynamics simulation study of water in amorphous Kapton," *Macromolecules*, vol. 41, no. 9, pp. 3349–3362, 2008, doi: 10.1021/ma702173j.

[14] S. Pandiyan, D. Brown, S. Neyertz, and N. F. A. Van Der Vegt, "Carbon dioxide solubility in three fluorinated polyimides studied by molecular dynamics simulations," *Macromolecules*, vol. 43, no. 5, pp. 2605–2621, 2010, doi: 10.1021/ma902507d.

[15] S. Neyertz, D. Brown, S. Pandiyan, and N. F. A. Van Der Vegt, "Carbon dioxide diffusion and plasticization in fluorinated polyimides," *Macromolecules*, vol. 43, no. 18, pp. 7813–7827, 2010, doi: 10.1021/ma1010205.

[16] L. Varain, "Electrochemical Investigation and Modeling of Ion- and Water Transport Through Polymer Membranes," Vienna University of Technology, Vienna, 2022.

[17] Y. Choo, D. M. Halat, I. Villaluenga, K. Timachova, and N. P. Balsara, "Diffusion and migration in polymer electrolytes," *Prog Polym Sci*, vol. 103, p. 101220, 2020, doi: 10.1016/j.progpolymsci.2020.101220.

[18] T. Mabuchi, K. Nakajima, and T. Tokumasu, "Molecular dynamics study of ion transport in polymer electrolytes of all-solid-state li-ion batteries," *Micromachines (Basel)*, vol. 12, no. 9, 2021, doi: 10.3390/mi12091012.

[19] D. Diddens and A. Heuer, "Lithium Ion Transport Mechanism in Ternary Polymer Electrolyte- Ionic Liquid Mixtures: A Molecular Dynamics Simulation Study," *ACS Macro Lett*, no. 3, pp. 322–326, Apr. 2013.

[20] The LAMMPS Developers, "LAMMPS DOCUMENTATION," 2024. Accessed: Feb. 12, 2024. [Online]. Available: https://docs.lammps.org/Manual.pdf

[21] V. Ru, C. Junghans, A. Lukyanov, K. Kremer, and D. Andrienko, "Versatile Object-Oriented Toolkit for Coarse-Graining Applications," pp. 3211–3223, 2009.

[22] L. W. McKeen, "6 - Polyimides," L. W. B. T.-T. E. of L. T. T. E. on P. and E. McKeen, Ed., Oxford: William Andrew Publishing, 2014, pp. 117–137. doi: https://doi.org/10.1016/B978-0-323-22108-5.00006-0.

[23] G. Lee, Y. Kim, and D. Kwon, "Mechanical characterization of polymer passivation layer in semiconductor applications using IIT and FEA," *Microelectron Eng*, vol. 87, no. 11, pp. 2288–2293, 2010, doi: 10.1016/j.mee.2010.03.005.

[24] W. L. Jorgensen and J. Tirado-Rives, "Potential energy functions for atomic-level simulations of water and organic and biomolecular systems," *Proceedings of the National Academy of Sciences*, vol. 102, no. 19, pp. 6665–6670, May 2005, Accessed: Jan. 02, 2025. [Online]. Available: www.pnas.org/cgi/doi/10.1073/pnas.0408037102

[25] D. N. Theodorou and U. W. Suter, "Atomistic modeling of mechanical properties of polymeric glasses," *Macromolecules*, vol. 19, no. 1, pp. 139–154, Jan. 1986, doi: 10.1021/ma00155a022.

[26] D. Brown and J. H. R. Clarke, "Molecular dynamics simulation of an amorphous polymer under tension. 1. Phenomenology," *Macromolecules*, vol. 24, no. 8, pp. 2075–2082, Apr. 1991, doi: 10.1021/ma00008a056.

[27] A. V. Lyulin, N. K. Balabaev, M. A. Mazo, and M. A. J. Michels, "Molecular dynamics simulation of uniaxial deformation of glassy amorphous atactic polystyrene," *Macromolecules*, vol. 37, no. 23, pp. 8785–8793, 2004, doi: 10.1021/ma049737p.

[28] V. M. Nazarychev, A. V. Lyulin, S. V. Larin, A. A. Gurtovenko, J. M. Kenny, and S. V. Lyulin, "Molecular dynamics simulations of uniaxial deformation of thermoplastic polyimides," *Soft Matter*, vol. 12, no. 17, pp. 3972–3981, 2016, doi: 10.1039/c6sm00230g.

[29] A. P. Thompson *et al.*, "LAMMPS - a flexible simulation tool for particle-based materials modeling at the atomic, meso, and continuum scales," *Comput Phys Commun*, vol. 271, p. 108171, 2022, doi: 10.1016/j.cpc.2021.108171.

[30] M. M. D. Ramos, A. M. Stoneham, and A. P. Sutton, "Aluminum Polyimide Adhesion," *Acta metallurgica et materialia*, vol. 41, no. 7, pp. 2105–2111, 1993.

[31] A. I. Jewett *et al.*, "Moltemplate: A Tool for Coarse-Grained Modeling of Complex Biological Matter and Soft Condensed Matter Physics," *J Mol Biol*, vol. 433, no. 11, p. 166841, 2021, doi: 10.1016/j.jmb.2021.166841.

[32] T. E. Gartner and A. Jayaraman, "Modeling and Simulations of Polymers: A Roadmap," *Macromolecules*, vol. 52, no. 3, pp. 755–786, Feb. 2019, doi: 10.1021/acs.macromol.8b01836.

[33] L. J. Abbott, K. E. Hart, and C. M. Colina, "Polymatic: A generalized simulated polymerization algorithm for amorphous polymers," *Theor Chem Acc*, vol. 132, no. 3, pp. 1–19, 2013, doi: 10.1007/s00214-013-1334-z.

[34] W. L. Jorgensen, D. S. Maxwell, and J. Tirado-Rives, "Development and testing of the OPLS all-atom force field on conformational energetics and properties of organic liquids," *J Am Chem Soc*, vol. 118, no. 45, pp. 11225–11236, 1996, doi: 10.1021/ja9621760.

[35] J. A. Rackers *et al.*, "Tinker 8: Software Tools for Molecular Design," *J Chem Theory Comput*, vol. 14, no. 10, pp. 5273–5289, 2018, doi: 10.1021/acs.jctc.8b00529.

[36] P. Feenstra, M. Brunsteiner, and J. Khinast, "Prediction of drug-packaging interactions via molecular dynamics (MD) simulations," *Int J Pharm*, vol. 431, no. 1–2, pp. 26–32, 2012, doi: 10.1016/j.ijpharm.2012.03.049.

[37] J. L. Barrat, J. Baschnagel, and A. Lyulin, "Molecular dynamics simulations of glassy polymers," *Soft Matter*, vol. 6, no. 15, pp. 3430–3446, 2010, doi: 10.1039/b927044b.

[38] D. Hossain, M. A. Tschopp, D. K. Ward, J. L. Bouvard, P. Wang, and M. F. Horstemeyer, "Molecular dynamics simulations of deformation mechanisms of amorphous polyethylene," *Polymer (Guildf)*, vol. 51, no. 25, pp. 6071–6083, 2010, doi: 10.1016/j.polymer.2010.10.009.

[39] R. Pan, X. Liu, A. Zhang, and Y. Gu, "Molecular simulation on structure-property relationship of polyimides with methylene spacing groups in biphenyl side chain," *Comput Mater Sci*, vol. 39, no. 4, pp. 887–895, 2007, doi: 10.1016/j.commatsci.2006.10.019.

[40] B. T. Low, Y. Xiao, and T. S. Chung, "Amplifying the molecular sieving capability of polyimide membranes via coupling of diamine networking and molecular architecture," *Polymer (Guildf)*, vol. 50, no. 14, pp. 3250–3258, 2009, doi: 10.1016/j.polymer.2009.04.059.

[41] X. Liu, "A Study on Patent Compulsory License System in China – With Particular Reference to the Drafted 3rd Amendment to the Patent Law of the P.R. of China," *Patents and Technological Progress in a Globalized World*, vol. 6, no. 2009, pp. 115–126, 2008, doi: 10.1007/978-3-540-88743-0_10.

[42] S. Goyal *et al.*, "Characterizing the Fundamental Adhesion of Polyimide Monomers on Crystalline and Glassy Silica Surfaces: A Molecular Dynamics Study," *Journal of Physical Chemistry C*, vol. 120, no. 41, pp. 23631–23639, 2016, doi: 10.1021/acs.jpcc.6b08081.

[43] M. Ries, F. Weber, M. Striegel, P. Steinmann, and S. Pfaller, "Multiscale fe-md coupling: Influence of the chain length on the mechanical behavior of coarse-grained polystyrene," *World Congress in Computational Mechanics and ECCOMAS Congress*, vol. 300, no. January, pp. 1–12, 2021, doi: 10.23967/wccm-eccomas.2020.214.

[44] C. R. Siviour and J. L. Jordan, "High Strain Rate Mechanics of Polymers: A Review," *Journal of Dynamic Behavior of Materials*, vol. 2, no. 1, pp. 15–32, 2016, doi: 10.1007/s40870-016-0052-8.

[45] W. Schnell, D. Gross, and W. Hauger, *Technische Mechanik*, 6th ed. in Springer-Lehrbuch. Berlin, Heidelberg: Springer Berlin Heidelberg, 1998. doi: 10.1007/978-3-662-22466-3.

[46] Dupont (USA), "DuPont Kapton - Summary of Properties," 2021. [Online]. Available: http://www.dupont.com/content/dam/dupont/products-and-services/membranes-and-films/polyimde-films/documents/DEC-Kapton-summary-of-properties.pdf

[47] M. Ries, G. Possart, P. Steinmann, and S. Pfaller, "Extensive CGMD simulations of atactic PS providing pseudo experimental data to calibrate nonlinear inelastic continuum mechanical constitutive laws," *Polymers (Basel)*, vol. 11, no. 11, pp. 1–25, 2019, doi: 10.3390/polym11111824.

[48] W. Y. Chang, T. H. Fang, and Y. C. Lin, "Physical characteristics of polyimide films for flexible sensors," *Appl Phys A Mater Sci Process*, vol. 92, no. 3, pp. 693–701, 2008, doi: 10.1007/s00339-008-4623-y.

[49] C. T. Kuo, M. C. Yip, K. N. Chiang, and C. Tsou, "Characterization study of time- and temperature-dependent mechanical behavior of polyimide materials in electronic packaging applications," *J Electron Mater*, vol. 34, no. 3, pp. 272–281, 2005, doi: 10.1007/s11664-005-0213-3.

[50] M. Rahimi, I. Iriarte-Carretero, A. Ghanbari, M. C. Böhm, and F. Müller-Plathe, "Mechanical behavior and interphase structure in a silica-polystyrene nanocomposite under uniaxial deformation," *Nanotechnology*, vol. 23, no. 30, 2012, doi: 10.1088/0957-4484/23/30/305702.

[51] "Material Property Database." Accessed: Aug. 07, 2023. [Online]. Available: https://www.mit.edu/~6.777/matprops/polyimide.htm

[52] M. Miyauchi, K. I. Kazama, T. Sawaguchi, and R. Yokota, "Dynamic tensile properties of a novel Kapton-type asymmetric polyimide derived from 2-phenyl-4,4'-diaminodiphenyl ether," *Polym J*, vol. 43, no. 10, pp. 866–868, 2011, doi: 10.1038/pj.2011.67.

[53] G. Song *et al.*, "Rigidity enhancement of polyimides containing benzimidazole moieties," *J Appl Polym Sci*, vol. 130, no. 3, pp. 1653–1658, Nov. 2013, doi: 10.1002/app.39324.

[54] S. Neyertz and D. Brown, "An optimized fully-atomistic procedure to generate glassy polymer films for molecular dynamics simulations," *Comput Mater Sci*, vol. 174, no. October 2019, p. 109499, 2020, doi: 10.1016/j.commatsci.2019.109499.

[55] L. Y. Ma, N. Soin, S. N. Aidit, F. A. Md Rezali, and S. F. Wan Muhamad Hatta, "Recent advances in flexible solution-processed thin-film transistors for wearable electronics," Oct. 01, 2023, *Elsevier Ltd.* doi: 10.1016/j.mssp.2023.107658.

[56] P. Grzybek, G. Dudek, and B. van der Bruggen, "Cellulose-based films and membranes: A comprehensive review on preparation and applications," Sep. 01, 2024, *Elsevier B.V.* doi: 10.1016/j.cej.2024.153500.

[57] F. Müller-Plathe, "Permeation of polymers — a computational approach," *Acta Polymerica*, vol. 45, no. 4, pp. 259–293, 1994, doi: 10.1002/actp.1994.010450401.

[58] N. F. A. Van Der Vegt, "Temperature dependence of gas transport in polymer melts: Molecular dynamics simulations of CO2 in polyethylene," *Macromolecules*, vol. 33, no. 8, pp. 3153–3160, Apr. 2000, doi: 10.1021/ma991737f.

[59] S. Wagner, "Personal Communication," Jul. 2024, *Graz*.

[60] C. Wen, R. Odle, and S. Cheng, "Coarse-Grained Molecular Dynamics Modeling of a Branched Polyetherimide," *Macromolecules*, vol. 54, no. 1, pp. 143–160, 2021, doi: 10.1021/acs.macromol.0c01440.

[61] M. P. Bernhardt, M. Hanke, and N. F. A. Van Der Vegt, "Stability, Speed, and Constraints for Structural Coarse-Graining in VOTCA," *J Chem Theory Comput*, 2022, doi: 10.1021/acs.jctc.2c00665.

[62] S. Pandiyan, P. V. Parandekar, O. Prakash, T. K. Tsotsis, and S. Basu, "Systematic coarse graining of a high-performance polyimide," *Macromol Theory Simul*, vol. 24, no. 5, pp. 513–520, 2015, doi: 10.1002/mats.201500009.

[63] S. Dhamankar and M. A. Webb, "Chemically specific coarse-graining of polymers: Methods and prospects," *Journal of Polymer Science*, vol. 59, no. 22, pp. 2613–2643, 2021, doi: 10.1002/pol.20210555.

[64] M. P. Allen, "Introduction to Molecular Dynamics Simulation," *Computational Soft Matter*, vol. 23, pp. 1–28, 2004.

[65] GROMACS development team, "GROMACS Documentation," Oct. 19, 2023. Accessed: Oct. 15, 2024. [Online]. Available: https://manual.gromacs.org/2023.3/manual-2023.3.pdf

[66] J. M. Haile, *Molecular Dynamics Simulation*, 1st ed. New York: Wiley-Interscience, 1997.

[67] D. Frenkel and B. Smit, *Understanding molecular simulation from algorithms to applications*, 2nd ed. San Diego: ACADEMIC PRESS, 2002.

[68] E. Tomasino, B. Mukherjee, V. D. Neelalochana, P. Scardi, and N. Ataollahi, "Computational Modeling of Hydrated Polyamine-Based Anion Exchange Membranes via Molecular Dynamics Simulation," *Journal of Physical Chemistry C*, vol. 128, no. 1, pp. 623–634, Jan. 2024, doi: 10.1021/acs.jpcc.3c07118.

[69] M. Rezayani, F. Sharif, and H. Makki, "Understanding ion diffusion in anion exchange membranes; effects of morphology and mobility of pendant cationic groups," *J Mater Chem A Mater*, vol. 10, no. 35, pp. 18295–18307, Aug. 2022, doi: 10.1039/d2ta04400e.

[70] A. Kubaczka, "Prediction of Maxwell-Stefan diffusion coefficients in polymer-multicomponent fluid systems," Nov. 15, 2014, *Elsevier*. doi: 10.1016/j.memsci.2014.06.055.

[71] B. J. Richard Bearman and of Gordon, "On The Molecular Basis of Some Current Theories of Diffusion," *J Phys Chem*, vol. 65, no. 11, Nov. 1961, doi: 10.1021/j100828a012.

[72] J. S. Vrentas and C. M. Vrentas, "Prediction of mutual diffusion coefficients for polymer-solvent systems," *J Appl Polym Sci*, vol. 77, no. 14, pp. 3195–3199, Jan. 2000, doi: 10.1002/1097-4628(20000929)77:14<3195::AID-APP210>3.0.CO;2-Q.

[73] J. S. Vrentas and C. M. Vrentas, "A New Equation Relating Self-Diffusion and Mutual Diffusion Coefficients in Polymer-Solvent Systems," *Macromolecules*, vol. 26, no. 22, pp. 6129–6131, Sep. 1993, doi: 10.1021/ma00074a040.

[74] J. S. Vrentas and C. M. Vrentas, "Restrictions on friction coefficients for binary and ternary diffusion," *Ind Eng Chem Res*, vol. 46, no. 10, pp. 3422–3428, May 2007, doi: 10.1021/ie061593a.

[75] P. Rosenauer, C. Kratzer, S. Larisegger, and S. Radl, "Extraction of Mechanical Parameters via Molecular Dynamics Simulation: Application to Polyimides," *Polymers (Basel)*, vol. 16, no. 6, p. 813, Mar. 2024, doi: 10.3390/polym16060813.

[76] E. Lin, X. You, R. M. Kriegel, R. D. Moffitt, and R. C. Batra, "Atomistic to coarse grained simulations of diffusion of small molecules into polymeric matrix," *Comput Mater Sci*, vol. 138, pp. 448–461, Oct. 2017, doi: 10.1016/j.commatsci.2017.07.011.

[77] C. Hu, T. Lu, and H. Guo, "Developing a Transferable Coarse-Grained Model for the Prediction of Thermodynamic, Structural, and Mechanical Properties of Polyimides at Different Thermodynamic State Points," *J Chem Inf Model*, vol. 59, no. 5, pp. 2009–2025, May 2019, doi: 10.1021/acs.jcim.8b00887.

[78] S. J. Marrink, H. J. Risselada, S. Yefimov, D. P. Tieleman, and A. H. De Vries, "The MARTINI force field: Coarse grained model for biomolecular simulations," *Journal of Physical Chemistry B*, vol. 111, no. 27, pp. 7812–7824, Jul. 2007, doi: 10.1021/jp071097f.

[79] R. Alessandri, S. Thallmair, C. G. Herrero, R. Mera-Adasme, S. J. Marrink, and P. C. T. Souza, "A Practical Introduction to Martini 3 and its Application to Protein-Ligand Binding Simulations," in *A Practical Guide to Recent Advances in Multiscale Modeling and*

Simulation of Biomolecules, AIP Publishing LLCMelville, New York, 2023, pp. 1-1-1–34. doi: 10.1063/9780735425279_001.

[80] R. Zangi, "Refinement of the OPLSAA Force-Field for Liquid Alcohols," *ACS Omega*, vol. 3, no. 12, pp. 18089–18099, Dec. 2018, doi: 10.1021/acsomega.8b03132.

[81] J. R. Partington, R. F. Hudson, and K. W. Bagnall, "Self-diffusion of Aliphatic Alcohols," *Nature*, vol. 169, pp. 583–584, Apr. 1952.

[82] K. Kremer and F. Müller-Plathe, "Multiscale simulation in polymer science," in *Molecular Simulation*, Jan. 2002, pp. 729–750. doi: 10.1080/0892702021000002458.

[83] Q. Berrod, S. Hanot, A. Guillermo, S. Mossa, and S. Lyonnard, "Water sub-diffusion in membranes for fuel cells," *Sci Rep*, vol. 7, no. 1, Dec. 2017, doi: 10.1038/s41598-017-08746-9.

[84] F. Demydiuk, M. Solar, H. Meyer, O. Benzerara, W. Paul, and J. Baschnagel, "Role of torsional potential in chain conformation, thermodynamics, and glass formation of simulated polybutadiene melts," *J Chem Phys*, no. 23, Nov. 2022, doi: 10.1063/5.0094536ï.

[85] S. Radl, C. Radeke, J. G. Khinast, and S. Sundaresan, "Parcel-Based Approach for the Simulation of Gas-Particle Flows," in *8th International Conference on CFD in Oil & Gas, Metallurgical and Process Industries*, Trondheim, Jun. 2011.

[86] J. H. Das and J. E. Morris, "Diffusion and self-gettering of ion-implanted copper in polyimide," *J Appl Phys*, vol. 66, no. 12, pp. 5816–5820, Dec. 1989, doi: 10.1063/1.343652.

[87] E. Ludwig *et al.*, "Corrosion of Copper in Combination with Polyimide," in *Conference Proceedings EUROCORR 2017*, Prague, Czech Republic, EU, Sep. 2017.

[88] M. Giacomelli Penon, S. J. Picken, M. Wübbenhorst, G. De Vos, and J. Van Turnhout, "Dielectric water sorption analysis," *Review of Scientific Instruments*, vol. 77, no. 11, 2006, doi: 10.1063/1.2370739.

[89] E. Stricker, Z. Adler, J. Wainright, and R. Savinell, "Diffusion Coefficients of Cuprous and Cupric Ions in Electrolytes with High Concentrations of Bromide Ions," *J Chem Eng Data*, vol. 64, no. 3, pp. 1095–1100, Mar. 2019, doi: 10.1021/acs.jced.8b00990.

[90] B. Y. Kazimierz Krynicki, C. D. Green, and D. W. Sawyer, "Pressure and Temperature Dependence of Self-diffusion in Water," *Faraday Discuss Chem Soc*, vol. 66, pp. 199–208, Sep. 1978, doi: 10.1039/DC9786600199.

[91] I. V. Volgin, S. V. Larin, A. V. Lyulin, and S. V. Lyulin, "Coarse-grained molecular-dynamics simulations of nanoparticle diffusion in polymer nanocomposites," *Polymer (Guildf)*, vol. 145, pp. 80–87, Jun. 2018, doi: 10.1016/j.polymer.2018.04.058.

7 Appendices

7.1 Appendix A – Atom and Ion diffusion

In this work, bulk diffusion for different species was determined and the results will be presented in this section. To provide better statistics the results were often averaged over all simulation runs and the results of single simulations are presented as visualization for the improvement of larger sample sizes. Table 4 summarizes the results of the bulk simulations for atoms and ions.

7.1.1 Motivation

Figure 29 shows an SEM image of a FIB cut of ion diffusion into the polyimide layer (dark part on the top of Figure 29). This ion diffusion can lead to defects of the protected device (light part on the bottom of Figure 29). In this case the polyimide acts as a protective layer to the metal surface below. Understanding the underlying mechanisms that influence the transport behavior of various ions through the polymer is the first step to improve the quality of the protective polyimide layer. MD simulations can aid in getting this understanding.

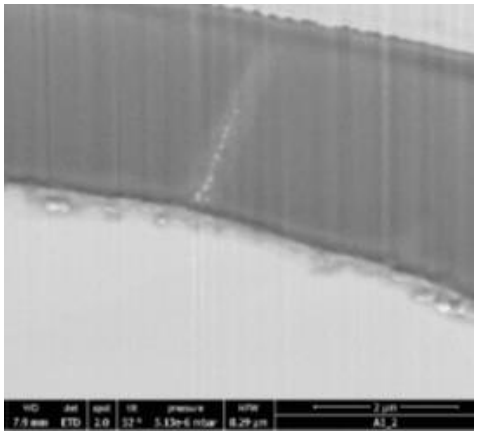

Figure 29: SEM image of a FIB cut of ion diffusion into PI on a Cu surface [87].

7.1.2 Atoms

The first simulation run was conducted with atoms to investigate the effect of atomic charge on the diffusion coefficient. The atoms were chosen as their respective ions were of interest in the present study. Although the uncharged atoms would not require counter ions for charge neutrality the system was prepared the same way as for the charged ions later for reasons of comparability.

7.1.2.1 Cu

Figure 30 shows the average MSD graph of uncharged Cu atoms over the course of 9 simulations each 5 ns long. The graph shows a reasonable linear fit over the range indicated by the black line.

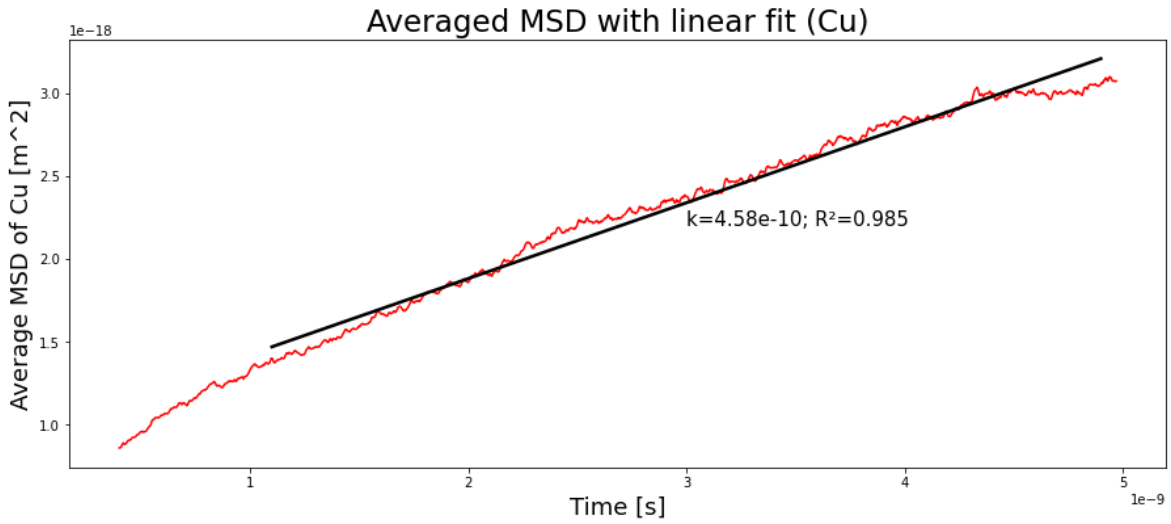

Figure 30: Average MSD of 9 simulation runs, each containing 93 uncharged Cu atoms in the Kapton matrix. The black line indicates the slope of the graph in the range of the line.

7.1.2.2 Cl

Similarly to the before-mentioned Cu atoms, the average MSD of uncharged Cl atoms can be estimated with a linear fit quite accurately and shows that the MSD is proportional to time. However, the slope of the linear fit is smaller in comparison to Cu before.

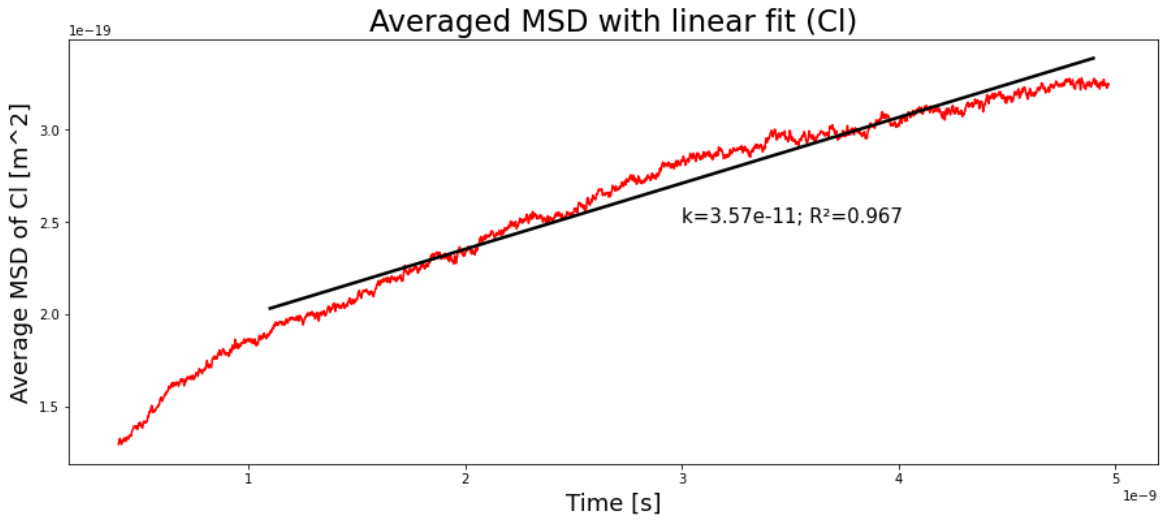

Figure 31: Average MSD of 9 simulations runs, each containing 186 uncharged Cl atoms in the Kapton matrix. The black line indicates the slope of the graph in the range of the line.

7.1.3 Ions

The species of interest will often be present as ions within the polymer matrix. Therefore, the second simulation series was conducted with ions and counterions to provide charge neutrality to the system. As main examples copper, double and single positively charged, as well as chloride single negatively charged, were chosen as for the investigation of atoms before.

7.1.3.1 Cu^{2+}

Figure 32 shows the average MSD of Cu^{2+} ions in the polymer matrix. In this case 9 simulations were averaged, but only 10 ions were inserted into the system, which is reflected by fluctuating data. The small sample size does not allow to draw any conclusions regarding the diffusion coefficient as there is no clear time dependence of the MSD shown.

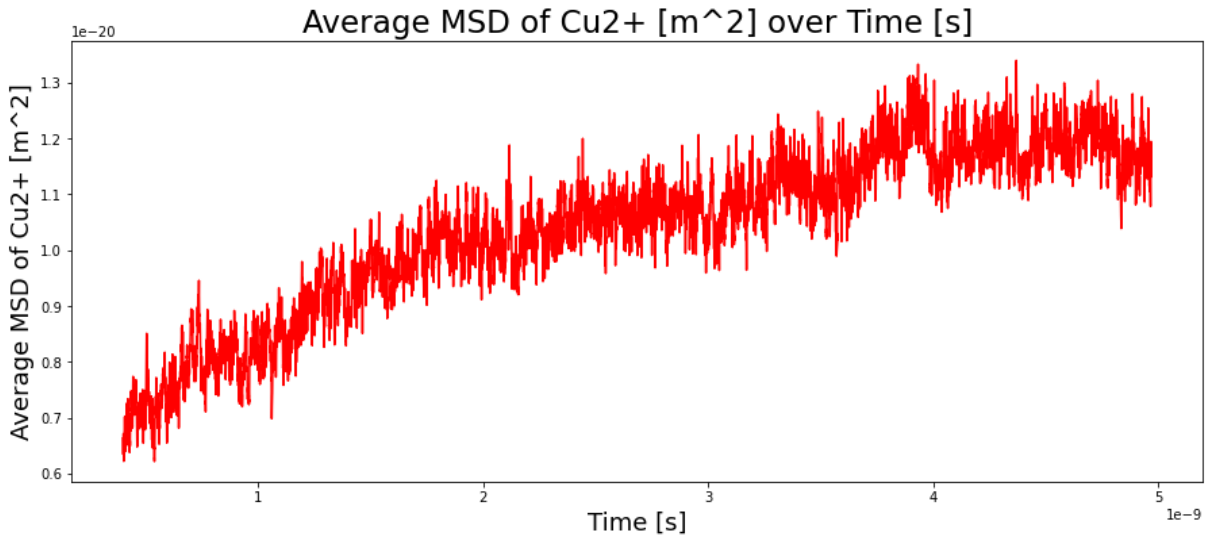

Figure 32: Average MSD of 9 simulations runs, each containing 10 Cu^{2+} ions in the Kapton matrix.

Figure 33 shows the average MSD of Cu^{2+} over 9 simulations, but in this case 93 Cu^{2+} ions were inserted into each respective simulation. After about 2.2 ns the MSD begins to linearly increase with time, which is highlighted by the black line obtained from a least squares method. R^2 is smaller than for the graphs for atoms but is still in good agreement with the simulation. However, the diffusion is around 3 orders of magnitude slower for Cu^{2+} in comparison to Cu as indicated in Table 4.

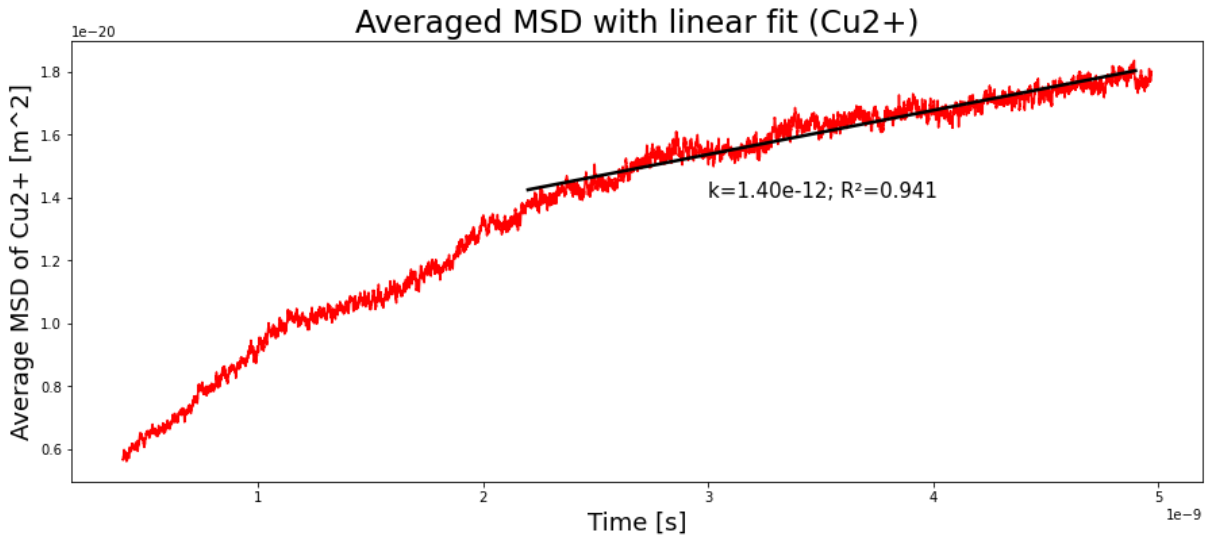

Figure 33: Average MSD of 9 simulations runs, each containing 93 Cu^{2+} ions in the Kapton matrix.

7.1.3.2 Cu^{+}

In the next step Cu^{+} ions were investigated as the assumption was that the charge is influencing the diffusion, depending on the electro positivity.

Figure 34 shows the MSD of a single simulation run with 80 Cu^{+} ions in the polymer matrix. Especially in the region between 2.5 and 4.5 ns it is important to note that due to only using 1 simulation run, although with many ions, the simulation does not describe the behavior properly. In this region it is assumed that a lot of the ions are trapped and only vibrate in their spatial location, which leads to this plateauing of the MSD. In this case the Einstein equation cannot be used to determine the diffusion coefficient.

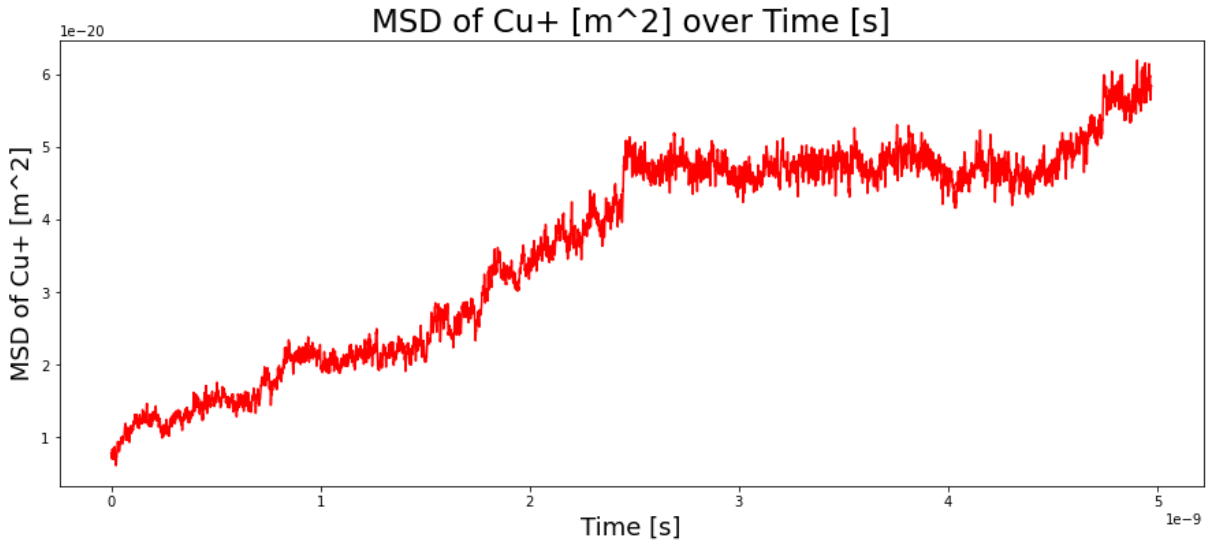

Figure 34: MSD of 1 simulation run, containing 80 Cu^{+} ions in the Kapton matrix.

Figure 35 shows the average MSD of 9 simulation runs, each containing 80 Cu^{+} ions. Although the fit is worse than for Cu^{2+}, after 2.2 ns a clear linear trend of increasing MSD with time is

visible. As assumed the diffusion takes place faster than for the double charged ions before. Table 4 shows that the diffusion of single charged ions is one order of magnitude faster.

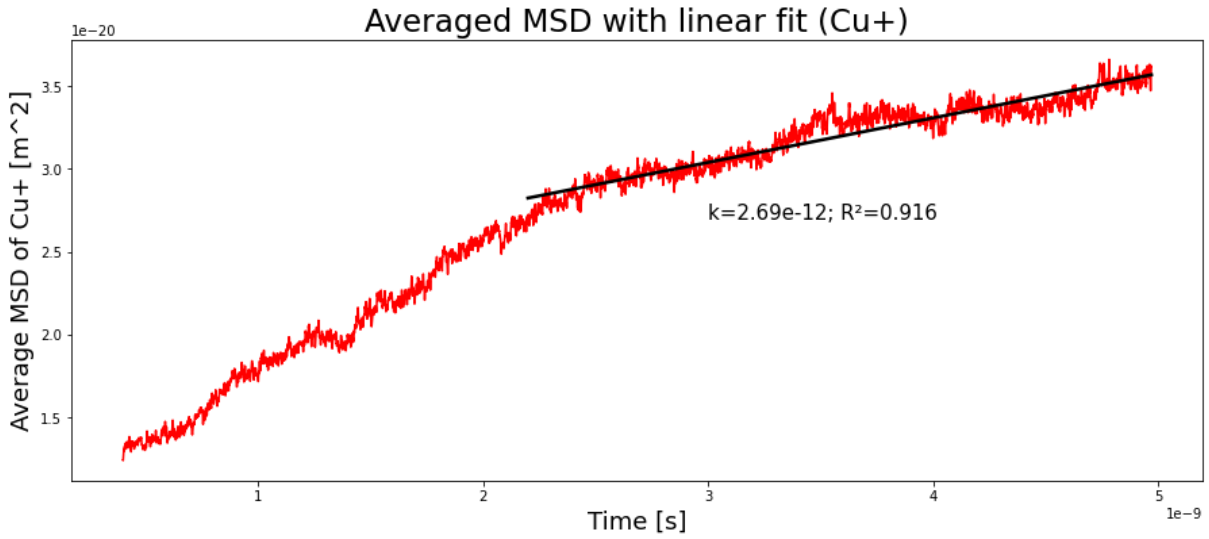

Figure 35: Average MSD of 9 simulations runs, each containing 80 Cu^+ ions in the Kapton matrix.

7.1.3.3 Cl^-

Cl^- was used as a counterion for the Cu ions as both Copper(II) chloride and Copper(I) chloride are salts often used in electro chemical experiments. In our simulations the charge of chloride did not change and only the number of chloride ions changed to provide the required charge neutrality. Similar to the graphs of Cu before, simulations with few ions do not allow to derive the diffusion coefficient from the MSD as there is no clear proportionality between MSD and time as shown in Figure 36.

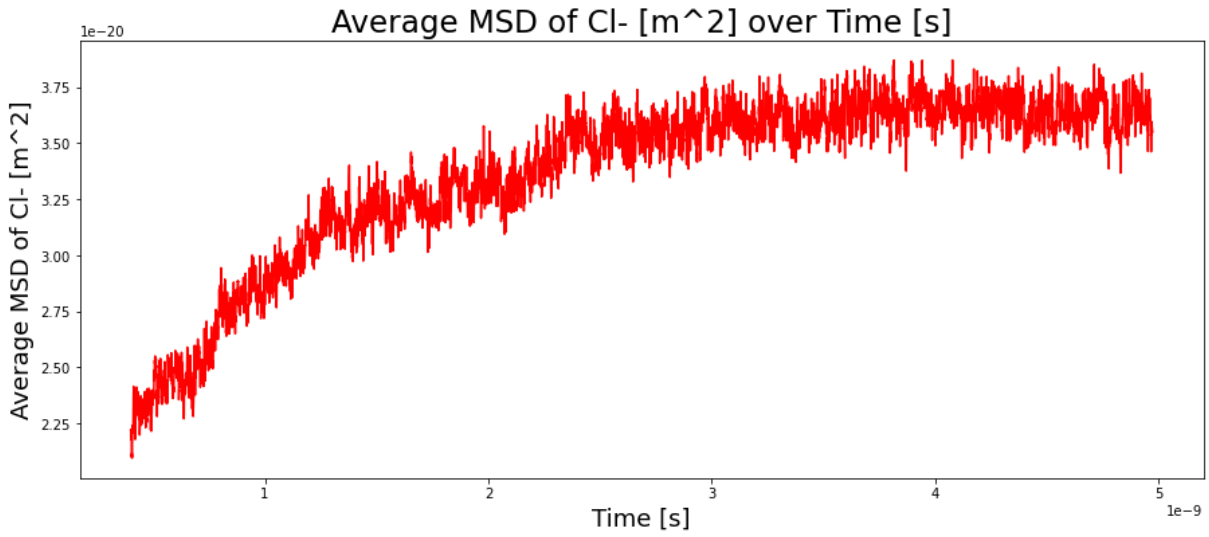

Figure 36: Average MSD of 9 simulations runs, each containing 20 Cl^- ions in the Kapton matrix. Cl^- as counterions for Cu^{2+}.

Interestingly, chloride diffusion was monitored for different ions, i.e. Cu^{2+} and Cu^{+}, but only the number of chloride counterions changed for the respective simulations. Therefore, it was possible to show that the diffusion is only dependent on the charge of the ions and not their counterparts, as the slope of the MSDs shown in Figure 37 and Figure 38 is in the same order of magnitude. The higher R^2 that can be seen in the graph of Figure 37 (Cl^- ions were the counterions for Cu^{2+}) supports the assumption that larger sample sizes provide better results.

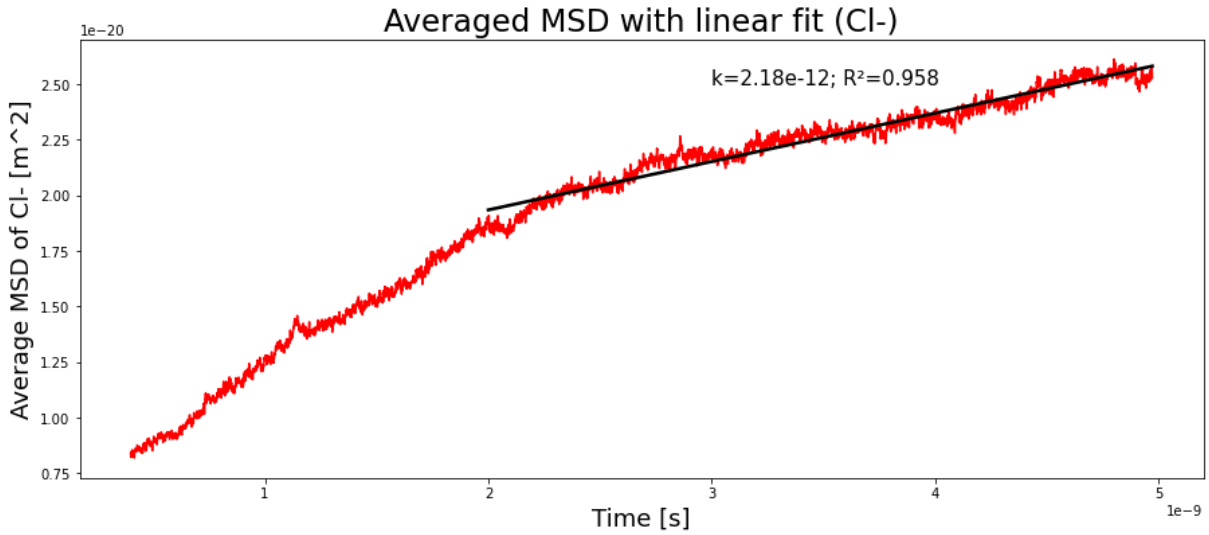

Figure 37: Average MSD of 9 simulations runs, each containing 186 Cl^- ions in the Kapton matrix. Cl^- as counterions for Cu^{2+}.

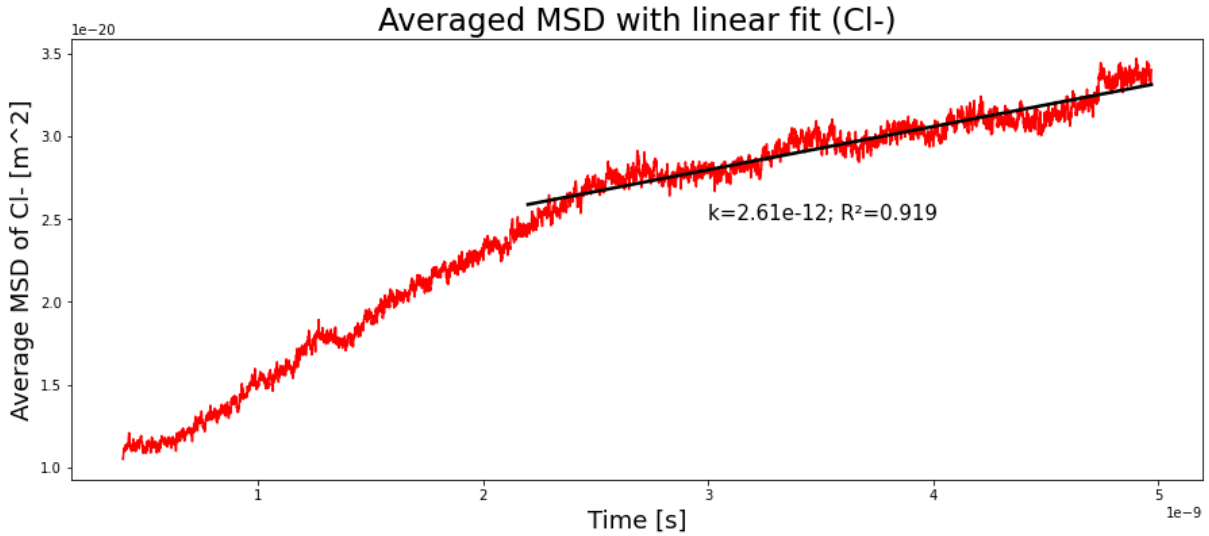

Figure 38: Average MSD of 9 simulation runs, each containing 80 Cl^- ions in the Kapton matrix. Cl^- as counterions for Cu^{+}.

Table 4 summarizes the results of the bulk diffusion simulations of Cu, Cl and their respective ions.

Table 4: Orders of diffusion coefficients for Cu and Cl atoms and their respective ions.

	Cu	*Cu^+*	*Cu^{2+}*	*Cl*	*Cl^-*
Diffusion coefficient	$D = O\left(10^{-10}\frac{m^2}{s}\right)$	$D = O\left(10^{-12}\frac{m^2}{s}\right)$	$D = O\left(10^{-13}\frac{m^2}{s}\right)$	$D = O\left(10^{-11}\frac{m^2}{s}\right)$	$D = O\left(10^{-12}\frac{m^2}{s}\right)$

7.1.4 Molecules

The procedure for diffusion simulations of molecules is in this framework the same as for atoms and ions.

7.1.4.1 Water

The first molecule of interest was water, as the ions investigated before are coming from aqueous solutions. Water was investigated at concentrations of 1 and 3 wt% to be below the stated water uptake of 4 wt% in Kapton® [88].

Figure 39 and Figure 40 show the MSD graph of water with concentrations of 1 wt% and 3 wt% respectively at 300 K. In this case 1 wt% is represented by 68 water molecules, which is already a usable sample size, based on the findings of the ion and atom simulations. The two figures show that the diffusion coefficient is independent of the concentration and that with a larger sample size (3 wt%) the linear fit is more accurate.

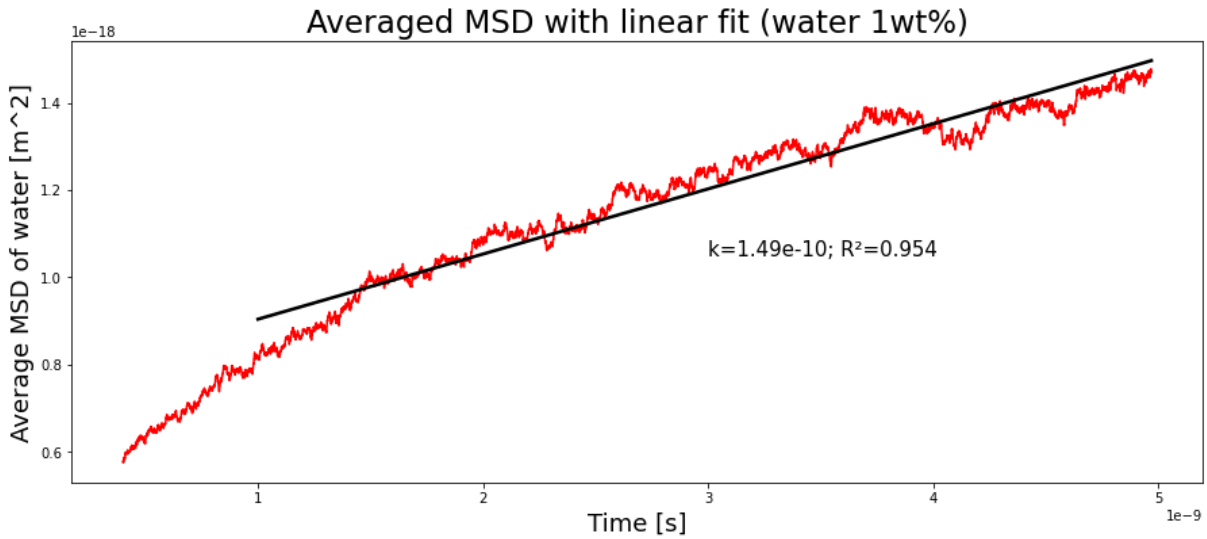

Figure 39: Average MSD of 9 simulation runs at 300 K with 1 wt% water in the polymer matrix.

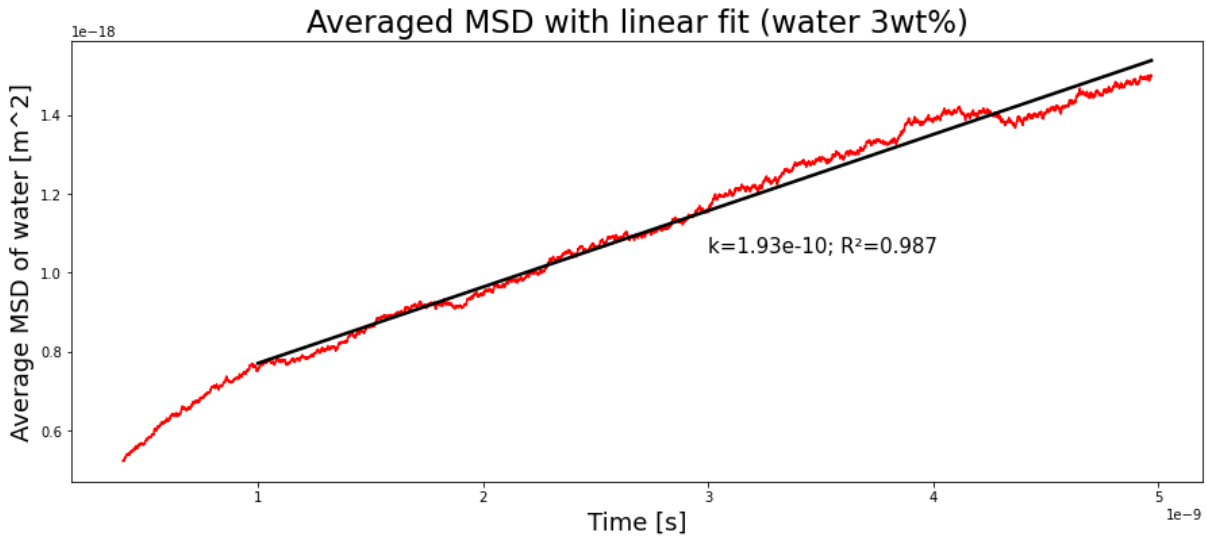

Figure 40: Average MSD of 9 simulation runs at 300 K with 3 wt% water in the polymer matrix.

Figure 41 and Figure 42 show the MSDs of water at a temperature of 400 K. The graphs show the same behavior regarding the quality of the fit for the respective concentrations. Furthermore, the slopes of the linear fits are of the same order of magnitude, and as expected for higher temperatures steeper than the slopes of the simulations at 300 K. The steeper slope can be interpreted as a faster diffusion process as the slope is proportional to the diffusion coefficient.

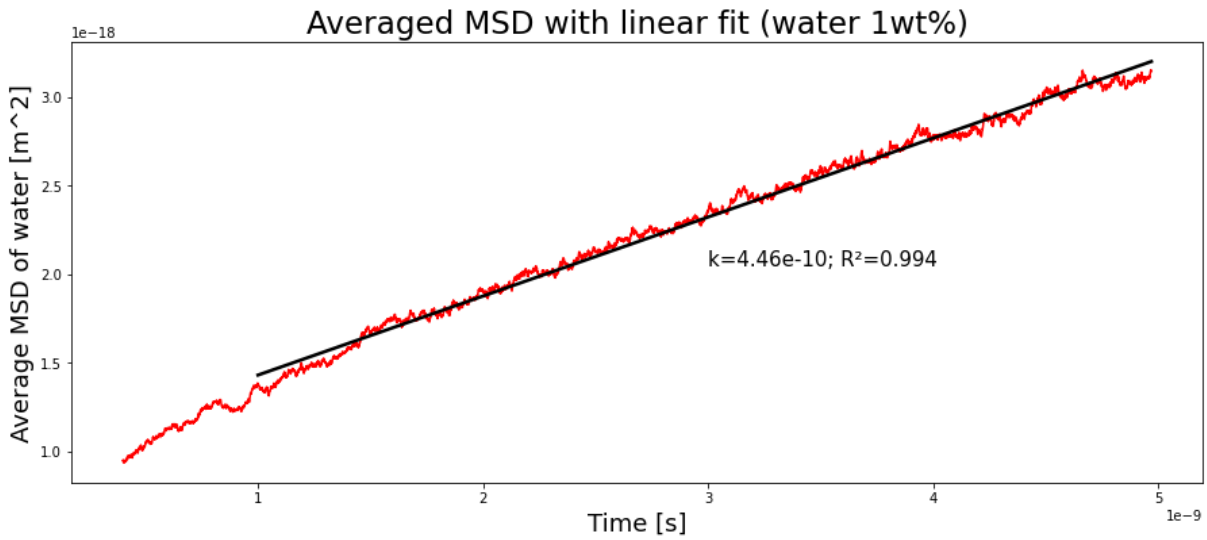

Figure 41: Average MSD of 9 simulation runs at 400 K with 1 wt% water in the polymer matrix.

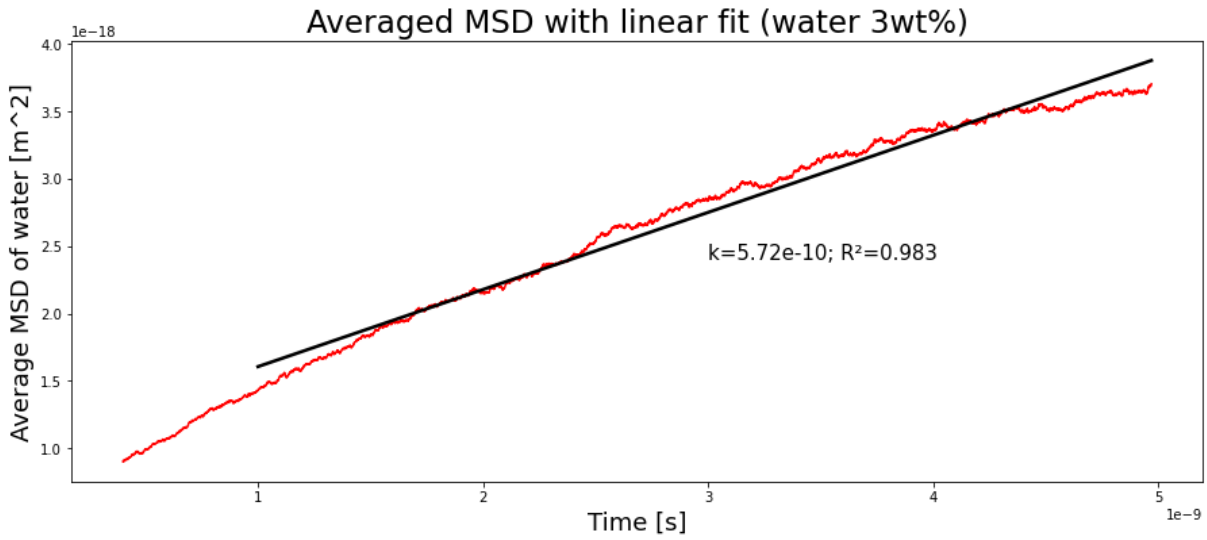

Figure 42: Average MSD of 9 simulation runs at 400 K with 3 wt% water in the polymer matrix.

7.1.5 Limitations

Including the new findings from the isopropanol investigations described in chapter 2, the double logarithmic plots were investigated for the ions of copper as well. Figure 43 and Figure 44 show the graphs of the average MSD of 3 simulations over time on a normal scale and double logarithmic scale respectively. While Figure 43 shows a decent linearity as the R^2 value highlights, the slope, i.e. n, in Figure 44 shows that sub-diffusion is present in the simulated system. The results presented in Table 4 support that assumption, as the diffusion coefficient, determined from experiments by Das et al. [86], is in the order of $10^{-22}\,\frac{m^2}{s}$. The data in Table 4 shows a large deviation from the literature data.

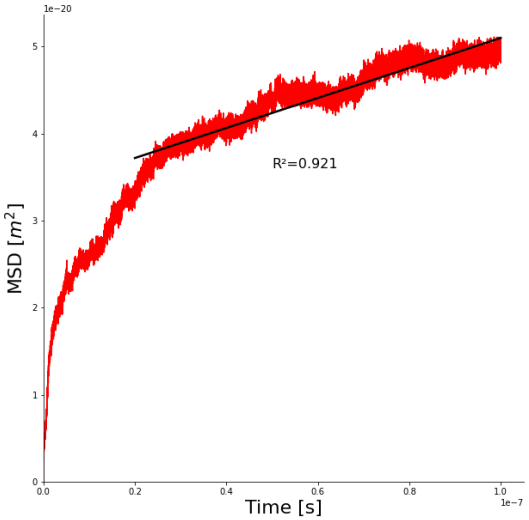

Figure 43: Graph of average AA MSD (self-diffusion) of 3 simulations with 93 Cu^{2+} ions. Simulation at 300 K and 1 atm for 100 ns.

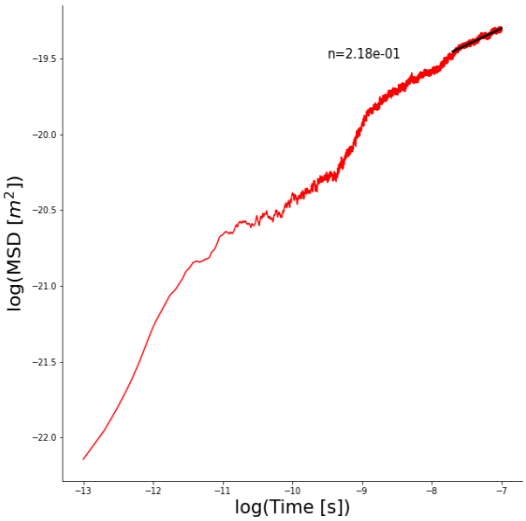

Figure 44: Double logarithmic graph of average AA MSD (self-diffusion) of 3 simulations with 93 Cu^{2+} ions. Simulation at 300 K and 1 atm for 100 ns.

The calculated minimal simulation time based on the equation presented by Müller-Plathe [57] and described in chapter two for diffusion of copper in a polyimide would be $2.5 \cdot 10^3\ s$.

7.1.6 Conclusion – ion diffusion

The SEM images taken by Ludwig [87] showed that ion diffusion in protective polyimide layers can lead to defects of the protected devices. The present work aimed to investigate the transport properties of ions, and especially determine the diffusion coefficient of these ions in the polyimide bulk with molecular dynamics simulations.

Equilibrated systems with varying amounts of ions were prepared and the mean-squared-displacement (MSD) was monitored to allow the calculation of the diffusion coefficient. The first finding as shown in Figure 32 and Figure 34, was the importance of the sample size of ions for the MSD. If too few ions are sampled for the MSD, effects like the trapping of ions in the bulk, highlighted by the plateau in the MSD graph of Figure 34, affect the results from the simulation largely. Comparing Figure 32 and Figure 33 shows that more sampled ions, as in Figure 33, smooth the MSD graph and improve the identification of the linear region of the MSD. However, to prevent unrealistic concentrations of ions in the polyimide bulk by increasing the number of ions, it is necessary to prepare larger systems.

The simulation of polyimide systems with ions and molecules showed that the prediction of trends is possible despite the short simulations. Stricker et al. [89] showed that the diffusion coefficient of cuprous ion (Cu^+) is higher than the diffusion coefficient of cupric ion (Cu^{2+}). Table 4 in the present work shows the same trend. Furthermore, the temperature dependency of water diffusion, described by Kazimierz et al. [90], was shown in Figure 40 and Figure 42.

The slope of the MSD graph, that represents the diffusion coefficient, in the simulations at 400 K is steeper than the slope in the simulations at 300 K.

However, the additional investigation of the slope of the MSD over time in a double logarithmic graph (see: Figure 44) showed that the simulations were still in a sub-diffusive regime. Therefore, it would be important to apply the findings for coarse-grained simulations described in chapter 2 of the present work to facilitate longer simulations. Furthermore, extending the simulations to other ions of interest is an interesting point of future research.

7.2 Appendix B – The VOTCA / LAMMPS Interface

A major part of this thesis was the provision of a working interface between the software tools VOTCA and LAMMPS. The software tool VOTCA has a good working interface with GROMACS, a different MD simulation software tool, including tutorials that allow the user to understand the required input files and the format of them to conduct correct simulations. However, it is different for LAMMPS as only 1 tutorial is provided that describes the CG simulations of SPC/E water, but not the process of getting there from an AA simulation. This appendix should allow researchers to obtain CG force fields and conduct CG MD simulations with the combination of VOTCA and LAMMPS, by following the steps described below.

7.2.1 VOTCA commands

7.2.1.1 Command for mapping the CG geometry

The all-atom (AA) representation of system.data is mapped to the coarse-grained (CG) representation cg1.dump based on the geometry given in hexane.xml. The topo.xml describes the bonds, angles and dihedrals of the AA representation.

csg_map --top topo.xml --cg hexane.xml --trj system.data --out cg1.dump

7.2.1.2 Command for getting the RDFs

The RDFs are used in the IBI to create the CG-beads based on the AA RDFs. The LAMMPS trajectory is also dumped as an xtc file. The settings.xml file describes how the CG process should be done.

csg_stat --top topo.xml --trj lammps.xtc --cg hexane.xml --nt 24 --options settings.xml --begin 0

7.2.1.3 Further helpful commands from GROMACS

gmx dump -f gromacs.xtc > GROMACS_xtc_readable

gmx dump -s topol.tpr > read_topol

After installing GROMACS the gmx dump command can be used. With this command it is possible to make binary files readable.

7.2.2 VOTCA input files for LAMMPS

To prepare the RDFs of an AA simulation from LAMMPS with VOTCA, the following files need to be prepared:

- Trajectory file of all atom simulation (we export it to xtc as this works better)
- Topology file of the CG representation (in our case: hexane.xml)

- Topology file of the AA representation including all bonds, angles and dihedrals (here: topo.xml)
- Settings file that tells VOTCA what the range in which the interactions will be and how small the bins should be for the RDF (settings.xml)

7.2.3 Step-by-step description from LAMMPS AA to VOTCA RDFs

- Already prepare your LAMMPS system.data in the way that the atoms that are in 1 CG bead later are in chronological order
- Conduct the all-atom simulation in LAMMPS (incl. the .xtc file)
- Prepare the above-mentioned files
- Use the csg_stat command mentioned above to get the RDFs

7.2.4 Preparation of input files for the iterative Boltzmann inversion (IBI)

Before preparing the input files it is important to understand how the LAMMPS notation translates to the VOTCA notation. This is since molecule and atom naming work differently in LAMMPS and VOTCA.

The following command allows to get this information:

- csg_dump --top system.data > log.data

The result looks like this:

```
List of molecules:
molecule: 1 C6H14 beads: 20
0 Name C80 Type C80 Mass 12.011 Resnr 0 Resname DUM Charge 0
1 Name H85 Type H85 Mass 1.008 Resnr 0 Resname DUM Charge 0
2 Name H85 Type H85 Mass 1.008 Resnr 0 Resname DUM Charge 0
3 Name H85 Type H85 Mass 1.008 Resnr 0 Resname DUM Charge 0
4 Name C81 Type C81 Mass 12.011 Resnr 0 Resname DUM Charge 0
5 Name H85 Type H85 Mass 1.008 Resnr 0 Resname DUM Charge 0
6 Name H85 Type H85 Mass 1.008 Resnr 0 Resname DUM Charge 0
7 Name C81 Type C81 Mass 12.011 Resnr 0 Resname DUM Charge 0
8 Name H85 Type H85 Mass 1.008 Resnr 0 Resname DUM Charge 0
9 Name H85 Type H85 Mass 1.008 Resnr 0 Resname DUM Charge 0
10 Name C81 Type C81 Mass 12.011 Resnr 0 Resname DUM Charge 0
11 Name H85 Type H85 Mass 1.008 Resnr 0 Resname DUM Charge 0
12 Name H85 Type H85 Mass 1.008 Resnr 0 Resname DUM Charge 0
13 Name C81 Type C81 Mass 12.011 Resnr 0 Resname DUM Charge 0
14 Name H85 Type H85 Mass 1.008 Resnr 0 Resname DUM Charge 0
15 Name H85 Type H85 Mass 1.008 Resnr 0 Resname DUM Charge 0
16 Name C80 Type C80 Mass 12.011 Resnr 0 Resname DUM Charge 0
17 Name H85 Type H85 Mass 1.008 Resnr 0 Resname DUM Charge 0
18 Name H85 Type H85 Mass 1.008 Resnr 0 Resname DUM Charge 0
19 Name H85 Type H85 Mass 1.008 Resnr 0 Resname DUM Charge 0
```

This is the log.data file for a hexane molecule. It is important that the molecule is named based on what VOTCA detects as atoms in the molecule (in this specific case C6H14). Further,

VOTCA is starting the numbering of atoms with 0, and is adding the letter of the atom to the atom type that it was given in LAMMPS (e.g., 80 → C80)

With this information we can prepare the required files based on the following example.

7.2.4.1 Topology file topo.xml

The first file is the topology file here always referred to as topo.xml that describes the AA topology of the molecule. Including the atoms that build the molecule, the bonds, angles and dihedral interactions within the molecule.

```
<topology>
<molecules>
<clear  />
<molecule name='C6H14' nmols='1000' nbeads='20'>
<bead name ='0' type='C80' mass='12.011' q='0.0' />
<bead name ='1' type='H85' mass='1.008' q='0.0' />
<bead name ='2' type='H85' mass='1.008' q='0.0' />
<bead name ='3' type='H85' mass='1.008' q='0.0' />
<bead name ='4' type='C81' mass='12.011' q='0.0' />
<bead name ='5' type='H85' mass='1.008' q='0.0' />
<bead name ='6' type='H85' mass='1.008' q='0.0' />
<bead name ='7' type='C81' mass='12.011' q='0.0' />
<bead name ='8' type='H85' mass='1.008' q='0.0' />
<bead name ='9' type='H85' mass='1.008' q='0.0' />
<bead name ='10' type='C81' mass='12.011' q='0.0' />
<bead name ='11' type='H85' mass='1.008' q='0.0' />
<bead name ='12' type='H85' mass='1.008' q='0.0' />
<bead name ='13' type='C81' mass='12.011' q='0.0' />
<bead name ='14' type='H85' mass='1.008' q='0.0' />
<bead name ='15' type='H85' mass='1.008' q='0.0' />
<bead name ='16' type='C80' mass='12.011' q='0.0' />
```

The first line describes the molecule for VOTCA. The name that was found from the csg_dump command should be used for the molecule (here: C6H14). How many molecules there are in the AA simulation (here: 1000) and how many beads (in this case atoms) make up each molecule (here: 20). Each atom needs to be named the same way as found from the csg_dump command.

Then bonds, angles and dihedrals need to be defined as the atom interaction in the AA simulation.

```
<bonded>
<bond>
<name>bond</name>
<beads>
C6H14:0   C6H14:1
C6H14:0   C6H14:2
C6H14:0   C6H14:3
C6H14:0   C6H14:4
C6H14:4   C6H14:5
C6H14:4   C6H14:6
C6H14:4   C6H14:7
C6H14:7   C6H14:8
C6H14:7   C6H14:9
C6H14:7   C6H14:10
C6H14:10   C6H14:11
C6H14:10   C6H14:12
C6H14:10   C6H14:13
C6H14:13   C6H14:14
C6H14:13   C6H14:15
C6H14:13   C6H14:16
```

```
<angle>
<name>angle</name>
<beads>
C6H14:1   C6H14:0   C6H14:2
C6H14:1   C6H14:0   C6H14:3
C6H14:1   C6H14:0   C6H14:4
C6H14:2   C6H14:0   C6H14:3
C6H14:2   C6H14:0   C6H14:4
C6H14:3   C6H14:0   C6H14:4
C6H14:0   C6H14:4   C6H14:5
C6H14:0   C6H14:4   C6H14:6
C6H14:0   C6H14:4   C6H14:7
C6H14:5   C6H14:4   C6H14:6
C6H14:5   C6H14:4   C6H14:7
C6H14:6   C6H14:4   C6H14:7
C6H14:4   C6H14:7   C6H14:8
C6H14:4   C6H14:7   C6H14:9
C6H14:4   C6H14:7   C6H14:10
C6H14:8   C6H14:7   C6H14:9
C6H14:8   C6H14:7   C6H14:10
```

```
<dihedral>
<name>dihedral</name>
<beads>
C6H14:1   C6H14:0   C6H14:4   C6H14:5
C6H14:2   C6H14:0   C6H14:4   C6H14:5
C6H14:3   C6H14:0   C6H14:4   C6H14:5
C6H14:1   C6H14:0   C6H14:4   C6H14:6
C6H14:2   C6H14:0   C6H14:4   C6H14:6
C6H14:3   C6H14:0   C6H14:4   C6H14:6
C6H14:1   C6H14:0   C6H14:4   C6H14:7
C6H14:2   C6H14:0   C6H14:4   C6H14:7
C6H14:3   C6H14:0   C6H14:4   C6H14:7
C6H14:0   C6H14:4   C6H14:7   C6H14:8
C6H14:0   C6H14:4   C6H14:7   C6H14:10
C6H14:0   C6H14:4   C6H14:7   C6H14:9
C6H14:5   C6H14:4   C6H14:7   C6H14:8
C6H14:6   C6H14:4   C6H14:7   C6H14:8
C6H14:5   C6H14:4   C6H14:7   C6H14:9
```

7.2.4.2 Coarse-graining file hexane.xml

The coarse-graining file describes how the atoms from the AA topology will be combined to create the CG representation of the beads.

```
<cg_molecule>
  <name>HEX</name>
  <ident>C6H14</ident>
  <topology>
    <cg_beads>
      <cg_bead>
        <name>A1</name>
        <type>A</type>
        <mapping>A</mapping>
        <beads>1:C6H14:0 1:C6H14:1 1:C6H14:2 1:C6H14:3 1:C6H14:4 1:C6H14:5 1:C6H14:6</beads>
      </cg_bead>
      <cg_bead>
        <name>B</name>
        <type>B</type>
        <mapping>B</mapping>
        <beads>1:C6H14:7 1:C6H14:8 1:C6H14:9 1:C6H14:10 1:C6H14:11 1:C6H14:12</beads>
      </cg_bead>
      <cg_bead>
        <name>A2</name>
        <type>A</type>
        <mapping>A</mapping>
        <beads>1:C6H14:16 1:C6H14:17 1:C6H14:18 1:C6H14:19 1:C6H14:13 1:C6H14:14 1:C6H14:15 </beads>
      </cg_bead>
  </cg_beads>
  <cg_bonded>
    <bond>
      <name>bond</name>
      <beads>
        A1 B
        A2 B
      </beads>
    </bond>
    <angle>
      <name>angle</name>
      <beads>
        A1 B A2
      </beads>
    </angle>
  </cg_bonded>
  </topology>
```

The name of the molecule is how the user wants to define it and is of no interest for the mapping. The ident is important and needs to be the same as the molecules are named from the csg_dump command and are named in the topology file to allow VOTCA to make the connection.

In the topology section the CG beads are described. Each bead has a name, is of a certain type and has a mapping. The mapping will be explained later.

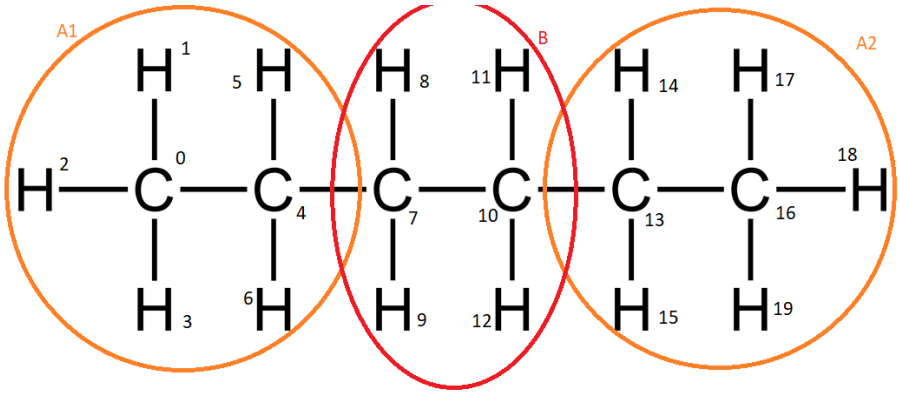

This figure shows how the CG beads are defined in this case.

In the cg_bonded section the bonds, angles and if there are the dihedral interactions of the CG beads need to be defined. In this case there are only bonds between A1 and B as well as between B and A2, and there is one angle A1 B A2 with B marking the middle bead.

Lastly, the user must tell VOTCA the atomic masses of all atoms that build up the beads. The mapping in this section is connected to the mapping that was defined in the topology section. Both beads A1 and A2 were defined to have the same mapping A. For the case of A1 the mapping tells VOTCA that atom 1:C6H14:0 has a molecular weight of 12.011, atom 1:C6H14:1 has 1.008 and so on. Importantly, one must use the right order for the different beads. That's why bead A2 is not in chronological order but must replicate the same atom order as defined in mapping A for bead A1. If the ordering for A2 is not adapted, the center of mass calculation would be flawed. In this case if only the chronological order would have been followed the 4th atom in A2 (C16) would have had a weight of 1.008.

```
  <maps>
    <map>
      <name>A</name>
      <weights> 12.011 1.008 1.008 1.008 12.011 1.008 1.008</weights>
    </map>
    <map>
      <name>B</name>
      <weights> 12.011 1.008 1.008 12.011 1.008 1.008 </weights>
    </map>
  </maps>
</cg_molecule>
```

7.2.4.3 Settings file settings.xml

The settings file in the case for mapping defines what are the minimum and maximum values for each interaction (e.g., an angle between 0 and π, and a bond length between 0.05 and 1 Å) and the step size for each of these interactions.

The first part was adopted directly from VOTCA tutorials.

```
<cg>
  <nbsearch>grid</nbsearch>
  <!--fmatch section -->
  <fmatch>
    <!--Number of different CG beads in the system. SHOULD BE KICKED OUT!!! -->
    <constrainedLS>true</constrainedLS>
    <!--Number of frames for block averaging -->
    <frames_per_block>10</frames_per_block>
  </fmatch>
```

The second part includes the mentioned CG bonded and non-bonded interactions.

```
  <bonded>
    <!-- name of the interaction -->
    <name>bond</name>
    <!-- fmatch specific stuff -->
    <min>0.0</min>
    <max>1.0</max>
    <step>0.001</step>
  </bonded>
  <bonded>
    <!-- name of the interaction -->
    <name>angle</name>
    <!-- fmatch specific stuff -->
    <min>0.0</min>
    <max>3.1415</max>
    <step>0.01</step>
  </bonded>
```

Importantly, the name that is defined for each interaction needs to match the name given to the interaction in the coarse-graining file (hexane.xml). For the bonded interactions this would be bond and angle.

The same holds true for the non-bonded interactions.

```
  <!-- example for a non-bonded interaction entry -->
  <non-bonded>
    <name>A-A</name>
    <type1>A</type1>
    <type2>A</type2>
    <min>0</min>
    <max>1.2</max>
    <step>0.01</step>
  </non-bonded>

  <non-bonded>
    <name>B-B</name>
    <type1>B</type1>
    <type2>B</type2>
    <min>0</min>
    <max>1.2</max>
    <step>0.01</step>
  </non-bonded>

  <non-bonded>
    <name>A-B</name>
    <type1>A</type1>
    <type2>B</type2>
    <min>0</min>
    <max>1.2</max>
    <step>0.01</step>
  </non-bonded>
</cg>
```

7.2.4.4 The trajectory file from LAMMPS (lammps.xtc)

The VOTCA tool was developed for the GROMACS simulation tool, therefore the connectivity between these tools is working stable. Due to this, the user is advised to export the trajectory from the LAMMPS simulations in the compressed ".xtc" format that GROMACS is also using. The following LAMMPS command exports the trajectory to the .xtc file:

dump 1 all xtc 5000 lammps.xtc

7.2.5 Differences between GROMACS and LAMMPS as the MD Simulator

There was no tutorial or thorough documentation of the mapping procedure for LAMMPS. Therefore, the tutorial for GROMACS "hexane" was replicated. The idea was to compare the results and assess if the LAMMPS case was built correctly. The system was made of 1000 hexane molecules and the AA simulations for LAMMPS and GROMACS were run for 5 ns respectively.

Although the qualitative behavior for 2 atom (bead) interactions were similar, especially the three atom interaction of the angle showed a very different behavior.

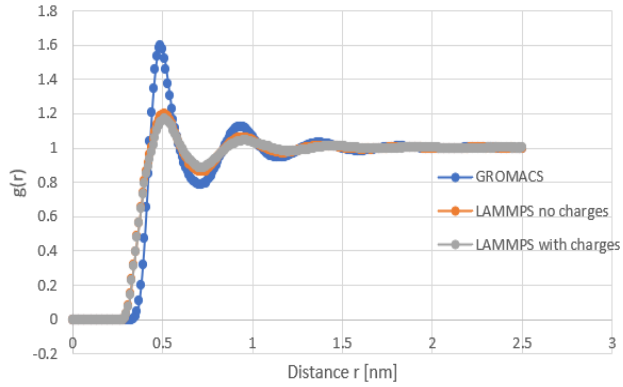

Figure 45: Comparison of RDF of non-bonded interaction A-A, in GROMACS and LAMMPS before adaptation of files.

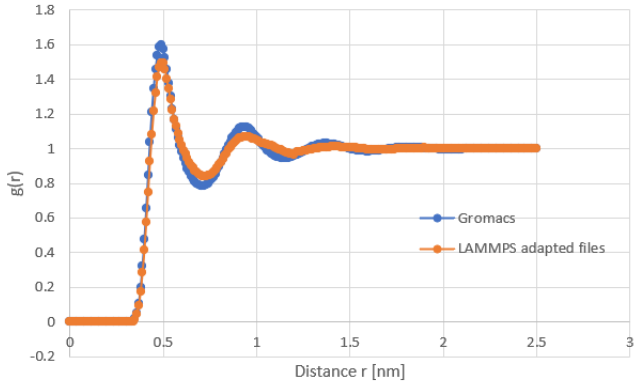

Figure 46: Comparison of RDF of non-bonded interaction A-A, in GROMACS and LAMMPS after adaptation of files.

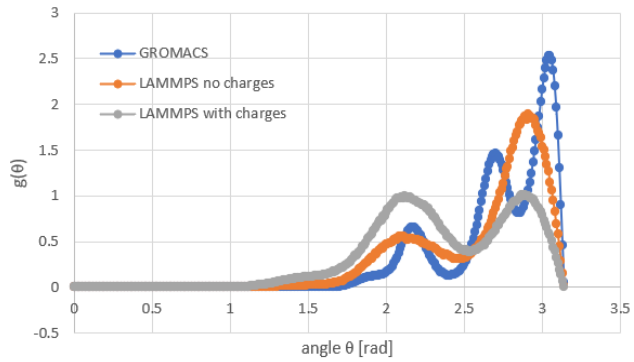

Figure 47: Comparison of RDF of bonded interaction A1-B-A2, in GROMACS and LAMMPS before adaptation of files.

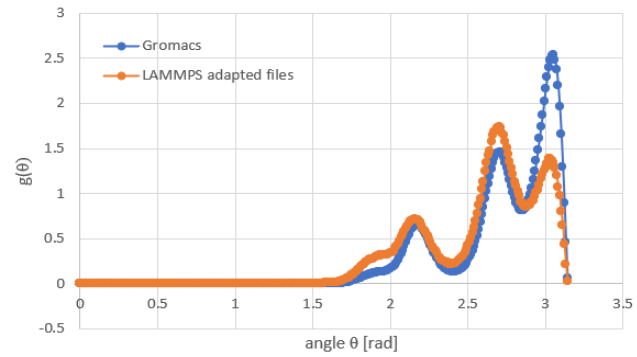

Figure 48: Comparison of RDF of bonded interaction A1-B-A2, in GROMACS and LAMMPS after adaptation of files.

The investigation of this difference in behavior between the LAMMPS and GROMACS simulation results began by reducing the complexity of the system. The interaction forces were set to zero, i.e., no movement of the atoms in the AA simulation. The interaction forces were set to zero by setting the force field parameters to zero (LAMMPS: settings.in file and GROMACS in the installation directory) Step-by-step interactions were added, i.e., first bond interactions, secondly angle interactions then dihedral and non-bonded interactions. The simulations were conducted for 1 timestep and results (atom coordinates and forces on atoms) were compared. For bonds and angles the results were identical as it was possible to use the same force fields in LAMMPS and GROMACS. After adding dihedral and non-bonded interactions, the results became different as it was not possible to replicate the used force field

equations in the two simulation tools. This in contrast to the fact that the force field parameters for dihedrals were the same for both LAMMPS and GROMACS.

7.2.6 Iterative Boltzmann Inversion

The steps described before were the prerequisite for the coarse-graining procedure. The actual coarse-graining procedure that is described here is called the "Iterative Boltzmann Inversion" (IBI), where in an iterative process the CG representation of the system is fitted to the AA behavior, which is represented by the RDFs. VOTCA already provides this feature, but again the correct input files need to be provided.

The following files need to be prepared in advance to conduct the IBI:

- settings.xml
- interaction.dist.tgt
- topo.xml
- cg_system.data
- system.in

7.2.6.1 Settings file settings.xml

As in the mapping procedure, the settings.xml file is the file that contains all the information for VOTCA to conduct the simulation. The file is structured as follows:

```
<cg>
  <bonded>
    <!-- name of the interaction -->
     <name>bond</name>
    <min>0.22</min>
    <max>0.35</max>
    <step>0.002</step>
    <inverse>
      <!-- target distribution -->
      <target>bond.dist.tgt</target>
      <lammps>
        <!-- name of the table for lammps run -->
        <table>bond.pot</table>
        <!-- nm to angstrom -->
        <scale>10</scale>
        <!-- kJ/mol to kcal/mol -->
        <y_scale>0.239006</y_scale>
    <table_begin>0.10</table_begin>
        <table_bins>0.002</table_bins>
      </lammps>
    </inverse>
  </bonded>
  <bonded>
    <!-- name of the interaction -->
    <name>angle</name>
    <min>1.7</min>
    <max>3.1</max>
    <step>0.02</step>
    <inverse>
      <!-- target distribution -->
      <target>angle.dist.tgt</target>
      <lammps>
        <!-- name of the table for lammps run -->
        <table>angle.pot</table>
        <!-- kJ/mol to kcal/mol -->
        <y_scale>0.239006</y_scale>
       </lammps>

    </inverse>
  </bonded>
```

In the file all parameters for each interaction need to be added. Again, the name of the interaction needs to match the name that was defined in the prior steps both in the hexane.xml

and the settings.xml file (here: "bond" and "angle"). The next lines define the range in which the values of the target distribution RDF (bond.dist.tgt) are interesting for the interaction. The target tag defines the file the contains the target RDF for each interaction (here: "bond.dist.tgt"). The table tag defines the name of the file where the final potential table should be saved after the IBI is finished. To account for the different units of VOTCA and LAMMPS the scale tag needs to be used. The scale tag is used for the x-axis of the RDF (here: the distance between to beads r in nm) and the y-scale accounts for the energy conversion. The same tags need to be addressed for the non-bonded interactions:

```
<non-bonded>
  <!-- name of the interaction -->
  <name>A-A</name>
  <!-- types involved in this interaction -->
  <type1>Bead1</type1>
  <type2>Bead1</type2>
  <!-- dimension + grid spacing of tables for calculations -->
  <min>0.1</min>
  <max>1.5</max>
  <step>0.01</step>
  <inverse>
    <!-- target distribution (rdf), just give gromas rdf.xvg -->
    <target>A-A.dist.tgt</target>
    <!-- update cycles -->
    <do_potential>1 0 0</do_potential>
    <!-- additional post processing of dU before added to potential -->
    <post_update></post_update>
    <!-- additional post processing of U after dU added to potential -->
    <post_add>convergence</post_add>
    <!-- name of the table for gromacs run -->
    <lammps>
      <!-- name of the table for lammps run -->
      <table>A-A.pot</table>
      <!-- nm to angstrom -->
      <scale>10</scale>
      <!-- kJ/mol to kcal/mol -->
      <y_scale>0.239006</y_scale>
     </lammps>
  </inverse>
</non-bonded>
```

Additionally, the beads as they are defined in the topo.xml file need to be mentioned for each interaction. If all interactions are defined the last part describes the general options for the IBI.

```
<!-- general options for inverse script -->
 <inverse>
   <!-- votca units 300*0.00831451 kJ/mol -->
   <kBT>2.49435</kBT>
   <!-- use lammps as simulation program -->
   <program>lammps</program>
   <!-- lammps specific options -->
   <lammps>
   <command>mpirun -oversubscribe -np 24 /home/user/lammps/src/lmp_mpi</command>
     <!-- lammps script to run !-->
     <script>system.in</script>
     <!-- topology to be used by  csg_stat !-->
     <topol>topo.xml</topol>
     <!-- traj file created by lammps !-->
     <traj>gromacs.xtc</traj>
   </lammps>
   <map>hexane_cg.xml</map>
   <initial_configuration>maindir</initial_configuration>
   <!-- these files are copied for each new run -->
   <filelist>cg_systemData_charges.data system.in topo.xml</filelist>
   <!-- do so many iterations -->
   <iterations_max>100</iterations_max>
   <!-- ibi: inverse biltzmann imc: inverse monte carlo -->
   <method>ibi</method>
 </inverse>
</cg>
```

7.2.6.2 VOTCA additional information - <min> and <max> tags

The VOTCA documentation says: "Similarly to the case of spline fitting (see Programs on csg_resample), the parameters min and max have to be chosen in such a way as to avoid empty bins within the grid." (https://www.votca.org/csg/methods.html)

7.2.6.3 VOTCA additional information - <traj> and </traj> tags

The <traj> tag needs to include the name of a trajectory file that is created during the simulation run.

```
<topol>topo.xml</topol>
<!-- traj file created by lammps !-->
<traj>kapton.xtc</traj>
```

Here the trajectory file is called "kapton.xtc" and needs to be called the same way in the system.in file for dumping of each iteration step.

```
dump 3 all xtc 10000 kapton.xtc
```

Without this, VOTCA is not able to iterate further than 1 step as it cannot find the trajectory file anymore from the previous iteration step.

7.2.6.4 Target interaction distribution *.dist.tgt

```
0.3 0 i
0.31 0 i
0.32 3.647500383e-05 i
0.33 0.0005659179596 i
0.34 0.003804542325 i
0.35 0.01490224789 i
0.36 0.04253148146 i
0.37 0.09526731003 i
0.38 0.1757437592 i
0.39 0.2832972088 i
0.4 0.4132943267 i
0.41 0.5745945803 i
0.42 0.7502997339 i
0.43 0.9241883981 i
0.44 1.079937845 i
0.45 1.216145793 i
0.46 1.321140679 i
0.47 1.414761144 i
0.48 1.469267418 i
0.49 1.497135039 i
0.5 1.496889352 i
0.51 1.459290243 i
0.52 1.40332521 i
0.53 1.344125584 i
0.54 1.282217019 i
0.55 1.222578484 i
0.56 1.168148473 i
0.57 1.12808185 i
0.58 1.086312605 i
0.59 1.05046936 i
0.6 1.022137757 i
0.61 0.9883659417 i
```

7.2.6.5 Coarse-grained topology topo.xml

Similar to the AA topology file, the CG version contains the information (weight, charge and name) of the atoms (here: the CG beads), and all the bond, angle and dihedral interactions of the beads.

```
<topology>
<molecules>
<clear  />
<molecule name='Be3' nmols='1000' nbeads='3'>
<bead name ='0' type='Bead0' mass='29.062' q='0.0' />
<bead name ='1' type='Bead1' mass='28.054' q='0.0' />
<bead name ='2' type='Bead0' mass='29.062' q='0.0' />

</molecule>
</molecules>
<bonded>
<bond>
<name>bond</name>
<beads>
Be3:0   Be3:1
Be3:2   Be3:1

</beads>
</bond>
<angle>
<name>angle</name>
<beads>
Be3:0   Be3:1   Be3:2
</beads>
</angle>
</bonded>
</topology>
```

7.2.7 Coarse-Graining for Polymers

7.2.7.1 lammps2votca

The tool lammps2votca (https://github.com/Chenghao-Wu/lammps2votca.py) aids in creating required files for VOTCA from LAMMPS. The tool also provides an example of polystyrene. Based on that example it is possible to understand the basic work principle of the software tool. In the python script the user must define a few arrays with the information how the coarse-grained representation of the polymer is described. L2V automatically recognizes molecules and atom types from the given system.data file of the AA geometry for LAMMPS.

However, there are no bonds, angles and dihedrals between different molecules, which leads to errors in the topology file for VOTCA.

With the tool several customized files are created, that contain the information VOTCA needs to conduct the IBI for coarse-graining.

We took lammps2votca as an inspiration and wrote our own L2V code and combined it in the framework that can be found in Appendix D – Software and Data Repositories.

7.2.7.2 cg_system.data

The data file that contains the initial atomic/CG configuration of the system. In this file the same structure as for an AA simulation needs to be followed. The number of atoms, bonds, angles and dihedrals needs to be defined followed by the number of types for each category respectively. The next section defines the system size, afterwards the atom masses are defined. The last section of the file are the atom coordinates followed by the description of their bond, angle and dihedral interactions.

```
CG Kapton

1920 atoms
1904 bonds
1888 angles
1872 dihedrals

4 atom types
3 bond types
4 angle types
3 dihedral types

0 54.790502 xlo xhi
0 54.790502 ylo yhi
0 54.790502 zlo zhi

Masses

1 70.027
2 74.082
3 76.098
4 15.999

Atoms

1 1 1 -9.917 -23.719 0.147
2 1 2 -7.350 -23.084 -0.752
3 1 1 -5.908 -20.756 -0.482
4 1 3 -5.530 -17.730 0.632
5 1 4 -5.340 -15.190 1.620
6 1 3 -7.454 -13.430 1.526
7 1 1 -10.084 -11.652 1.498
8 1 2 -12.646 -11.807 0.807
```

```
Bonds

1 1 1 2
2 1 2 3
3 2 3 4
4 3 4 5
5 3 5 6
6 2 6 7
```

```
Angles

1 1 1 2 3
2 2 2 3 4
3 3 3 4 5
4 4 4 5 6
5 3 5 6 7
6 2 6 7 8
7 1 7 8 9
```

```
Dihedrals

1 1 1 2 3 4
2 2 2 3 4 5
3 3 3 4 5 6
4 3 4 5 6 7
5 2 5 6 7 8
6 1 6 7 8 9
7 1 7 8 9 10
8 2 8 9 10 11
9 3 9 10 11 12
10 3 10 11 12 13
```

7.2.7.3 Coarse-graining file *_cg.xml

Similar to the AA formulation, the mapping_cg.xml file contains the information of the beads. In the AA version the single beads were defined based on which atoms they inherit. In the CG version of the mapping file each bead contains itself as a bead. The file also contains information on which beads interact with one another in what form. The bonded section of the CG version of the mapping file is equivalent to the AA formulation.

```
<cg_molecule>
  <name>HEX</name>
  <ident>Be3</ident>
  <topology>
    <cg_beads>
      <cg_bead>
        <name>A1</name>
        <type>Bead1</type>
        <mapping>Bead1</mapping>
        <beads>1:Be3:0</beads>
      </cg_bead>
      <cg_bead>
        <name>B</name>
        <type>Bead2</type>
        <mapping>Bead2</mapping>
        <beads>1:Be3:1</beads>
      </cg_bead>
      <cg_bead>
        <name>A2</name>
        <type>Bead1</type>
        <mapping>Bead1</mapping>
        <beads>1:Be3:2</beads>
      </cg_bead>
  </cg_beads>
  <cg_bonded>
    <bond>
      <name>bond</name>
      <beads>
        A1 B
        A2 B
      </beads>
    </bond>
    <angle>
      <name>angle</name>
      <beads>
        A1 B A2
      </beads>
    </angle>
  </cg_bonded>
  </topology>
```

7.2.7.4 LAMMPS input script system.in

The system.in file is the main simulation file for LAMMPS. All information regarding the system the used ensembles, the force field parameters and the styling of how the interactions are calculated is defined in the system.in file.

7.2.8 Handling of Tabulated Potentials in LAMMPS – Hexane vs. Kapton

VOTCA prepares the potential tables for the interactions for LAMMPS from the distribution functions from the AA simulations. The same procedure for the combination of LAMMPS and VOTCA to coarse grain a certain system works for hexane. Unfortunately, this was not the case for Kapton. By analysis of the RDFs, and the calculated potentials the following graphs show the differences for one non-bonded interaction.

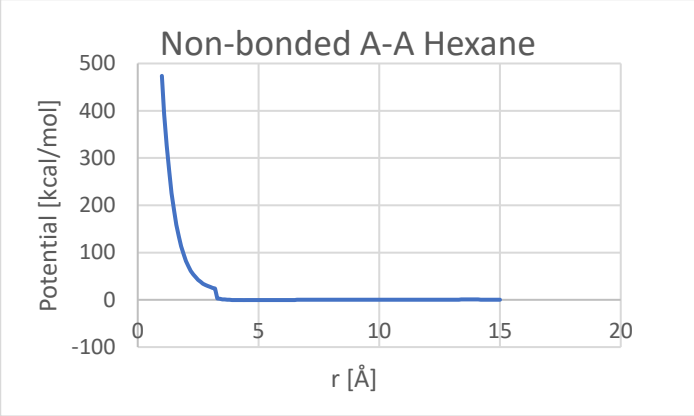

Figure 49: Potential of non-bonded interaction A-A of Hexane.

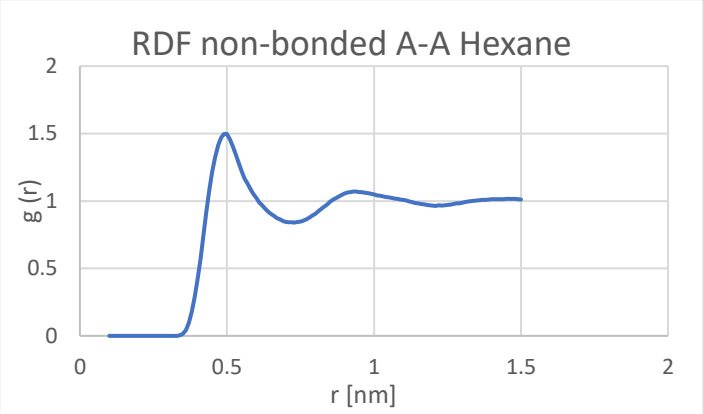

Figure 50: RDF of non-bonded interaction A-A of Hexane.

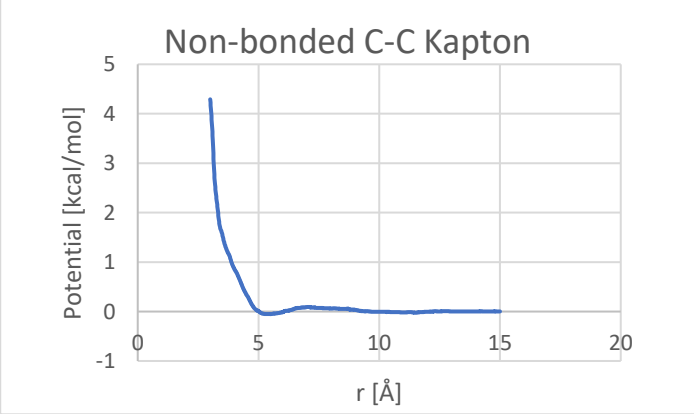

Figure 51: Potential of non-bonded interaction C-C of Kapton.

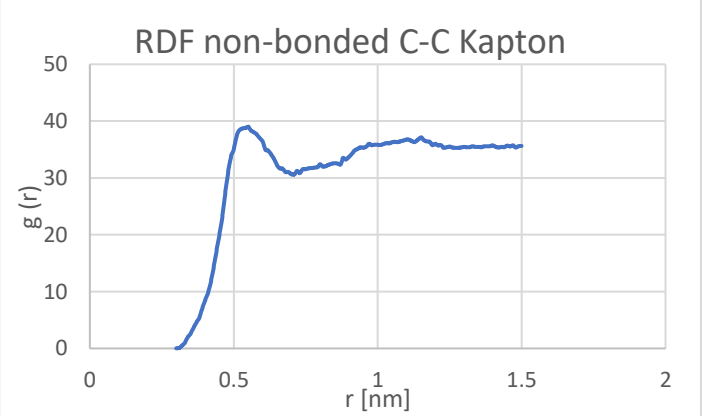

Figure 52: RDF of non-bonded interaction C-C of Kapton.

7.2.8.1 Analysis of Kapton potentials from VOTCA after second iteration step

The potential of the bond C-A as shown in the following figure obviously is wrong, and causes the error.

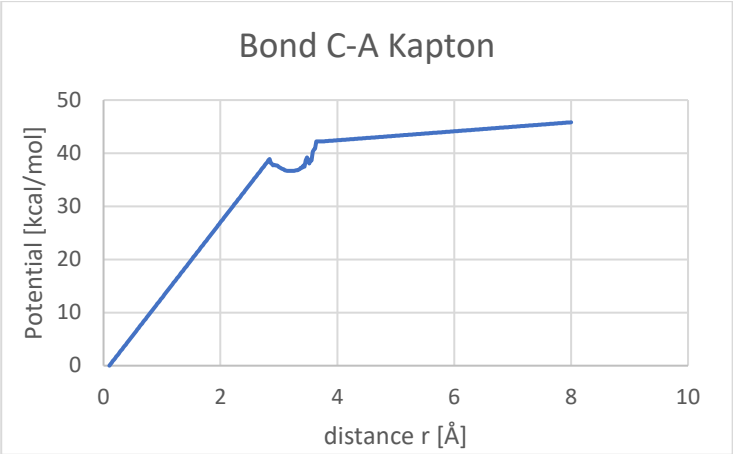

Figure 53: Potential of bonded interaction C-A of Kapton.

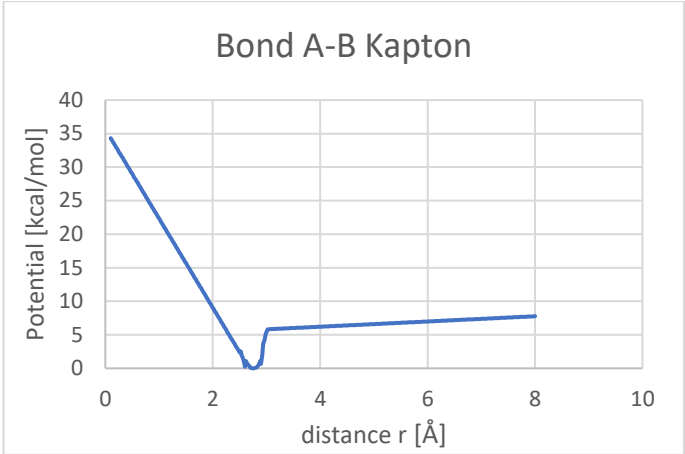

Figure 54: Potential of non-bonded interaction A-B of Kapton.

Furthermore, the distribution of dihedrals is a potential source of error as well.

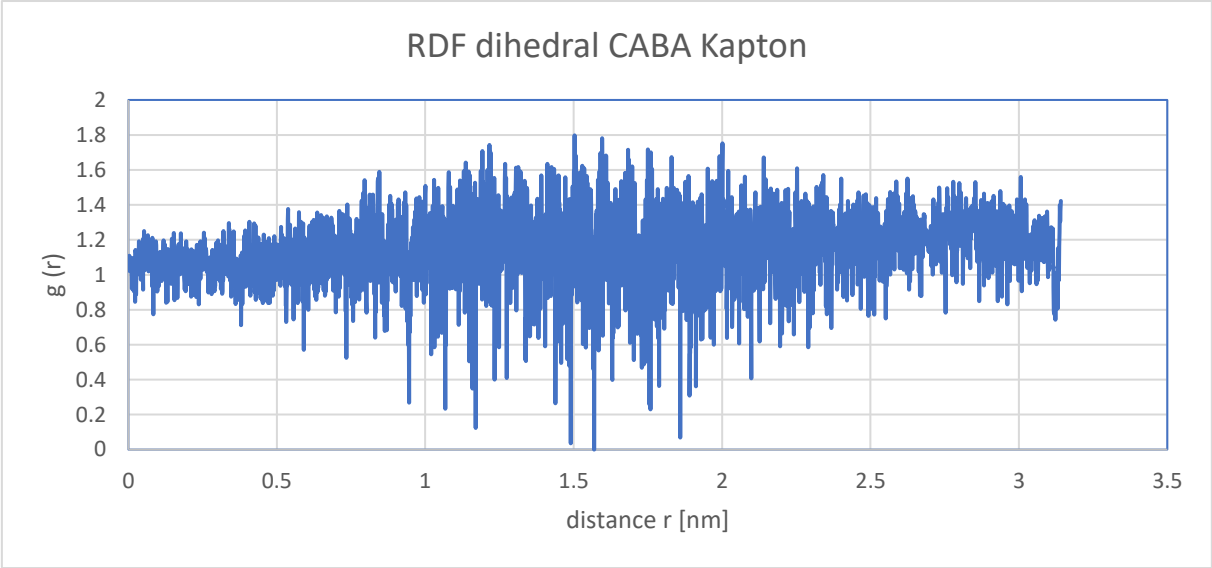

Figure 55: RDF of dihedral interaction CABA of Kapton.

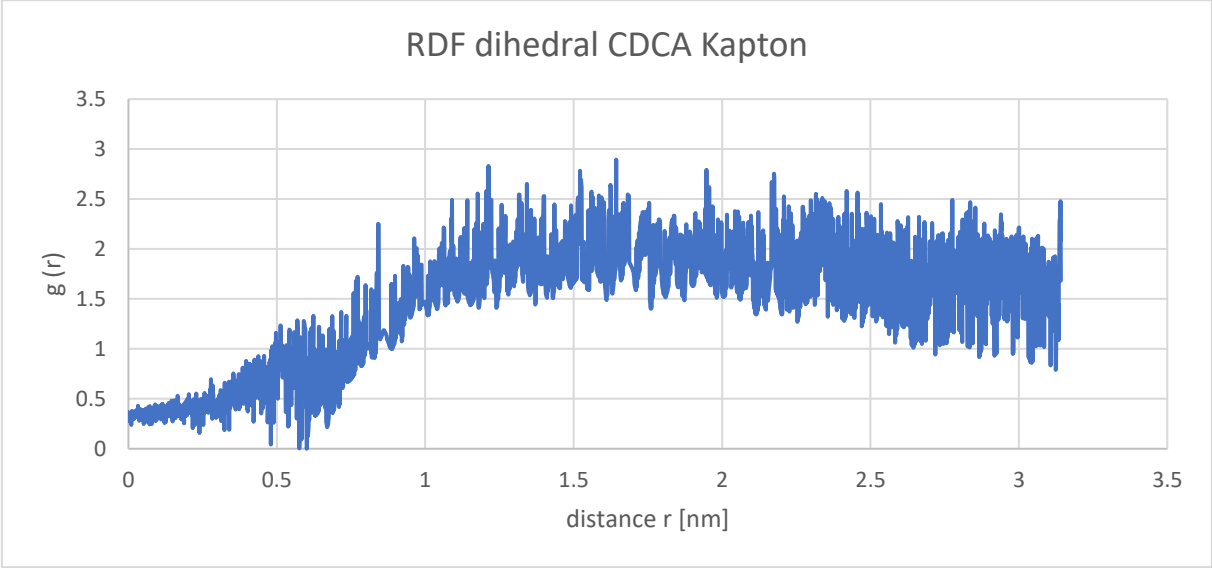

Figure 56: RDF of dihedral interaction CDCA of Kapton.

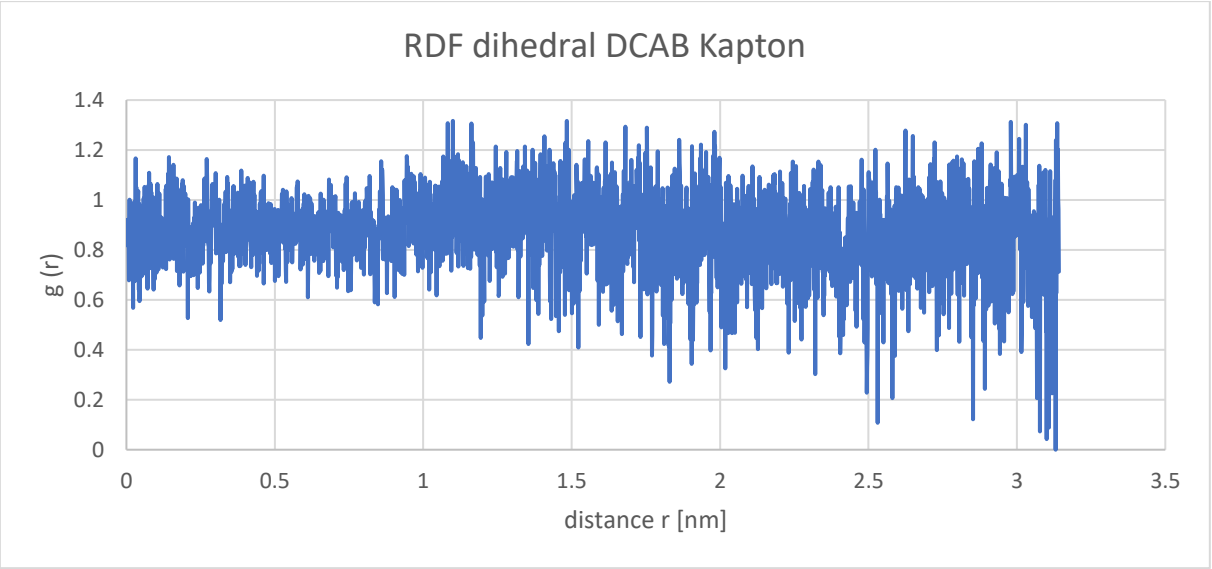

Figure 57: RDF of dihedral interaction DCAB of Kapton.

7.2.8.2 Ideas to overcome the problem with potentials

Ideas to overcome the problems with potentials of bad quality described in the section before would be to:

I. Use coarser tables to overcome the sharp changes in slope of the RDFs
II. Investigate potentials before using them and adapt the unphysical ones (e.g. bond C-A vs. bond A-B) by:
    - Using the same target distribution for C-A as for A-B (see: Figure 53 and Figure 54)
    - Constrain the potential ($F = -\frac{dU}{dr} \rightarrow \int dU = -\int F dr \ \ with\, F = k \cdot (r - r_0)^2$)
III. Work with the function post_update and smoothing from VOTCA
IV. Don't update bonded and non-bonded interactions at once
    - Use [60] to determine the harmonic parameters for the bonded interactions and only fit non-bonded interactions with VOTCA

7.2.8.3 Detected Errors

```
    466000   358.3758       16786.887      26127.05       44963.909     -6495.5027      43702.645
    467000   353.42359      16762.659      26291.897      45076.2        1296.5398      43680.913
    468000   353.54113      16679.175      26222.042      44923.534     -7864.1561      43696.35
    469000   366.3688       16718.819      26122.288      44936.801     -1750.3483      43690.139
    470000   366.69157      16760.505      26112.372      44970.417     -144.60389      43710.507
    471000   362.4806       16741.543      26236.022      45051.017      2757.3385      43674.077
    472000   367.23111      16827.251      26159.46       45087.337      9312.6423      43658.279
ERROR on proc 21: Pair distance < table inner cutoff: ijtype 1 2 dist 0.9998812614635497 (../pair_table.cpp:116)
Last command: run              500000
--------------------------------------------------------------------------
MPI_ABORT was invoked on rank 21 in communicator MPI_COMM_WORLD
with errorcode 1.

NOTE: invoking MPI_ABORT causes Open MPI to kill all MPI processes.
You may or may not see output from other processes, depending on
exactly when Open MPI kills them.
--------------------------------------------------------------------------

Callstack:
/home/user/share/votca/scripts/inverse/inverse.sh - linenumber 246
    do_external - linenumber 177 in /home/user/share/votca/scripts/inverse/functions_common.sh
        /home/user/share/votca/scripts/inverse/run_genericsim.sh - linenumber 60
            critical - linenumber 4 (see 'csg_call --cat function critical')
                die - linenumber 2 (see 'csg_call --cat function die')
environment: line 24: echo: write error: Input/output error
```

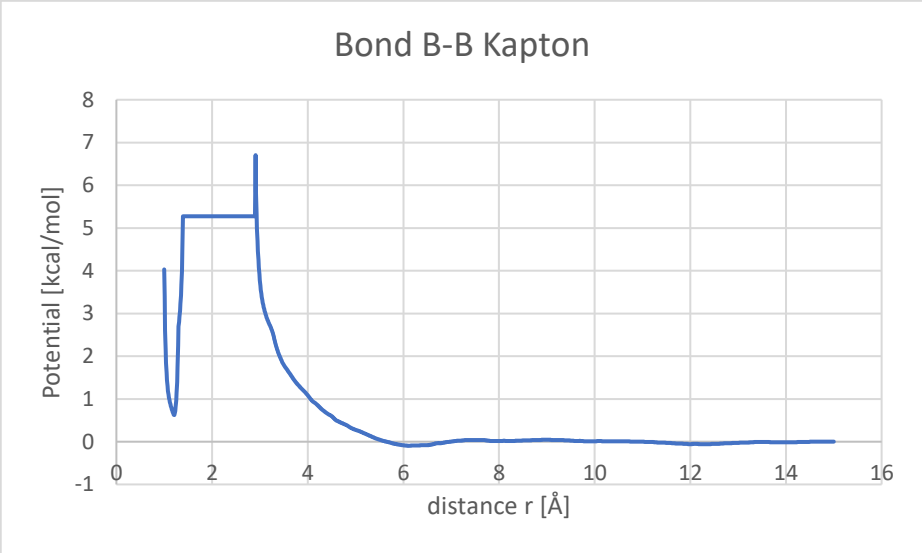

Figure 58: Potential of bonded interaction B-B of Kapton.

Based on this graph it can be seen why the pair distance can get smaller than the tabulated pair distance potential. To solve this, the B-B potential is used and transversed by 1 Å to the left to stabilize the system. No interactions below 2 Å were present and therefore only the physically correct repulsive part of the potential was affecting the bonded interaction B-B.

7.2.9 Adaptation of initial potentials

7.2.9.1 Fitting usable part of initial potentials

Parts of the potentials were identified that represent the expected behavior and a polynomial equation of the second order was fitted to the data. Below the bond of C-A is shown as an example:

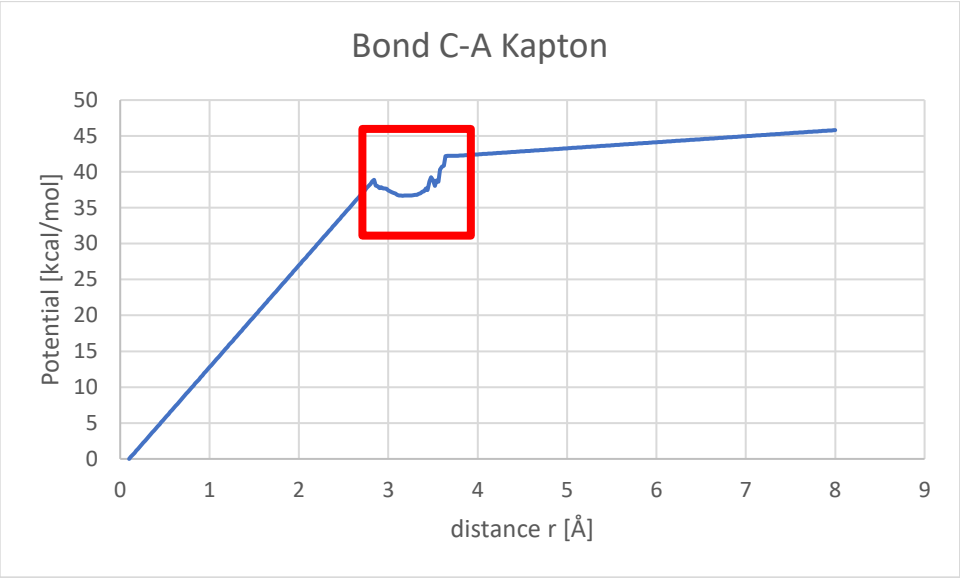

Figure 59: Potential of bonded interaction C-A of Kapton.

The data in the red square was used in this case to fit a polynomial equation of second order to.

7.2.9.2 Possible reason why this potential occurs

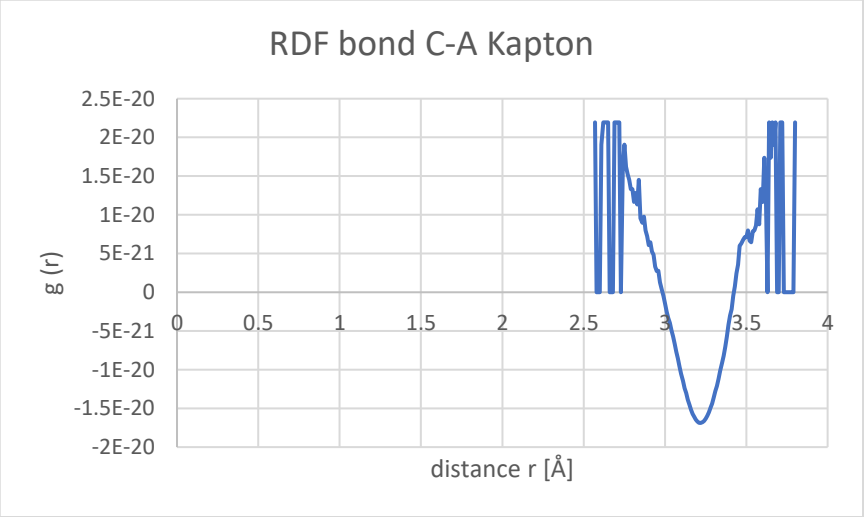

Figure 60: RDF of bonded interaction C-A of Kapton.

Due to the oscillating behavior of the RDF at the boundaries of the usable section, the extrapolation is not really accurate. If VOTCA is using 2 points for the extrapolation that would be connected by a line with negative slope it gets obvious how the potential that is shown in Figure 59 can occur.

7.2.9.3 First results with fitted potentials

The potentials seem to be too small again as the bond length gets longer than the maximum estimated by the table:

```
  current step  : 0
  Time step     : 0.1
WARNING: Inconsistent image flags (../domain.cpp:819)
Per MPI rank memory allocation (min/avg/max) = 8.028 | 8.029 | 8.032 Mbytes
   Step          Temp          E_pair         E_mol          TotEng         Press          Volume
         0   0             -287.85927      28685.437      28397.578      2946.5461      164481.04
ERROR on proc 4: Bond length > table outer cutoff: type 1 length 4.7921971 (../bond_table.cpp:597)
Last command: run              200000
--------------------------------------------------------------------------
```

7.2.10 Boltzmann Inversion for initial potentials

The Boltzmann inversion is used to get the potential of an interaction based solely on the geometric property of the distribution functions for each interaction (i.e., bonds, angles, dihedrals, and non-bonded). The interested reader is referred to the work of Rühle et al. [21], in which equations 5 and 6 describe the mathematical principle of the function "csg_stat" from VOTCA.

7.2.11 Final approach for coarse-graining of the polymer Kapton®

After a thorough investigation of literature, it was found that seldomly both bonded and non-bonded interactions are parametrized simultaneously [62] [91] [77][61]. Therefore, it was decided that the bonded interactions won't be parametrized by the IBI procedure.

It was further investigated if the iterative procedure improves the potential of the nonbonded interactions. Figure 61 below highlights that for the nonbonded interaction of the A-A beads, even 100 iteration steps are not improving the potential. This can similarly be found for all other non-bonded interactions as well.

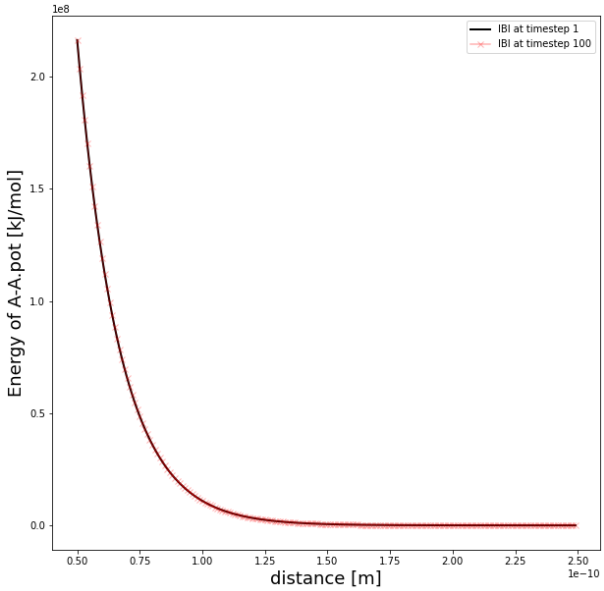

Figure 61: Comparison of potentials at 1 and 100 iteration steps.

Therefore, it was decided that the potential for the non-bonded interactions will be taken from the first Boltzmann Inversion (BI) step. Additionally, the dihedral potential was also taken from

the Boltzmann Inversion as, (i) no dihedral potentials from literature were possible to use, (ii) often in CG simulations the dihedral potentials are even left unconsidered [60].

For the bonded interaction the potentials were not built from BI but taken from similar coarse-grained beads from Wen et al. [60]. The figure below shows the section of the input file that includes the force field and potential parameters.

```
units       real
atom_style  molecular

pair_style  table linear 100
pair_modify tabinner 2.0
pair_modify mix geometric

bond_style harmonic


angle_style harmonic

dihedral_style table linear 100

 read_data       cg_system.data
# read_restart KaptonCG.%.*

pair_coeff  1 1 C-C.pot VOTCA 15
pair_coeff  2 2 D-D.pot VOTCA 15
pair_coeff  3 3 A-A.pot VOTCA 15
pair_coeff  4 4 B-B.pot VOTCA 15

pair_coeff  3 4 A-B.pot VOTCA 15
pair_coeff  1 3 A-C.pot VOTCA 15
pair_coeff  2 3 A-D.pot VOTCA 15
pair_coeff  1 4 B-C.pot VOTCA 15
pair_coeff  2 4 B-D.pot VOTCA 15
pair_coeff  1 2 C-D.pot VOTCA 13

bond_coeff 1 300 2.77
bond_coeff 2 400 3.22
bond_coeff 3 500 2.76


angle_coeff 1 310 99
angle_coeff 2 310 147
angle_coeff 3 310 176
angle_coeff 4 310 114

dihedral_coeff 1 dihedralCDCA.pot VOTCA
dihedral_coeff 2 dihedralDCAB.pot VOTCA
dihedral_coeff 3 dihedralCABA.pot VOTCA
```

With these settings it was possible to replicate the results regarding the density of the 21-step equilibration of a Kapton® system. A system of 64 chains and a chain length of 40 monomers (99840 atoms in total) was coarse-grained to a system of 15360 CG beads, that was equilibrated and simulated for 10 ns in around 16 h on 24 processors (shown in picture below)

```
  11265542   298.74683     -511.24904      1.3240371      49.583075
Loop time of 56527.5 on 24 procs for 10000000 steps with 15360 atoms

Performance: 0.153 ns/day, 157.021 hours/ns, 176.905 timesteps/s
72.0% CPU use with 24 MPI tasks x no OpenMP threads

MPI task timing breakdown:
Section |  min time  |  avg time  |  max time  |%varavg| %total
---------------------------------------------------------------
Pair    | 9971.6     | 26526      | 43656      |5238.8 | 46.93
Bond    | 1552       | 3191.4     | 4332.3     |1131.6 |  5.65
Neigh   | 10.541     | 10.689     | 10.784     |   2.4 |  0.02
Comm    | 5592.2     | 23806      | 41789      |5887.8 | 42.11
Output  | 75.778     | 76.466     | 89.891     |  32.0 |  0.14
Modify  | 2058.2     | 2171.3     | 2303.4     | 171.3 |  3.84
Other   |            | 745.8      |            |       |  1.32

Nlocal:            640 ave         900 max         300 min
Histogram: 1 0 3 0 6 3 6 2 1 2
Nghost:         4032.46 ave        5479 max        3245 min
Histogram: 4 6 3 2 3 1 2 0 1 2
Neighs:         98033.2 ave      166211 max       35624 min
Histogram: 3 0 3 6 0 4 3 2 1 2

Total # of neighbors = 2352796
Ave neighs/atom = 153.17682
Ave special neighs/atom = 5.95
Neighbor list builds = 1348
Dangerous builds = 0
    unfix fxnpt


#  ---- (end of examples) ----

Total wall time: 16:06:55
```

Columns from left to right: step (represents 1 fs per step), temperature, pressure, density, radius of gyration of the polymer system.

Although the density of the system at 1324 kg/m³ is smaller than the literature value of 1420 kg/m³, the value from the CG simulation represents the found density in AA simulations accurately.

7.2.12 Possible improvements in the connection between LAMMPS and VOTCA

7.2.12.1 Automatic plotting of potential graphs from VOTCA IBI

During our investigation an important part was the monitoring of the potentials that were calculated from the IBI in VOTCA. To check the quality of the determined potentials they had to be investigated with an in-house code. An implementation of this monitoring tool in VOTCA, that provides graphs of the potentials over the distance or the angle, depending on the interaction, would be a very helpful and time saving feature.

7.2.12.2 Deactivate interpolation of tabulated potentials in LAMMPS

This would be a very important feature for future versions (here Version 2020 of LAMMPS was used). The LAMMPS documentation [20] explains the correct application of the "pair_style table" that is used for tabulated non-bonded potentials in this work. The general form of the pair_style is a follows:

"pair_style table style N"

The style basically describes how the table from the file should be interpolated for the application in LAMMPS. The important part here is the parameter N, that describes how many entries the table that LAMMPS uses to calculate the interaction forces should have. In the LAMMPS documentation it is suggested to define N in the pair_style command equivalently to the entries in the tabulated potential file.

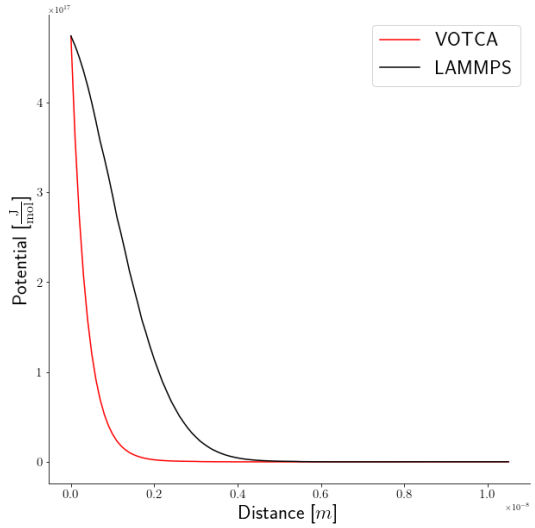

Figure 62: Comparison of isopropanol CG potential from VOTCA (red) and the interpolated potential from LAMMPS (black).

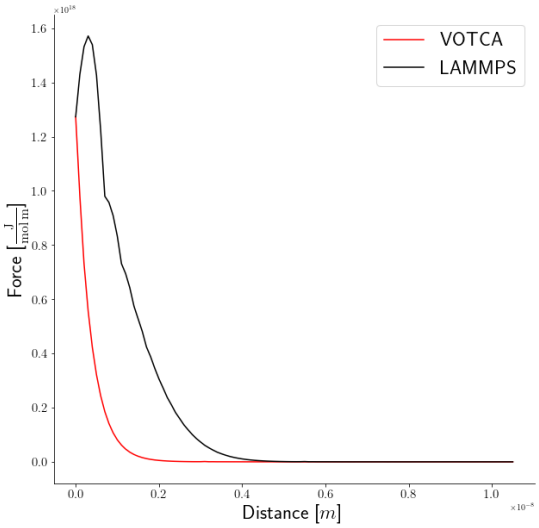

Figure 63: Comparison of isopropanol CG forces from VOTCA (red) and the interpolated potential from LAMMPS (black).

The results of using a linear pair_style table where N equals the number of entries in the tabulated potential file from VOTCA are shown in Figure 62 and Figure 63. As can be seen, the interpolated potential and force respectively (indicated by the black lines in Figure 62 and Figure 63) are different from the found potential and force from the IBI method. Due to the determination of the force based on the potential (first derivative), an unphysical behavior occurs that explains the instability of the simulation.

LAMMPS does not allow the user to decativate this interpolation and directly use the tabulated potential from the input file. Even by hard coding the flags that should allow this behavior in the LAMMPS source code did not resolve the problem of the difference in potential and force.

7.3 Appendix C – Maxwell-Stefan diffusion from MD simulations

Based on the Einstein equation described in the methods section of the second part of the thesis, it is possible to calculate the self-diffusion coefficient from the MSDs of diffusing species. However, determining the self-diffusion coefficient in experiments, where one species is diffusing in another one (here: isopropanol or ions in Kapton), is difficult.

In this work we followed the method described by Kubaczka [70] based on Bearman's equations [71] and friction coefficients described by Vrentas and Vrentas [72], [73], [74]. The interested reader is advised to follow the complete description of the method in the literature sources above. However, the basic idea that can be followed to calculate the Maxwell-Stefan diffusion coefficient of a solvent in a polymer, based on the respective self-diffusion coefficients, is described here.

7.3.1 Calculation of the Maxwell-Stefan diffusion coefficient from self-diffusion

Kubaczka [70] combines statistical mechanical theory, thermodynamics of irreversible processes and continuum mechanical theory to obtain the definition of the Maxwell-Stefan diffusion coefficient shown in Eqn. (C-1).

$$D_{ij} = \frac{RT}{C\psi_{ij}} \tag{C-1}$$

In Eqn. (C-1), R is the gas constant, T is the temperature of the system, C is the total concentration of the system and ψ_{ij} is the friction coefficient between the components i and j.

Eqn. (C-2) describes the dependences between self-diffusion and the friction coefficients based on Bearman's equations [71] for a binary system.

$$D_1 = \frac{RT}{c_1\psi_{11} + c_2\psi_{12}} \; and \; D_2 = \frac{RT}{c_1\psi_{21} + c_2\psi_{22}} \tag{C-2}$$

Vrentas and Vrentas [72], [73], [74] argue that the adoption of the geometric relationship between the friction coefficients is generally viable and experimentally confirmed.

$$\psi_{12} = (\psi_{11}\psi_{22})^{0.5} \tag{C-3}$$

With the geometric relationship shown in Eqn. (C-3) in combination with Eqn. (C-2), a clear relationship between self-diffusion and the friction coefficients can be provided:

$$\frac{D_1}{D_2} = \left(\frac{\psi_{22}}{\psi_{11}}\right)^{0.5} \tag{C-4}$$

$$\psi_{11} = \frac{RT}{D_1 \cdot \left(c_1 + c_2 \cdot \left(\frac{D_1}{D_2}\right)\right)} \; and \; \psi_{22} = \frac{RT}{D_2 \cdot \left(c_1 \cdot \left(\frac{D_2}{D_1}\right) + c_2\right)} \tag{C-5}$$

Eqn. (C-5) and Eqn. (C-3) allow to calculate the Maxwell-Stefan diffusion coefficient with Eqn. (C-1) as the total concentration and the temperature can be obtained from the MD simulations as well as the self-diffusion coefficients D_1 and D_2.

This is the basic concept for a binary system as it was investigated in this work. However, in the literature sources, the authors also describe the application of this method to a multicomponent system.

7.4 Appendix D – Software and Data Repositories

7.4.1 LAMMPS

The version used in the present work can be found with the following information:

LAMMPS branch: stable; commit: 584943fc928351bc29f41a132aee3586e0a2286a (28.10.2020)

A complete installation guide for LAMMPS can be found at: https://docs.lammps.org/Install.html

7.4.2 VOTCA

The version used in the present work can be found with the following information:

VOTCA branch: master, commit: 305586376 (23.11.2023)

A complete installation guide for VOTCA can be found at: https://www.votca.org/INSTALL.html

7.4.3 Moltemplate

The version used in the present work can be found with the following information:

moltemplate branch: master; commit: 9f1512e6b25f8325b5c6c1a4f2fecdc94eda40f1 (21.3.2021)

A complete installation guide for moltemplate can be found at: https://github.com/jewettaij/moltemplate

7.4.4 Data and Software repository

The used software for postprocessing can be found under the following link and can be opened after contacting for viable reasons:

https://gitlab.tugraz.at/90ED8AF830FCF564/lammps2votca

The data including all simulations is saved on the NAS01 server of the Institute of Process and Particle Engineering at Graz University. Access to this data is provided upon reasonable request.